UNIVERSITY OF SOUTHAMPTON

HIGH FIDELITY IMAGING IN ELECTRICAL IMPEDANCE TOMOGRAPHY

Marc Molinari

A thesis submitted for the degree of
Doctor of Philosophy

Department of Electronics and Computer Science,
Faculty of Engineering and Applied Science

June 2003

UNIVERSITY OF SOUTHAMPTON

ABSTRACT

FACULTY OF ENGINEERING AND APPLIED SCIENCE

ELECTRONICS AND COMPUTER SCIENCE DEPARTMENT

Doctor of Philosophy

HIGH FIDELITY IMAGING IN ELECTRICAL IMPEDANCE TOMOGRAPHY

By Marc Molinari

This thesis addresses the computational reconstruction of images using Electrical Impedance Tomography (EIT). EIT is an imaging method, in which electrical currents are injected through electrodes into a conducting volume and the resulting potential distribution is measured at surface electrodes. From these potentials, an image of the electrical conductivity can be obtained using numerical reconstruction techniques. This non-linear reconstruction is mathematically difficult and computationally intensive. Most applications in medicine and industry rely upon a fast and accurate image acquisition. The aim of this investigation is to find methods which improve the speed and accuracy of EIT by a range of improvements to the numerical methods used in the forward solution and inverse reconstruction.

We investigate the impact of the finite element discretization on the performance of computing the electric field forward solution. We derive an a posteriori error estimate on the finite element mesh and implement 2D adaptive mesh refinement techniques in an optimised forward solver. Our results of this novel approach show that a speed-up of approximately an order of magnitude can be obtained.

We extend the developed iterative Newton-Raphson algorithm to include image smoothness constraints and adaptive mesh refinement based on conductivity gradients in the image. The results show that the image resolution can be made independent of the underlying numerical discretization and therefore is limited only by the level of noise present in the measurements. An additional benefit of this new technique is the automatic focus of available computational resources on key regions for forward solution and inverse reconstruction.

As 3D impedance imaging becomes computationally too expensive for the Newton-Raphson method, we develop a novel non-linear conjugate gradient algorithm incorporating 3D adaptive mesh refinement routines, and present results showing the decrease of memory requirements and the increase in image reconstruction performance. In addition, a Matlab software package containing optimised routines for the finite element-based computations in EIT has been developed as part of this work.

Finally, we outline a method for obtaining a map for the determination of the reconstruction reliability and image correlation of an EIT algorithm.

With the improvements to reconstruction accuracy and speed investigated in this thesis, we conclude that efficient non-linear 3D impedance imaging is feasible.

Author's declaration

The work of this report is partly the result of collaboration with others. The author acknowledges the following efforts as contributions to his work:

Prof. Simon J Cox introduced the author to the idea of using adaptive finite element meshes in the forward solution and reconstruction process of impedance images.

Hans Fangohr created and contributed figure 3.1 showing results from the developed Vortex Meshing method as described in 3.1.1.

Dan Elphick has developed the Matlab code browser which produced figure 3.15 showing the call-graph of the developed SEEIT software package.

The author acknowledges the contribution of co-authors to published papers, in particular Dr. Barry H Blott, Prof. Simon J Cox and Dr. Geoffrey J Daniell.

Acknowledgements

I would like to thank my supervisor Prof. S.J. Cox for his support, guidance, criticism and help. I would also like to thank a number of other people, in particular Dr. B.H. Blott and Dr. G.J. Daniell from the Department of Physics and Astronomy for valuable discussions, the provision of data and feedback on this work as well as Dr. H. Fangohr and Dr. J.M. Generowicz for our stimulating discussions on finite element mesh creation. Thanks are also due to my fellow students and colleagues D. Beckett, B. Hiett, and Dr. K.S. Thomas for their input towards this work.

Thanks also to all those researchers working on EIT who I was able to meet and engage with in discussions at the numerous conferences in many parts of the world.

My deepest appreciation goes to my parents H.&M. Molinari and my fiancée Lin as well as my sister, all of whom have supported me during the course of this project and beyond. Many thanks for not complaining how little you have seen of me over the past years and to Lin for being patient when it got late in the evenings due to thesis work.

The Department of Electronics and Computer Science at the University of Southampton deserves my gratitude for providing financial support in form of a maintenance grant and I acknowledge the contribution of a studentship from EPSRC.

—

Ich möchte meinem Supervisor, Prof. S.J. Cox, herzlich für seine Unterstützung, Unterweisung, Kritik und Hilfe danken. Mein dank geht auch an Dr. B.H. Blott und Dr. G.J. Daniell vom Department for Physics and Astronomy für wertvolle Diskussionen, das Zurverfügungstellen von Daten und ihr Feedback zu dieser Dissertation. Ebenso möchte ich Dr H. Fangohr und Dr J.M. Generowicz fuer unsere anregenden Diskussionen über Finite Elemente Mesh Konstruktion danken. Danke auch an meine Mitstudenten D. Beckett und B. Hiett sowie Kollegen Dr. K.S. Thomas für ihre Beiträge.

Danke an all die in EIT forschen und welche ich auf zahlreichen Konferenzen in aller Welt bei Diskussionen kennenlernen konnte.

Das grösste Dankeschön geht an meine Eltern H.&M. Molinari, und meine Partnerin Lin, die meine Ausbildung kontinuierlich unterstützt und gefördert haben und die sich ebenso wie meine Schwester nicht darüber beschwerten, wie selten sie mich in den letzten Jahren gesehen haben. Vielen Dank auch an meine Partnerin Lin, die mich während des Verfassens meiner Arbeit unterstützt und oft mit Geduld die späten Abende ertragen hat.

Finanziell unterstützt wurde diese Arbeit durch ein Stipendium des Department of Electronics and Computer Science der University of Southampton und durch Studienbeiträge des EPSRC.

Contents

List of Tables

List of Figures

Chapter 1

Introduction

1.1 Electrical Impedance Tomography

The non-invasive and non-destructive imaging of the interior of objects has long been a challenge. Electrical Impedance Tomography (EIT) is one possible answer to the question of how to obtain information from otherwise inaccessible regions within a closed and often opaque volume. EIT is a technique which can produce images of the electric admittivity or conductivity distribution of electrically conducting objects by injecting known amounts of current and measuring the resulting electric field at the surface of the object. This technology has a wide variety of applications in many different fields which we will discuss briefly in the following sections before concentrating our review on reconstruction algorithms for absolute imaging purposes.

1.2 Applications

1.2.1 EIT in Process Tomography

Applications of EIT exist in the monitoring of conducting liquids or in the evaluation of chemical compounds in pipes and stirring vessels. The petrochemical industry as well as other branches concerned with material processes are interested in imaging characteristics such as liquid quantity, mixing behaviour and rate of flow using electrical resistance tomography applications (Dickin and Wang, 1996). The accurate knowledge of fixed electrode positions and the often simple geometry of the container as well as the possibility of applying relatively large currents through

the compound make electrical tomography a well-suited candidate for industrial applications. Much research is currently carried out in this field, supported by many manufacturing companies, and the popularity of EIT in the commercial sector is rising continuously (WCIPT, 2001).

1.2.2 EIT in Geophysical Research

Electrical properties of soil, rocks, liquids and ancient building material contain a variety of information about the processes within the earth and geophysical and archaeological structures below the earth's surface. Geophysical research using electrical resistance tomography has been known for a long time and examples of its use include the detection of buried buildings and walls, the monitoring of ground water, the detection of mines and caves as well as the discovery of hidden water or oil reservoirs. In archaeology, this type of measurement allows to build up a picture of a site before disturbing it, so that targeted excavation can be carried out to avoid damaging valuable ancient and preserved sites.

Typical characteristics of geophysical prospecting experiments are the large current (up to 15 Amp) and the electrode spacing (1000m), as for example given in Schütze (1998). If higher resolution is sought, as required in the case of archaeological research, then electrode arrays with a grid spacing of typically 0.5m are used (Szymanski and Tsourlos, 1993). Although a particular difficulty of this technique is the behaviour of the ground as a non-linear capacitor exhibiting subsurface polarization (Coskun and Szymanski, 1993), satisfying results of reconstructions can be achieved. Often, the permittivity (or polarization) is measured using the transient response of the investigated volume.

1.2.3 EIT for Non-Destructive Material Testing

Although EIT has large potential in the material and food sciences sector for the classification, testing and quality assessment of industrially manufactured products, few compelling examples are in widespread use. EIT has been used in quality assurance of agricultural products such as muskmelons (Toyoda, 2000).

1.2.4 EIT for Medical Imaging

A major application area for EIT is the medical sciences (Committee on the Mathematics and Physics of Emerging Dynamic, 1996). These have experienced the proliferation of a broad range of different imaging methods in recent years including X-Ray Imaging, Computer Tomography (CT), Ultrasound Imaging, Magnetic Resonance Tomography (MRT), Positron Emission Tomography (PET), Single Photon Emission Computed Tomography (SPECT) and many others. The resolution of some of these is incredibly high: spiral computed tomography, for example, can achieve spatial resolutions down to 1 mm (Dawn *et al.*, 2001; Siemens, 1999). However, this comes at a very large cost for the apparatus and requires expensive hospital space as well as pre-booking mechanisms for scheduled use. Most of these methods are hence not suitable for (long-term) monitoring of patient parameters.

Table 1.1 gives an overview of some of the most common imaging methods used for medical purposes and their characteristics as given by Webb (1988) and by Budinger (2001).

An ideal imaging method for the medical field would be non-invasive, portable (small and light), harmless to the patient, inexpensive and easy-to-use at the same time as providing medically relevant information. A device with these properties would equally allow for real-time imaging as well as for long-term monitoring, in particular since it could be held at hospitals in large numbers (Gaeke, 1992). An Electrical Impedance Tomograph fulfils these requirements and has large potential in medical imaging since it provides images of parameters which cannot be obtained by most of the other methods. In addition it can be made safe to comply to British and European Standards by restricting current densities and frequencies (Lionheart *et al.*, 2001).

Figure 1.1 shows the distinct wide range of electrical conductivities in biological tissues, ranging from 0.0067 S/m for bone to 1.6 S/m for cerebrospinal fluid.

For comparison, the absorption coefficients for X-ray imaging are plotted in the same graph. The figure indicates that EIT images of biological material should be superior to X-ray images in terms of tissue contrast. However, the low resolution of EIT imaging prevents the images from showing the same detail as X-Ray

Technology	Spatial resolution	Time resolution	Cost	Imaging modality	Physical mechanism
EIT	low	msec-sec	low	mainly physiological	electrical conductivity
Infra-Red	low	real-time	low	mainly anatomical	temperature
Ultra-Sound	low	real-time	low	anatomical + physiological	acoustic impedance / Doppler shift
MRI	v.high	sec	high	mainly anatomical	density of protons (spin relaxation)
X-Ray	high	–	medium	anatomical	absorption & scattering
X-Ray CT	v.high	–	high	anatomical	absorption
SPECT	medium	sec-min	high	anatomical + physiological	single photon emission
PET	high	sec-min	v.high	anatomical + physiological	gamma ray emission

Table 1.1: Comparison of medical imaging methods.

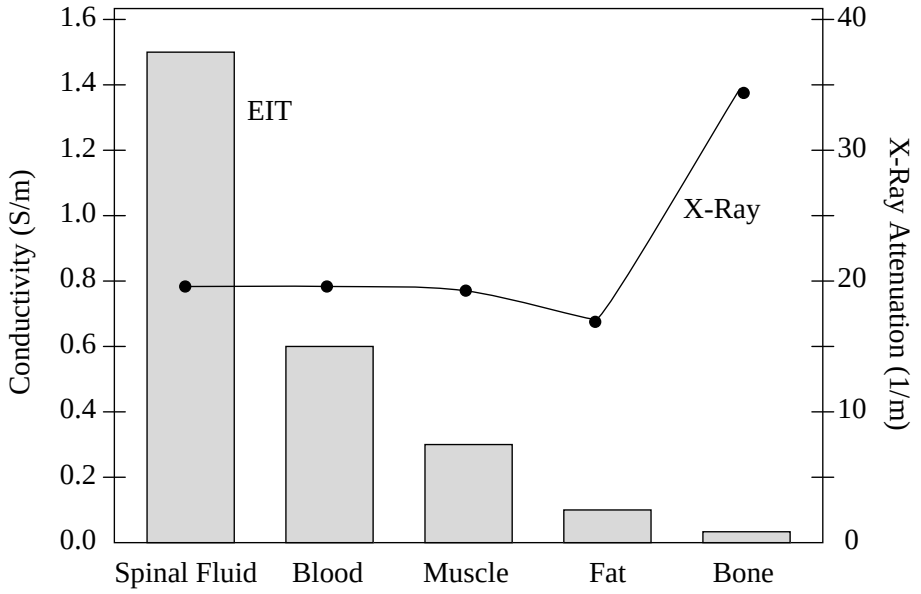

Figure 1.1: Comparison of EIT and X-Ray contrasts in biological tissues (values from Meeson 1997).

images. Although EIT resolution is low at present, the advantages over higher resolution imaging techniques make it worthwhile to further investigate EIT techniques (Meeson, 1997).

A summary of the major medical applications of EIT is given, for example, by Brown (1990) and in Cheney *et al.* (1999); a further overview by Bhar can be found in Webster (1990). These applications include cardio-pulmonary monitoring (Brown *et al.*, 1985), the imaging and monitoring of gastric emptying (Avill *et al.*, 1989), measurement of lung resistivity (Woo *et al.*, 1992) and lung water, assessment of acute pulmonary edema (Newell *et al.*, 1993), detection of intra-ventricular haemorrhage, pulmonary function studies and lung ventilation (Adler *et al.*, 1996), cancer detection, and brain activity localization, to mention but a few.

Dynamic vs. Static Imaging

Electrical Impedance Tomography can be used for differing clinical applications, depending on the *imaging modality* used. The two main forms of impedance tomography are *dynamic imaging* and *static imaging* yielding *differential* and *absolute* images respectively. The images produced by differential imaging represent the conductivity changes of a region between two time intervals, as initially introduced by Barber and Brown (1984). This allows for monitoring changes such as gastric

emptying or long-term observation of body functions/volume changes. Imaging physiological function within the body largely relies on this technique which is relatively simple to implement. A more recent meaning of "dynamic imaging" has been introduced by the work of the Kuopio group, which is looking at imaging and tracking objects in the fluid flow within a pipe.

In this thesis, however, we are mainly concerned with the quantitative reconstruction of static conductivity images which requires more advanced numerical algorithms.

The reasons that EIT is not yet a well-established tool in the biomedical sector are mainly its sensitivity to electrode positioning, its rather low image resolution due to noise in the measurements and numerical effects of the discretization, the often time-consuming non-linear numerical reconstruction and a lack of dedicated easy-to-use software.

1.3 A brief history of EIT

In this section, we summarise some of the key developments in the history of impedance imaging which form the basis and framework for current and future research.

Reconstruction

1978 The first attempt at producing images of a body in terms of its electrical properties was done by Henderson and Webster (1978). They used a single large electrode to drive current through the body to a 12 by 12 square electrode array on the other side.

1980 Calderon (1980) formulated the mathematical background of electrical prospection as a boundary value problem and showed that the derivative is injective.

1984 The initial work of Barber and Brown (1984) on Applied Potential Tomography (APT) was one of the first to address the problem of reconstructing conductivity images for medical application. A backprojection algorithm was used for reconstruction which is similar to those used for X-Ray CT imaging.

1985 Murai and Kagawa (1985) based their EIT reconstruction on a finite element discretization of a 2D domain. The similarity between the FE formulation

and electrical circuits was used to reconstruct conductivity images according to the sensitivity or lead theorem as derived by Geselowitz (1971) and Lehr (1972).

1985-1987 Two significant papers of Kohn and Vogelius (1985) and Sylvester and Uhlman (1987) contain mathematical proofs that both piecewise analytic and smooth conductivities can be distinguished theoretically by boundary measurements made with infinite precision.

1987 In one of the most frequently cited articles in EIT, Yorkey *et al.* (1987) compared the performance of six different reconstruction algorithms. He detailed two methods for obtaining the Jacobian for the modified Newton-Raphson method which proved to be the most robust and efficient technique for conductivity reconstructions. It was found later that the two methods were the same.

1987 The SVD method was used by Breckon and Pidcock (1987a) to analyze instability in the EIT problem. EIT has been described as a highly ill-posed, nonlinear inverse problem (Breckon and Pidcock, 1987b) and techniques for producing absolute images are all extremely sensitive to any errors which occur in the system.

1987 Seagar *et al.* (1987) investigated the theoretical limits of sensitivity and resolution in EIT. They derived a method to predict the smallest object size detectable by measurements with a known level of noise. They addressed the aspects of geometric flexibility, dimensionality, approximations, speed and computational effort required for an efficient EIT reconstruction algorithm.

1989 Clarke and Janday (1989) explained the method of maximum statistical entropy and demonstrate how it can be applied to biomagnetic inverse problems by finding the solution for a simplified spherical inverse problem. This work is based on previous work by Skilling and Bryan (1984) and by Clarke (1989) on the use of probabilistic methods in inverse problems.

1990 Gisser *et al.* (1990) studied the problem of choosing current patterns, electrode size and number in terms of the spectral properties of certain pseudo-differential operators. He found that the resolution goes to zero as the number of electrodes goes to infinity for pair drives.

1991 Somersalo *et al.* (1991) presented the Layer stripping algorithm for impedance imaging. This algorithm is critically dependent upon the noise level, even

when as low as 0.05% and its reconstruction cost is dominated by the cost of back-propagating the matrix elements; corresponding to a CPU cost growth of $\mathcal{O}(n_M)$ with n_M being the number of measurements.

1992 Dobson (1992) addressed convergence properties of reconstruction algorithms.

1993 Woo *et al.* (1993) found that Hachtel's augmented Matrix method for solving the normal equations is faster than Yorkey *et al*'s (1987) technique as the Hessian matrix does not need explicit computation and the augmented matrix is sparse.

1994 The work by Artola and Dell (1994) tried to obtain quicker covergence through modifying the Newton method by approximating the Jacobian with a singular value decomposition. Although their quasi-Newton algorithm achieved superlinear convergence, the results were obtained with perfect noise-free measurement data only.

1994 A reconstruction algorithm based on optimal experiments, called POMPUS, has been developed and presented by Paulson *et al.* (1994). It is a fast and efficient reconstruction algorithm which converges along the direction of steepest descent and reduces the computational cost of solving the linearized form of the inverse problem from $\mathcal{O}(n^6)$ to an optimal $\mathcal{O}(n^3)$ (Paulson *et al.*, 1995).

1994 Incorporation of prior information of the conductivity distribution into the EIT problem formulation has been attempted by Dobson and Santosa (1994a). They included the assumption that the unknown conductivity is "blocky", i.e. a piecewise constant function with small variation in the discontinuities. With this approach, reconstructions of fine details and highly oscillatory features were difficult or impossible to obtain.

1994 Otto and Chew (1994) derived a time-harmonic formulation for the solution of the EIT inverse problem. Their T-matrix method is very fast, finite element free and addresses the problem of low resolution of the electrostatic description by applying an electrodynamic physical model. Results show that only few iterations are required to obtain good results from 2D data with no additional cost compared to an FE solution.

1995 Bayford *et al.* (1995) presented experimental results from a reconstruction algorithm based on backprojection of Lagrange multipliers. The data was collected in a cylindrical saline-filled tank and the results show that it is possible to produce images in conditions similar to those producing epileptic activity. Although the algorithm does not show much improvement compared to the Barber and Seagar backprojection algorithm, the ringing artefact in the image was reduced.

1995 3D reconstruction has been attempted in Morruci *et al.* (1995) using a direct sensitivity matrix approach.

1996 Vadasz and Sebestyen (1996) compared the modified Newton-Raphson algorithm of Yorkey *et al.* (1987) with the Spectral Expansion Reconstruction method of Zadehkoochak *et al.* (1991). They found that the spectral expansion analysis is identical to one step of the Newton-Raphson algorithm and that thus the two methods can be combined to develop more sophisticated reconstruction procedures (Zadehkoochak, 1992).

1996 A constructive proof of uniqueness for the 2D boundary value problem was derived by Nachman (1996). Siltanen and Mueller implemented his technique later.

1996 An article in Nature by Metherall *et al.* (1996) described a 3D EIT experiment performed with the 64-electrode Sheffield Mark3b system. Their computationally reconstructed images compare very closely with the real objects in the experimental setup.

1997 Cohen-Bacrie *et al.* (1997) adopted a linearized approximation to the forward problem in order to reduce computational load. The tuning parameters for the reconstruction are automatically determined from the measured data. Regularization using a variance uniformization approach yields results similar to Tikhonov regularisation, but with higher sensitivity in the central regions of the 2D volume.

Inversion by (linearized) Fourier transformation was carried out in Cohen-Bacrie *et al.* (1997).

1999 A reconstruction algorithm adapted for data collection on rectangular electrode arrays is presented by Mueller *et al.* (1999).

2000 Siltanen *et al.* (2000) implemented the direct reconstruction method of Nachman for the 2D inverse problem.

2000 The Matlab software package EIDORS for 2D reconstructions in impedance and diffuse optical tomography has been released.

2001 Borcea (2001) investigates a non-linear multigrid method for forward and inverse solution in low-frequency electrical imaging.

2002 The Matlab software package EIDORS for 3D reconstructions in EIT has been released.

2002/2003 Knudsen (2003) discusses a new direct method for reconstructing isotropic conductivities in the plane based on scattering transforms.

Distinguishability & Optimal Current

1986 Isaacson (1986) derived and presented criteria for measuring the distinguishability of two different conductivity distributions. He showed how these criteria can be used to determine the measurement precision needed to distinguish between two differing distributions. The selection of current injection patterns is discussed in the context of achieving maximum distinguishability in the reconstruction.

1996 A neasure of fidelity of an image based on Isaacson's criteria was discussed by Vadasz and Sebestyen (1996).

Measurement error

1988 Breckon and Pidcock (1988) published an article dealing with data errors and their effects on reconstruction algorithms.

1997 Cohen-Bacrie *et al.* (1997) assumed a measurement noise of 20 dB in their reconstructions.

Regularization

1992 The question of determining the regularization parameter has been studied by many authors and a review of several techniques can be found in Galatsanos and Katsaggelos (1992).

1995 Dobson (1997) details a method of "image enhancement" for electrical impedance tomography, in which he bases the recovery of typically blocky images on the total variation regularization technique of Rudin *et al.* (1992).

1997 Vassilevski and Wade (1997) investigate numerical methods for solving inverse problems based on total variation regularization. They conduct several

numerical experiments to compare the effects of various multilevel iterative methods used as pre-conditioners for the conjugate gradient solver used.

1997 Vauhkonen *et al.* (1997) present a new method of incorporating prior information in the EIT reconstruction process by simulating samples of feasible conductivities and thus approximating the prior covariance matrix. This corresponds to a novel method of regularizing the EIT problem based on anatomic information of the body.

1997 Pinheiro *et al.* (1997) compared smoothness-constrained inversion with Levenberg-Marquardt regularization. The results indicate that smoothness-constrained regularization shows superior robustness when noise is present in the measurements.

2002 Borsic (2002) implements Total Variation regularisation and investigates a range of other regularisation methods for electrical imaging.

Linearization Methods

Cohen-Bacrie *et al.* (1997) summarised the different flavours of linearization methods published in the literature and used up to then:

The integral method initially proposed by Chen. Using Born approximation on the inhomogenous factor ($\delta\sigma/\sigma << 1$), the sensitivity matrix S is computed in an analytical manner under the assumption of a circular medium and dipolar current patterns. A more general formulation for a larger class of current input patterns was provided by Dobson and Santosa (1994b).

The sensitivity method developed by Barber and Brown (1984) uses the Geselowitz theorem (Geselowitz, 1971). The computational burden can be high due to the nature of the integrals that need to be evaluated.

The first order approximation of the FEM corresponds to using a linearized approximation of the solution on the FE model around a given initial objective σ_i. In this case, the sensitivity matrix is given by the Jacobian of the FE solution at point σ_i.

The linearization through Fourier coefficients assumes that the medium is circular and analytically derives the expression of the potentials around the object through expansions of Green functions in Fourier series.

Cohen-Bacrie *et al.* (1997) comment that "both the sensitivity method and first order approximation of the FE model require large amounts of computations for the evaluation of the sensitivity matrix."

1990 Kohn and McKenney (1990) found that the solution of variational methods for the inverse problem as presented by Kohn and Vogelius (1987) show best performance in terms of stability and robustness when a Newton-type solver is used. Early termination of the iterative process shows a "desirable" smoothing effect.

Finite Elements in EIT

1959 Duffin (1959) demonstrated that the potential distribution inside a quadrilateral finite element can be solved using an equivalent resistor network.

The FEM has been used by many biomedical engineering researchers. Early FE based work was carried out in cardiology (Kim, 1982), and in defibrillation studies (Kothiyal *et al.*, 1988); in studies of the electric field distribution in human bodies by Natarajan and Seshadri (1976), impedance cardiography (Kim *et al.*, 1988), plethysmography (Batacharya and Tandon, 1988) and in EIT by Murai and Kagawa (1985); Yorkey *et al.* (1987); Liu *et al.* (1988); Wexler (1988); Webster (1990); Hua *et al.* (1991); Woo *et al.* (1993).

1985 Murai and Kagawa (1985) used FE for EIT reconstruction.

1988 A finite element model with node renumbering for adaptive impedance imaging was presented by Woo *et al.* (1988).

1990 Yorkey (1990) investigated the use of higher order polynomial representations of the conductivity in the reconstruction process and demonstrated that (bi)linear conductivity distributions might not be enough to increase resolution. Their results showed that the increase in degrees of freedom causes a large increase in compute time, however, they were not decreasing the number of elements in their original mesh for an increasing polynomial order.

1993 Hua *et al.* (1993) demonstrated how to model the electrode-skin contact in a finite element representation of the boundary of a body.

1994 Woo *et al.* (1994) described a FE based analysis software package for EIT, including a simple interactive graphical mesh generator and fast algorithms for solving linear systems of equations using sparse-matrix techniques.

1994 Schmidt *et al.* (1994) presented a general purpose mesh generator and a method for adaptive mesh refinement for electrocardiography and cardiac defibrillation. They highlight the suitability of adaptive mesh refinement techniques for solving electric field problems in computational medicine.

1994 The work of Johnson and McLeod (1994) addressed the use of mesh adaption based on *a posteriori* error estimates in forward and inverse bioelectric field problems.

1994 Kytömaa and Weselake (1994) investigated the effects of two current projection techniques in combination with a finite element configuration producing a mesh of uniform sensitivity. Their results indicate that the adapted mesh yields superior results. This, however, seems to be due to the increased mesh density at the electrode boundaries rather than the uniform sensitivity.

1995 The use of a range of renumbering algorithms for the system matrix was investigated by Fulton and Lipczynski (1995). The authors compared a natural row-by-row ordering, the minimum degree odering, the irregular nested dissection algorithm and the regular mesh nested dissection ordering with each other. The results show that the regular nested dissection gives best results in terms of factorisation and backsubstitution speed as it has the smallest element fill-in.

1996 The Computational Science Education Project in the USA published an online book entitled "Direct and Inverse Bioelectric Field Problems" (CSEP, 1996), in which the basics of computational bioelectric field modelling are detailed and the potential of future techniques (e.g. adaptive meshing) is discussed.

1997 A fast meshing algorithm using a special binary tree method has been described by Karamete *et al.* (1997). The authors adaptively refine a coarse initial mesh depending on the local element density and thus obtain a method with a linear scaling of total number of nodes in the mesh and computational time.

1997 Borouchaki and George (1997) employed an iterative approach for performing Laplace smoothing, which is used to improve the quality of the finite elements in the domain for numerical simulations. We will show later that Laplace smoothing can be performed using a linear algorithm.

2000 High quality (anisotropic) unstructured meshes can be obtained by ellipsoidal bubble packing as implemented by Yamakawa and Shimada (2000). They present and discuss a computational method for anisotropic tetrahedral meshing of 3D domains by modified bubble meshing in combination with the advancing front method. The advantage of bubble meshing is the high quality of elements in the produced mesh, however, as the distance matrix needs to be computed repeatedly, the computation time can be high.

2000 Schinnerl *et al.* (2000) developed a nested multigrid method for fast numerical computations of 3D Magnetic fields; similar to finite difference multigrid computations, but with a hierarchy of FE discretizations. They compare results from the nested multigrid algorithm with a pre-condicitoned conjugate gradient solver. The results show that for an example involving 1,900,000 degrees of freedom, the solver time can be reduced by an order of magnitude.

EIT Measurement Systems

1987 The development of the Sheffield Mark I system was reported by Brown and Seagar (1987). In 1990 the Sheffield Mark II system came into existence.

A number of systems were reported in the literature for 1990 (Boone and Holder, 1996), major developments followed in 1992 with the OXPACT-II and ACT-III systems.

1994 The year with the most publications on EIT instrumentation and measurement systems. The development of Sheffield Mark III and OXBACT-III fall into this period.

1999 Siemens titled the TransScan TS2000 system as "one of the most important innovations in the diagnosis of breast cancer in the last 25 years" (Siemens, 1999). Although this can be considered part of their marketing strategy, the approval by the FDA in the USA for clinical use shows that there is a niche in the market for this type of device.

Parallelization

1992 Paulson (1992) investigated the possibility of parallelizing algorithms to increase the reconstruction performance in EIT.

1993 Woo *et al.* (1993) developed a modified Newton-Raphson algorithm which uses Hachtel's augmented matrix method (Gjelsvik *et al.*, 1985) for static impedance reconstruction. The subsequent parallelization using a 20 processor *Symmetry* system from Sequent Computer Systems Inc resulted - as expected - in a major speed-up of the reconstruction process.

Electrodes & Measurements

1987 The Sheffield protocol (Brown and Seagar, 1987) allows for $n_L(n_L-3)/2$ independent measurement to be made when n_L is the number of electrodes in the system.

1993 Kyriacou *et al.* (1993) investigate the dependence of the sensitivity matrix on the location of the sensing electrodes on the boundary.

1996 In induced current EIT (ic-EIT), currents are induced into the volume by time-varying magnetic fields produced by coils surrounding the medium. Hence the contact impedance usually occuring by chemical processes under injection electrodes can be neglected (Ruan *et al.*, 1996). The number of measurement in ic-EIT is not determined solely by the number of voltage electrodes, and $(n_L-1)n_C$ measurements can be made where n_L is the number of voltage measurement surface electrodes and n_C is the number of injection coils used.

1997 Paulson *et al.* (1997) presented mathematical models for the modeling of electrodes in EIT.

2000 Generalized Optimal current patterns and electrical safety in EIT are discussed in Lionheart *et al.* (2001).

1.4 Thesis overview

This work addresses the slow reconstruction speed of absolute conductivity images and the currently rather low image resolution in Electrical Impedance Tomography. We will try to improve these factors by introducing and combining special numerical techniques into the reconstruction process of EIT.

To achieve this, we first introduce the basics of electrical impedance tomography, such as the governing physical equation, electrode models, basic theory of inverse problems and the solution of the forward problem in chapter 2.

Chapter 3 deals with the discretization of the derived continuous problem for numerical investigations with finite elements. We then move on to show how adaptive mesh refinement techniques can improve the performance of the forward solution in chapter 4 and we investigate the impact of mesh refinement on the inverse solution in terms of resolution and speed improvements in chapter 5.

In chapter 6, we extend our reconstructions from two-dimensional to three-dimensional objects and introduce a novel conjugate gradient algorithm as alternative to the common non-linear Newton-Raphson iterative solver.

Finally, we summarise our findings and conclusions in chapter 7 and take an outlook on possible future work in 7.2.

1.5 Contributions to the field

The contributions to the field of image reconstruction as detailed in this thesis are as follows:

1. We have employed adaptive mesh refinement methods to focus the available computational resources on regions where they have highest impact on the forward solution. This results in a more efficient 2D reconstruction algorithm with improved accuracy. (Molinari *et al.*, 2001a,d,e,b)
2. Some of the finite element code written has been reused and applied as part of a project on finite element modeling of photonic crystals. (Generowicz *et al.*, 2002)
3. We have devised a method employing adaptive finite elements in the 2D inverse problem which makes the reconstruction independent of the numerical discretization. The resolution is then only limited by the noise of the measurement system. (Molinari *et al.*, 2002b)
4. We have developed a novel conjugate gradient algorithm, incorporating adaptive mesh refinement techniques, to enable large-scale 3D reconstructions (in comparison to Newton-Raphson). (Molinari *et al.*, 2001c, 2002a)

Chapter 2

How does EIT work?

Electrical Impedance Tomography seeks to image the electrical impedance distribution in an inhomogenous medium by applying external sources of electric current and making surface measurements of the resulting electric field.

Figure 2.1 shows a typical experimental set-up for a 2D cross-sectional reconstruction problem. It consists of 16 electrodes attached to the surface of the object under investigation, Ω. In this example, one pair of electrodes is used to inject a

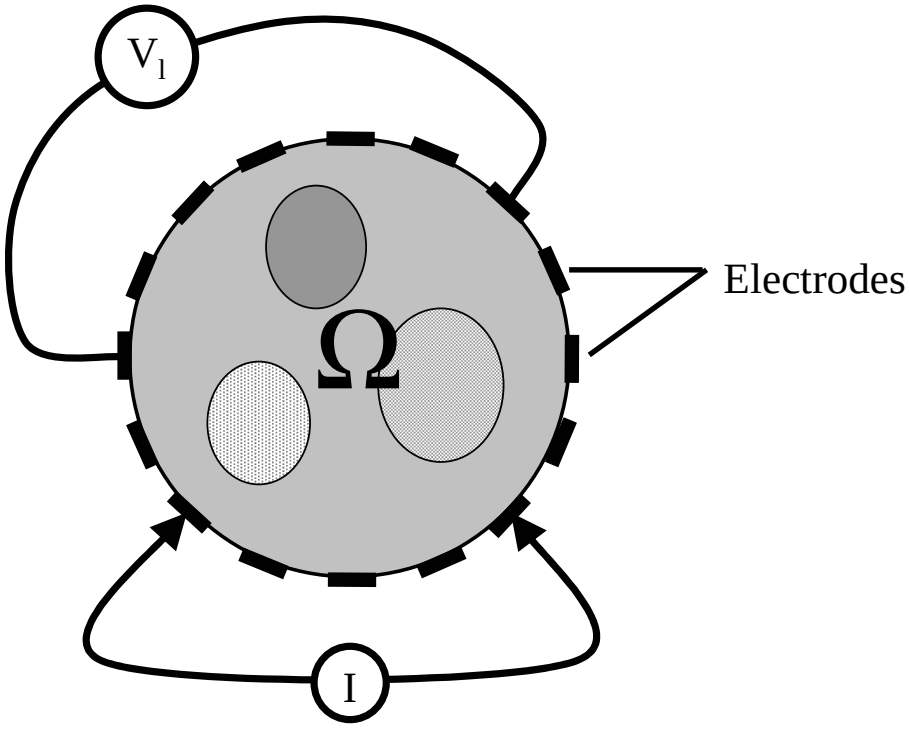

Figure 2.1: Electrical Impedance Tomography experiment. Measurement of the resulting potential at surface electrodes V_ℓ after current I is injected into object Ω.

small time-harmonic current I of frequency ω into the object. The resulting potential distribution ϕ within Ω is then measured at the remaining surface electrodes,V_ℓ.

An initial estimate of the contained material is updated iteratively on a computer so that the application of the measurement procedure to the model yields the real measurements as closely as possible. This leads to a conductivity image which is assumed to resemble the real distribution. The evaluation of the correctness of this image has to be performed carefully since the ill-posedness of the problem allows for several conductivity distributions giving similar potential measurement at the electrodes.

To model the processes taking place when a current is injected into the body, we need to know the behaviour of electric and magnetic fields within our object under investigation or the biological tissue respectively. We will derive the equations of EIT starting from first principles, applying simplifications and defining appropriate boundary conditions as imposed by the electrodes. EIT measurements will be presented and we will detail some of the theory behind the solution of the forward and the inverse problem.

2.1 The physical model

The electromagnetic field within a body Ω is governed by the well-known Maxwell Equations, for which Jackson (1998) gives an excellent introduction. They have been studied in the context of EIT by, for example, Ackermann (1962) and Doerstling (1995):

$$\nabla \times \mathbf{E} = -\frac{\partial \mathbf{B}}{\partial t} \tag{2.1}$$

$$\nabla \times \mathbf{H} = \mathbf{J} + \frac{\partial \mathbf{D}}{\partial t}. \tag{2.2}$$

The electric displacement $\mathbf{D}$ and the magnetic induction $\mathbf{B}$ can be expressed in terms of the electric field $\mathbf{E}$ and the magnetic field $\mathbf{H}$ as:

$$\mathbf{D} = \epsilon\mathbf{E} \tag{2.3}$$

$$\mathbf{B} = \mu\mathbf{H}, \tag{2.4}$$

where ϵ and μ denote the electrical permittivity and magnetic permeability respectively. In EIT, these parameters are generally considered isotropic although Geddes and Baker (1967) have shown that some tissues behave, in fact, highly anisotropically (for example muscle tissue as present in the heart.) At this stage, we follow the common assumption of isotropic ϵ, μ and electric conductivity σ and leave the anisotropic case for further studies. Substituting the current density as $\mathbf{J} = \sigma\mathbf{E}$ and applying the plane-wave definitions for the electric field, $\mathbf{E} = \hat{\mathbf{E}}e^{i\omega t}$, and the magnetic field, $\mathbf{B} = \hat{\mathbf{B}}e^{i\omega t}$, equations (2.1) and (2.2) can be rewritten into the form

$$\nabla \times \mathbf{E} = -i\omega\mu\mathbf{H} \tag{2.5}$$

$$\nabla \times \mathbf{H} = \mathbf{J} + i\omega\epsilon\mathbf{E}. \tag{2.6}$$

The two components forming $\mathbf{J} = \mathbf{J_o} + \mathbf{J_s}$ are the current density caused by ohmic current $\mathbf{J_o} = \sigma\mathbf{E}$, and the current density resulting from internal sources, $\mathbf{J}_s$, such as brain or heart activity. $\mathbf{J}_s$ can be neglected for the frequency range used in EIT studies. Thus we obtain the Maxwell Equations applicable to EIT in the form

$$\nabla \times \mathbf{E} = -i\omega\mu\mathbf{H} \tag{2.7}$$

$$\nabla \times \mathbf{H} = (\sigma + i\omega\epsilon)\mathbf{E} \tag{2.8}$$

Nunez (1981) and Vauhkonen (1997) showed that it is valid for biological tissue to neglect the electric field contributed by magnetic induction and hence use the

definition of $\mathbf{E}$ under quasi-static conditions,

$$\mathbf{E} = -\nabla\phi, \tag{2.9}$$

where ϕ is the electric potential. Substituting equation (2.9) into equation (2.8) and taking the divergence of both sides yields

$$\begin{aligned} \nabla \cdot (\nabla \times \mathbf{H}) &= \nabla \cdot (\sigma + i\omega\epsilon)\mathbf{E} && (2.10) \\ 0 &= \nabla \cdot (\sigma + i\omega\epsilon)\nabla\phi. && (2.11) \end{aligned}$$

Hence the governing equation for Electrical Impedance Tomography inside the body Ω becomes

$$\nabla \cdot (\sigma + i\omega\epsilon)\nabla\phi = 0. \tag{2.12}$$

Applying low frequency or direct currents ($\omega \approx 0$) reduces equation (2.12) to the governing equation for Electrical Resistance Tomography (ERT), which is often referred to as the governing equation for EIT and which we will use throughout the thesis:

$$\nabla \cdot (\sigma\nabla\phi) = 0. \tag{2.13}$$

The approximation is valid as long as ω is within a range of approximately 0-10 kHz in which biological tissue exhibits distinct conductivity values as shown in figure 2.2. Even at certain higher frequencies the capacitive term can be neglected according to Nunez (1981); Barber and Brown (1984) and Webster (1990).

2.1.1 Current density from MR-EIT

The latest method to obtain the current density within a body is to perform current injection while the object is in a MR scanner. This method is called MREIT and is a research field on its own. The spatial resolution of the current density image is comparable with that of an MRI image. For further details see, for example, Eyüboglu *et al.* (2000) or Kwon *et al.* (2002).

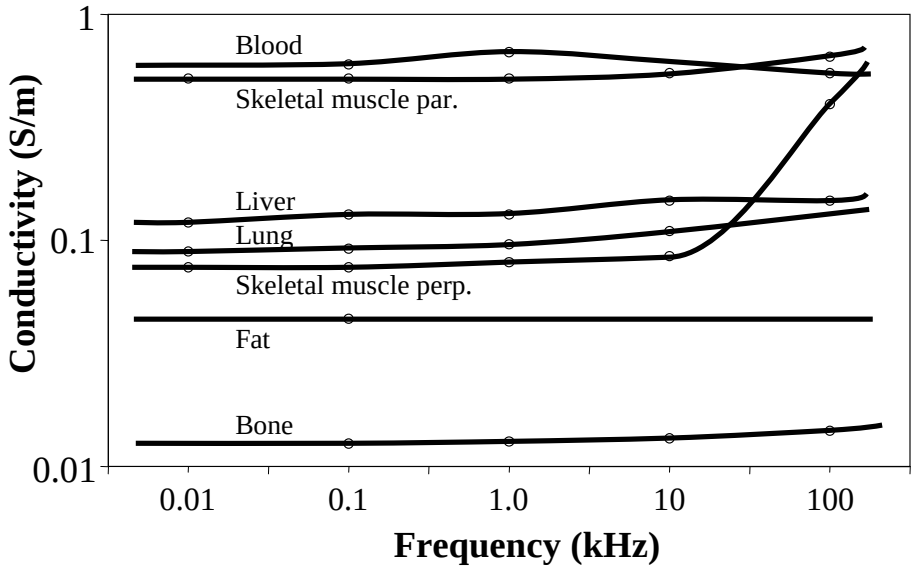

Figure 2.2: Electrical conductivity of human tissue at different current frequencies. The discrete points shown are averaged values from Foster and Schwan (1989). The low frequency range of 0-10 kHz is most suitable for medical imaging purposes as biological cells exhibit their most distinct differing conductivities in this frequency range.

2.2 Electrode models and boundary conditions

Equation (2.13) is a second order elliptic partial differential equation (PDE) in ϕ. For a unique solution to exist, the definition of boundary conditions (BC) is required. The BCs for this PDE depend on the electrode type used and the model assumed for its behaviour (Cheng *et al.*, 1989; Somersalo *et al.*, 1992).

The continuum model

The most simplistic case for the BCs would be to use the *continuum model* which does not take into account the presence of electrodes. The current density j applied in normal inward direction $\mathbf{n}$ to the object's surface, $\partial\Omega$, is then defined as

$$j = \sigma \frac{\partial \phi}{\partial \mathbf{n}} \qquad \text{on } \partial\Omega. \tag{2.14}$$

Cheng *et al.* (1989) showed that this model overestimates the resistivities by as much as 25 % and is hence not applicable to EIT reconstructions.

The gap model

Though the alternative *gap model* does account for the presence of N_L electrodes and assumes the injection of the current I_ℓ into electrode number ℓ with area S_ℓ,

$$j = \frac{I_\ell}{S_\ell} \qquad \ell = 1, 2, \ldots, N_L \tag{2.15}$$

$$j = 0 \qquad \text{in gaps between the electrodes,} \tag{2.16}$$

it is not much more accurate than the continuum model. This is due to the fact that both ignore the shunting effect of the electrodes and the contact impedance caused by electrochemical reactions at the gel interface between body skin and electrodes.

The shunt model

The shunting effect is represented by the *shunt model* which assumes a constant measured potential V_ℓ across electrodes,

$$\phi = V_\ell \quad \text{on } S_\ell \qquad \ell = 1, 2, \ldots, N_L, \tag{2.17}$$

and uses the more reliable boundary condition for current injection,

$$\int_{S_\ell} \sigma \frac{\partial \phi}{\partial \mathbf{n}} ds = I_\ell \qquad \ell = 1, 2, \ldots, N_L. \tag{2.18}$$

The complete model

While the former two models overestimate the resistivity, the latter model underestimates it because it still does not take into account the contact impedance (Cheney *et al.*, 1999). The electrochemical effect that takes place between the electrode and the body is the formation of a thin and highly resistive layer. This layer is characterized by the *contact impedance* z_ℓ. Typically, z_ℓ is in the range $200 - 400\Omega\text{cm}^2$ (Heimbach, 1990).

Accounting for z_ℓ results in replacing equation 2.17 by

$$\phi + z_\ell \frac{\partial \phi}{\partial \mathbf{n}} = V_\ell \qquad \ell = 1, 2, \ldots, N_L. \tag{2.19}$$

Somersalo *et al.* (1992) have shown that this *complete model* is able to predict the experimental measurements to better than 0.1 % which is in the region of the noise-to-signal ratio common to current measurement systems and thus the most appropriate electrode model for EIT reconstruction.

For existence and uniqueness of a solution to equation (2.13), all the described models require the additional formulation of the following two Kirchhoff conditions:

$$\sum_{\ell=1}^{N_L} I_\ell = 0 \qquad \text{conservation of charge} \tag{2.20}$$

$$\sum_{\ell=1}^{N_L} V_\ell = 0 \qquad \text{choice of a ground.} \tag{2.21}$$

2.2.1 The complete formulation

We will employ the complete electrode model throughout this thesis. For convenience, we summarize the complete set of equations on which the EIT forward solution and reconstruction process will be based in chapters 4 to 6:

$$\nabla \cdot (\sigma \nabla \phi) = 0 \qquad \text{governing equation} \tag{2.22}$$

$$\int_{S_\ell} \sigma \frac{\partial \phi}{\partial \mathbf{n}} ds = I_\ell \qquad \text{current injection, vonNeumann BC} \tag{2.23}$$

$$\sigma \frac{\partial \phi}{\partial \mathbf{n}} = 0 \qquad \text{gaps between the electrodes} \tag{2.24}$$

$$\phi + z_\ell \frac{\partial \phi}{\partial \mathbf{n}} = V_\ell \qquad \text{potential measurement, Dirichlet BC} \tag{2.25}$$

$$\sum_{\ell=1}^{N_L} I_\ell = 0 \qquad \text{conservation of charge} \tag{2.26}$$

$$\sum_{\ell=1}^{N_L} V_\ell = 0 \qquad \text{choice of ground.} \tag{2.27}$$

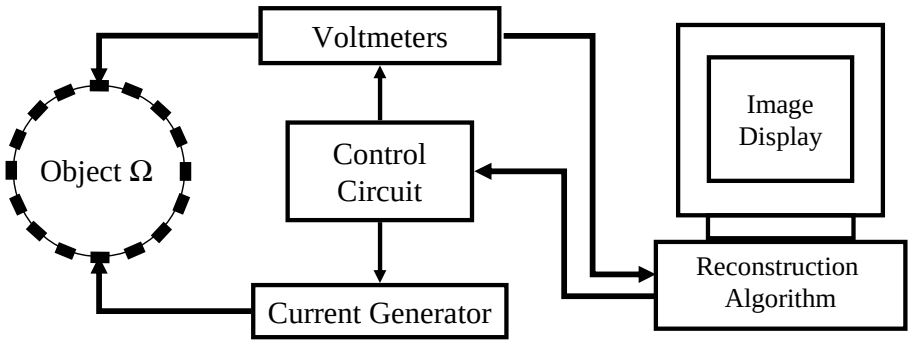

Figure 2.3: Electrical Impedance Tomography system. See text for explanation of devices.

2.3 EIT measurements

EIT data acquisition, which consists of current injection and subsequent measurement of the resulting electrode potentials, can be performed in many different ways. What hardware to use and how to carry out the measurements in order to obtain the best possible resolution and a stable reconstruction is an important question in EIT (Dobson and Santosa, 1994b). Different strategies for current injection have been investigated by Hua *et al.* (1992) and optimal voltage measurement schemes are discussed in Paulson *et al.* (1993).

In order to achieve a unique result, an infinite number of measurements of infinite precision is required (Sylvester and Uhlman, 1987).

2.3.1 Measurement hardware

Figure 2.3 shows the main parts of an electrical impedance imaging system. It comprises of a number of current generators and voltage measurement devices connected to electrodes on the surface of the body. A control circuit switches/assigns the electrodes to the current generator and voltmeter input and output. When only one generator is present, only two electrodes at any one time can be used for current injection. If more than one voltmeter is present, the voltage measurements can be made in parallel and hence shorter acquisition times can be achieved. The computer is used to control the measurement process and to store, process and visualize the data. See Webster (1990) for more details about the hardware of EIT measurement systems.

2.3.2 Current patterns

Current can be injected either through a few electrodes or through many/all electrodes at the same time. The set of the combinations of electrodes involved and the amplitudes of the currents applied in each set form a *current pattern*. Main current patterns – as described in Vauhkonen (1997) – are:

- the *neighbouring pattern*, where current is injected through neighboured electrodes and voltage is measured at the remaining electrodes. This technique was initially used by Barber and Brown (1984) with backprojection reconstructions and corresponds to the presence of pseudo-dipoles along the boundary.
- the *opposite pattern*, where current is injected through electrodes on opposite sides of the object's surface. This method deploys a more uniform current density in the center of the object and hence results in increased sensitivity in that region.
- the *cross pattern*, which uses one electrode as current reference electrode and all the others in turn for injection. The voltages are measured with respect to one reference electrode.
- the *optimal pattern*. Hua *et al.* (1991) derived optimal current patterns by adapting the reconstruction algorithm used to minimize the difference between measured potential values and those predicted by the model. In this case, current of adapted amplitude is driven through all electrodes at the same time which leads to increased sensitivity to conductivity changes.
- the *trigonometric pattern*. Paulson *et al.* (1993) and others (Vauhkonen *et al.*, 1999; Cheney *et al.*, 1999) use trigonometric current patterns where the amplitude of the injected current, I_0, varies with the angular position θ_ℓ of the electrode ℓ on the boundary of a circular plate: $I_\ell = I_0 \cos(\theta_\ell)$. The advantage is the more evenly distributed current density within the object and the increased sensitivity in the center of the object.

Throughout the course of this thesis, we will use the neighbouring measurement pattern which corresponds to $N_{cp} = N_L - 1$ linear independent current injections

and a total of $N_M = \frac{N_L(N_L-3)}{2}$ independent voltage measurements, where N_L is the number of electrodes used.

When performing 3D impedance imaging, the current patterns can not be as easily differentiated as in 2D. The best approach in this case is to use the optimal pattern as it adapts the measurement to the object's properties.

2.3.3 Measurement error

All physical measurements carry measurement errors caused by random and systematic error sources. *Random errors* originate in the measurement electronics and often cannot be avoided. The reduction of thermal fluctuations and digital quantization error can be performed by using electronic parts of high specification. When living systems are investigated, noise is often caused by physiological changes within the body during the measurement period. Sources of *systematic errors* are manifold and start with simple mislocation of electrodes, the interchange of electrode connections, and others. They often include errors caused by inaccurate geometrical or numerical modelling. Systematic errors usually scale with the size of the measurements and there are often ways of identifying these, for example by applying the reciprocity theorem[1]. Meeson *et al.* (1996) showed that this reciprocity may be used to measure noise performance and to check the quality of data.

2.4 The forward and the inverse problem

The classical *forward* or *direct problem* consists of finding a unique effect resulting from a given cause through a known mathematical or physical model. This type of problem is usually well-posed in the sense of Hadamard (1923), and as given by Lamm (1993):

1. There exists a (globally-defined) solution for all reasonable data;
2. The solution is unique;
3. The solution depends continuously on given data (stability).

Many physical situations satisfy these conditions of *existence*, *uniqueness* and *stability* and are hence well-posed. However, there exists a large class of problems

[1] If a voltage source S acting in one branch of a network causes a current I to flow in another branch of the network, then the same voltage source S acting in the second branch would cause an identical current I to flow in the first branch (Geselowitz, 1971).

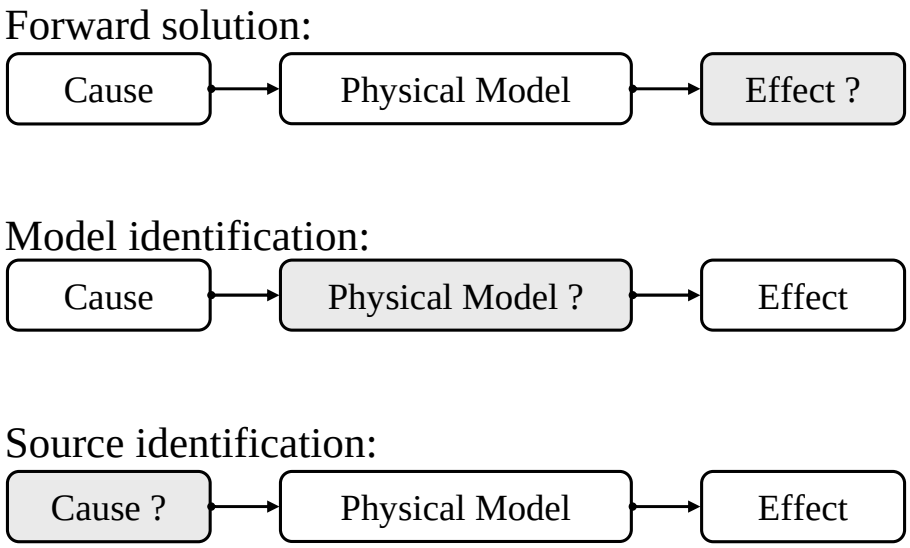

Figure 2.4: Classification of inverse problems. Top: Forward problem – cause and model are known, effects are sought. Centre: Model identification problem – cause and effect are known. Bottom: Source identification problem – model and effect are known.

in science and technology which are not necessarily well-posed (Groetsch, 1993). These problems are *inverse* to the classical forward problem and do not necessarily have unique solutions or the solutions may be very sensitive to small changes in data (or very insensitive to large changes in data).

2.4.1 Problem classification

Figure 2.4 shows the 3 different classes of numerical simulations where an unknown quantity needs to be determined from a set of known parameters.

The top model shows the solution of the so-called forward problem. Most numerical solutions to questions in the physical and engineering science are solutions of the forward problem, where the causes and physical model are known and the resulting effects need to be found. In the case of EIT, this corresponds to the computation of the electrode potentials when the current injection is given and the conductivity distribution is known.

The middle row represents the typical problem in EIT, the model identification problem. In this case, the cause – the injected current – is known, as well as the effect – the measured electrode potential – however, most of the physical model is unknown.

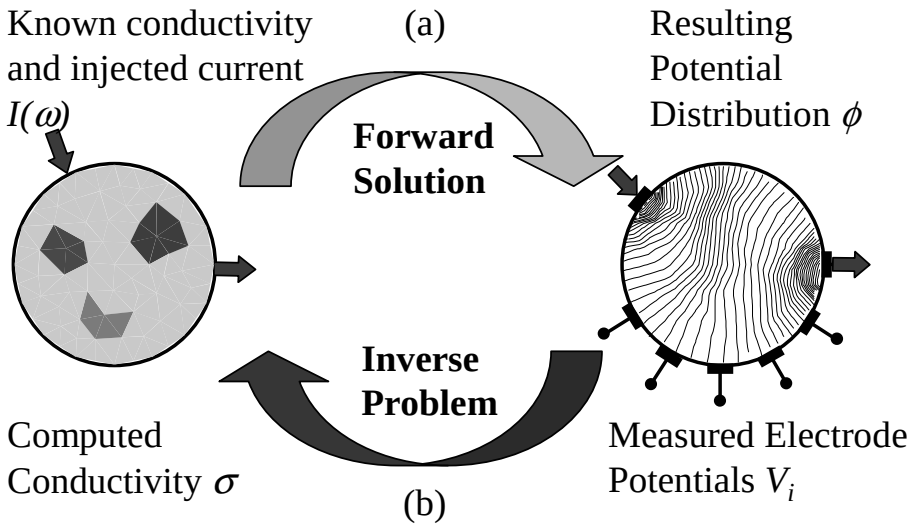

Figure 2.5: (a) In the forward solution, the potential ϕ is sought whereas in the (b) inverse problem the physical model based on the conductivity distribution has to be determined.

Finally, the model in the bottom row shows the source identification problem. This problem is encountered, for example, in Electrical Encephalographic (EEG) reconstructions of the current dipoles in the brain when surface potentials can be measured and the brain tissue conductivities are assumed known.

Although the reconstruction of conductivity distributions in EIT is of the model identification problem class, the solution of the forward problem is a central part of many iterative solvers. One of these iterative solution methods is outlined in figure 2.5. In the remaining chapters of this thesis, we will show the implementation of such an iterative solver incorporating a solution to the forward problem and solving the inverse model identification problem.

2.4.2 Forward solution

The typical *forward problem* in EIT is as follows: Given the conductivity distribution σ and the currents injected through boundary electrodes, $\mathbf{I}$, find the potential distribution ϕ within the object Ω and in particular the resulting voltages at the potential measurement electrodes, $\mathbf{V}$, see figure 2.5a.

The solution of the forward problem is rather simple as it only requires solving the linear system

$$\nabla \cdot \sigma \nabla \phi = 0 \tag{2.28}$$

for ϕ in Ω together with the application of the boundary conditions imposed by the current injection and subsequent determination of the electrode voltages $\mathbf{V}$. This formula can be rewritten as an operator equation,

$$\mathcal{Y}(\sigma)\phi = j, \tag{2.29}$$

where $\mathcal{Y}(\sigma)$ is known as the conductivity-dependent *Dirichlet-to-Neumann map* and j is the current density applied trough boundary conditions. We will see in the next chapter how this operator is derived and expressed in a discrete form on a finite element mesh.

2.4.3 Theory of inverse problems

The actual challenge for using this method for tomographic purposes is the *inverse problem*, which is based on the inverse *model identification* problem as follows: Given the injected currents $\mathbf{I}$ (the causes) and the corresponding voltages at the potential measurement electrodes $\mathbf{V}$ (the effects), find the conductivity distribution σ (the physical model) within Ω.

The transfer impedance model can be described by the operator $\mathcal{R} = \mathcal{Y}^{-1}$ which projects the current densities injected through the electrodes, j, onto the potential distribution ϕ which we measure on the electrodes, $\mathbf{V}$, see figure 2.5b.

In this case, equation (2.28) turns out to be non-linear in σ as the potential ϕ is a function of the conductivity, $\phi = \phi(\sigma)$,

$$\nabla \cdot \sigma \nabla \phi(\sigma) = j \tag{2.30}$$

and hence we cannot easily solve this equation for σ.

In fact, equation (2.30) can not be solved analytically for arbitrary σ's and thus requires the application of appropriate numerical techniques. In order to obtain a numerical solution to the continuous problem, the solution domain needs to be discretized into small elements, on which a solution is then approximated.

In general, it can be said that to obtain the image of an unknown interior of an object, we have to create a numerical model on which the simulation of the potential measurement is approximated as closely as possible to the real measurement. The model of an initial conductivity distribution is then adaptively changed to match the physical properties of the original object so that the calculated effects (electrode potentials) match the real measurements.

There are other methods to deal with this type of ill-posed inverse problem. A non-exhaustive list of these as applied to inverse problems in recent years, is for example:

- stochastic reconstruction (Maximum entropy)
- non-linear iterative reconstruction
- linearized reconstruction
- direct reconstruction (Nachman)
- backprojection algorithms

The classical forward problem is to find a unique effect of a given cause by using an appropriate mathematical or physical model. This class of problems is usually well-posed, which means that it has a unique solution and the solution is insensitive to small changes in the data. Traditionally, it was thought that all physical situations lead to well-posed problems, but today we know that many problems in science and technology are not necessarily well-posed. These problems are *inverse* to the classical forward problems. There exist two different types of inverse problems: (1) The *source identification* problem where the model is given, the effects can be measured and the unknown cause is sought, and (2) the *model identification* problem where cause and effect are known and the physical model is sought. These inverse problems do not necessarily have unique and stable solutions and small changes in the data can cause large variations in the solution. For this reason, inverse problems are called *ill-posed* or *ill-conditioned* respectively in the sense of Hadamard (1923).

In this chapter, some topics in the field of inverse problems are reviewed and solution strategies discussed. The focus is on the model identification problem as Electrical Impedance Tomography belongs to this class of ill-posed problems. The

major solution methods can be categorized as deterministic and statistical methods. It is assumed that the physically continuous problem has been discretized and the discussion is therefore based on a finite-dimensional system. From a mathematical point of view is the discrete problem always well-posed because arbitrarily small changes in the data cannot cause arbitrarily large variations in the solution. However, finite dimensional discrete problems have properties very similar to those of continuous ill-posed problems and it is therefore natural to consider only finite-dimensional problems.

2.4.4 Deterministic method

Consider the equation

$$o = h(p), \tag{2.31}$$

where $o \in \mathbb{R}^M$ denotes the M observations or measurements, and h represents the physical model which is depending on the physical parameter vector $p \in \mathbb{R}^N$ of size N.

If the model h is linear with respect to p, equation 2.31 can be written in the form of a linear matrix equation,

$$o = Hp, \qquad H \in \mathbb{R}^{M \times N}. \tag{2.32}$$

If h or H are known, the effect o can be calculated for a given p. This is the classical forward problem which is usually stable and has a unique solution. In the model-identification inverse problem, the observation o is measured and the physical model h is to be determined. The observations are usually measured with a certain error. Is the problem ill-posed, the solution p can be very sensitive to these small errors and hence vary in a wide range. This behaviour of ill-posed inverse problems corresponds to an ill-conditioning in H. The condition number of the matrix H is calculated as ratio between largest and smallest non-zero singular value of H:

$$\kappa(H) = \frac{\max(svd(H))}{\min(svd(H))} = \|H\|\|H^+\| = \frac{\gamma_1}{\gamma_r}. \tag{2.33}$$

H^+ is the Moore-Penrose inverse of H, γ_1 is the largest singular value of H and γ_r is the smallest non-zero singular value of H. r denotes the numerical rank of H. The larger the condition number, the more ill-conditioned the problem is.

2.4.5 Non-linear least squares

In practice, a general solution is sought which minimizes the difference between observations and measurements simulated on the numerical model.

In cases where the number of measurements, M, equals the number of unknown parameters, N, a simple inversion of the model matrix H would be sufficient to determine p. For the case of underdetermined systems ($M < N$) or overdetermined systems ($M > N$) a *best fit* solution needs to be found.

One method to find such a solution is to use (weighted) least squares. The vector p is called the weighted least squares solution if it solves the problem

$$p = \min\|Lo - Lh(p)\|_2^2. \tag{2.34}$$

$W = L^T L$ is the so-called *weighting matrix*.

If $h(p)$ is a non-linear function, there exist several possibilities to solve equation 2.34. If the non-linearity of the problem is weak, the model $h(p)$ can be linearized around p_0 according to a Taylor series expansion:

$$h(p) = h(p_0) + \frac{\partial h}{\partial p}(p_0)(p - p_0) + \mathrm{o}(\|p - p_0\|), \tag{2.35}$$

where $\partial h(p_0)/\partial p$ is referred to as the Jacobian, J, of $h(p)$ at $p = p_0$. Neglecting higher order terms and rearranging then yields

$$h(p) - h(p_0) = J(p - p_0). \tag{2.36}$$

With $\Delta p = (p - p_0)$, and $\Delta o = h(p) - h(p_0)$, we obtain

$$J\Delta p = \Delta o. \tag{2.37}$$

This equation represents the linearized relation between a change in parameter p with respect to a change in the observation o in the vicinity of the local point p_0. The least-squares solution to this linearized equation can now be obtained with the help of the *Moore-Penrose inverse* or *pseudoinverse* of H:

$$\Delta p = H^+ \Delta o, \tag{2.38}$$

where

$$H^+ = (J^T W J)^{-1} J^T W. \tag{2.39}$$

Here, Δp now represents the parameter update required based on the observation difference Δo when J is determined by the physical model. If H has a trivial null space, $\{y \in \mathbb{R}^N | Hy = 0 \quad \text{for} \quad y = 0 \quad \text{only}\}$, then the solution is unique. Cases with non-trivial null space as in the case of measurement noise require regularisation and will be considered later.

Sylvester and Uhlman (1987) proved that the Dirichlet-to-Neumann map uniquely determines C^2 conductivities for this type of boundary-value problem which was identified first by Calderon (1980). The proof outlines a direct method for reconstructing the conductivity under the assumption that the measurement data are exact.

2.5 Image smoothness constraint

The reformulation of the problem yields a well-posed problem instead of an ill-posed problem. So far we have started from the assumption that the difference in measured (V_ℓ) and computed (U_ℓ) electrode voltages has to be minimized under the assumption of measurement noise. We assume that the set of measurements made and the error on these follows a Normal distribution and we can thus scale

the voltage values by the variance of the voltage set as measurement noise ($\delta V_\ell = (var)(V_\ell)$).

This leads to the formulation of the objective function

$$\Phi(\sigma) = ||Y^{-1}(\sigma)\mathbf{I} - \mathbf{V}||^2 \tag{2.40}$$

$$\sigma = \text{argmin} \left\{ \sum_{\ell=1}^{N_L} \left(\frac{V_\ell - U_\ell}{\delta V_\ell} \right)^2 \right\} \tag{2.41}$$

or in Lagrangian formulation:

$$\text{minimize} \quad \sum_{\ell=1}^{N_L} \left(\frac{V_\ell - U_\ell}{\delta V_\ell} \right)^2 . \tag{2.42}$$

However, Pinheiro *et al.* (1997, p.301) demonstrated that "Fitting data rather than noise is a necessary requirement in order to reconstruct meaningful images. The use of a smoothness-constrained model is a means to obviate this problem. It has been shown that the smoothness-constrained regularization is superior to the [Levenberg-Marquardt method] in stabilizing the inversion procedure". Smoothness-constrained inversion is also often referred to as Occam's inversion in the geophysical literature (Constable *et al.*, 1987).

The idea behind this inversion technique is that, rather than fitting the experimental data as closely as possible which maximizes the roughness of the model, the smoothest model is sought which fits the data to within an expected tolerance.

The Levenberg-Marquardt method tries to stabilise the problem by adding a matrix with small diagonal elements ($\epsilon\mathbb{1}$) to the Hessian approximation $J^T J$.

Often, the Tikhonov regularization method is used to stabilize the problem and to make it more well-posed in terms of the singular value decomposition (SVD) components and the matrix conditioning. Tikhonov regularization can be written as

$$\sigma = \text{argmin} \left\{ \sum_{\ell=1}^{N_L} \left(\frac{V_\ell - U_\ell}{\delta V_\ell} \right)^2 + \lambda ||\sigma|| \right\} \tag{2.43}$$

or in Lagrangian formulation:

$$\text{minimize} \quad \sum_{\ell=1}^{N_L} \left(\frac{V_\ell - U_\ell}{\delta V_\ell} \right)^2 \quad \text{under the condition} \quad ||K\sigma|| < \epsilon, \tag{2.44}$$

with K being the matrix representation of a linear integral operator.

The conditioning of the problem is now influenced by the Lagrange parameter λ. The size of this factor balances between a large contribution of the constraint (λ large) or a large contribution of the original term ($\lambda \to 0$).

2.5.1 χ^2 fitting

We address the problem of conditioning the problem by minimising a χ^2 functional under the condition of image smoothness. The χ^2 method has been applied for many years in the physical and engineering sciences where statistical measurements of data are taken repetitively. The mean value and the standard deviation of these repetitive measurements give an indication of how well the measured data is approximated by the simulated data when measurement error (represented by the standard deviation) is present.

Let $o_i + \delta o_i$ be a set of observations of size $N_O (i = 1 \dots N_O)$. These observations deviate from the "exact" theoretically predicted value o_i by an error of δo_i. Repetitive measurement ($m = 1...M$) of these observations result in a set of measurements, $\mathcal{M} \in \mathbb{R}^{N_O \times N_M}$, from which mean observations $\bar{o}_i$ and their standard deviations $\delta \bar{o}_i$ can be derived.

To obtain a measure of how well the observed values match a set of computed observations $\tilde{o}_i$, their difference should be within the error limits of $\pm \delta \bar{o}_i$, i.e.

$$(\tilde{o}_i - \bar{o}_i)^2 \leq \delta \bar{o}_i^2 \tag{2.45}$$

or

$$\left(\frac{|\tilde{o}_i - \bar{o}_i|}{\delta \bar{o}_i} \right)^2 \leq 1. \tag{2.46}$$

If we sum up all contributions, we obtain an expression for a good fit of the computed observations to the real observations in the χ^2 sense:

$$\chi^2 = \sum_{i=1}^{N_O} \left(\frac{\tilde{o}_i - \bar{o}_i}{\delta \bar{o}_i} \right)^2 \leq \sum_{i=1}^{N_O} 1 \tag{2.47}$$

$$\chi^2 = \sum_{i=1}^{N_O} \left(\frac{\tilde{o}_i - \bar{o}_i}{\delta \bar{o}_i} \right)^2 \leq N_O. \tag{2.48}$$

This assumes that all measurements carry an error $\neq 0$. If the computed observations now fall within the error limits of the real observations, the criterion $\chi^2 \leq N_O$ is satisfied and a *best fit* computed solution to the problem is found.

There obviously exist a number of possible solutions which all satisfy the χ^2 goodness-of-fit criterion.

2.6 Summary

In this chapter, we have introduced the physical principles behind Electrical Impedance Tomography and detailed electrode models and current injection patterns. We have discussed the basics of solving the forward problem and given an introduction to the different types of inverse problems and their solution method which we will apply in this thesis. The next chapter will take the continuous model we have developed and we apply the finite element method as discretization method for numerical computation.

Chapter 3

The Finite Element Method in EIT

In the engineering sciences there exist many different types of electro-magnetic field problems which are simulated and solved numerically with computers. From the most common numerical techniques as listed in Schwab (1998),

- FDM - the finite difference method,
- BEM - the boundary element method,
- FEM - the finite element method,
- SC - simulation charges, and
- MCM - the Monte-Carlo method,
- FVM - the finite volume method,

the finite element method is the most applicable method for complex geometries and non-trivial boundary conditions (Burnett, 1987; Bathe, 1982; Silvester and Ferrari, 1996; Salazar-Palma *et al.*, 1998). In EIT, it provides piecewise solutions for both the approximation of the potential and the determination of conductivities (Miller and Henriquez, 1990) and hence we will mainly apply this technique for the required computations throughout this document.

The FDM - although reasonably simple and fast - is restricted to pointwise solutions on a pre-defined and usually square grid and hence cannot cater for the arbitrary boundaries of complex geometries such as those of tissue within the human body. The BEM is more suitable for problems where there are few regions of homogenous conductivity with well-known boundaries within the body, which are often unavailable in the case of EIT reconstruction. Simulation charges can be

applied to model electrostatic fields if the current source and - once again - the conductivity were known. The Monte-Carlo method is a powerful technique based on statistical sampling of the electro-magnetic field. This interesting method, however, often requires too much computation time compared to other methods.

The finite element method was first used by Courant (1943) for vibrational studies in mechanical engineering. Some sources (Williamson, 1980) cite Schellbach (Schellbach, 1851) as first application of finite element analysis since he determined a surface of minimum area enclosed by a given closed boundary curve with a finite element-like solution.

The finite element solution to a problem, set up by a PDE and additional boundary conditions, consists of the following steps (Burnett, 1987):

1. *Discretization* of the object volume/field area into single elements,
2. *Approximation* of the potential function ϕ within a single element,
3. *Determination* of the elemental matrices,
4. *Assembly* of the system matrix (or transfer matrix, stiffness matrix),
5. *Boundary condition* imposition, and
6. *Solution* of the (linear) set of equations.

3.1 Discretization & Meshing

To allow for numerical calculations, we need to divide the domain Ω into a finite number of elements – this process is known as meshing.

Numerical simulations can only produce accurate results if the discretization of the volume under investigation is chosen suitably for the applied numerical algorithm. In EIT, a poor discretization might yield inaccurate results since it affects several steps of the reconstruction process at once (forward solution, inverse problem, final visualisation). In particular the effects of the discretization on the accuracy of the predicted voltages on the boundary and the effects on the sensitivity due to conductivity change in the interior are highly significant in this field.

There are a number of factors in the discretization process which need to be taken into account for any numerical simulation and we will address the issues involved in the following sections:

- Meshing software
- Element geometry
- Element & mesh quality
- Element size and density
- Mesh smoothing
- Boundary model accuracy (shape & electrode modelling)
- Node numbering
- Algorithms and computational implementation (bubble, vertex)

3.1.1 Meshing software

The discretization of the object Ω into elements can be performed using publicly available software, for example: Easymesh (Niceno, 2001) or Triangle (Shewchuk, 1996) for two-dimensional areas; and Gmesh (Geuzaine and Remacle, 2000), Geompack (Joe, 1996), Netgen (Schöberl, 2001) or the well-known QHull package (Barber *et al.*, 1996) for three- and higher-dimensional volumes.

These packages are usually based on Octree, Divide-and-Conquer or Advancing Front techniques (Thompson *et al.*, 1999) in combination with Delaunay triangulation algorithms (Delaunay, 1934). Some of these can produce very irregular meshes which contain non-equilateral elements with rather sharp angles, which should in general be avoided as they can distort the numerical solution unnecessarily.

An alternative to these approaches is to write software which is based on physical techniques such as, for example, *bubble meshing* (Cingoski *et al.*, 1997), spring meshing, or a Vortex-based method (Fangohr *et al.*, 2001). If more structured meshes are required, a simple way of creating such a mesh is to fill the domain (defined by its fixed boundary) with a structured/regular mesh and to subsequently adjust this to the boundary shape by smoothing it (see 3.1.7).

Good mesh generators should be able to meet the following criteria:

User Input
- ability to accurately define boundaries
- possibility to specify a node or element density function
- allowing for remeshing of existing meshes

Meshing

- conform to complex boundary
- create unstructured mesh to avoid anisotropies
- create elements with high quality
- generate element density according to user input
- perform automatic computation without the requirement for user interaction
- carry out fast construction of meshes
- be robust: creation of valid meshes

Output

- restricted to useful and meaningful parameters, such as topology and node positions
- possibility of choosing different output structures (topology, edge connection, etc.)

The Handbook of Grid Generation (Thompson *et al.*, 1999) and the Meshing Research Corner (Meshing Research Corner, 2001) are valuable resources, presenting and discussing many different methods for the generation of finite element meshes.

However, it seems that many researchers make use of meshing programs without considering the impact of unsuitable volume discretizations on the reconstruction.

We have found that mesh generation based on physical principles gives the best results in terms of element shape and grading. In particular, we have employed two novel methods of generating high quality meshes fitted to a given mesh density: (a) a modified version of bubble meshing (Cingoski *et al.*, 1997) and (b) a vortex dynamics (Fangohr *et al.*, 2000, 2001) meshing technique. Both methods are based on Molecular Dynamics (MD) principles (Haile, 1997) which minimize the chosen system's energy functional:

> (a) In *modified bubble meshing*, the nodes of the mesh are represented by spheres of finite size, interacting only with their nearest neighbours according to Hooke's law. The variation of the node density across the domain results from making the radius of the bubbles a function of their position.

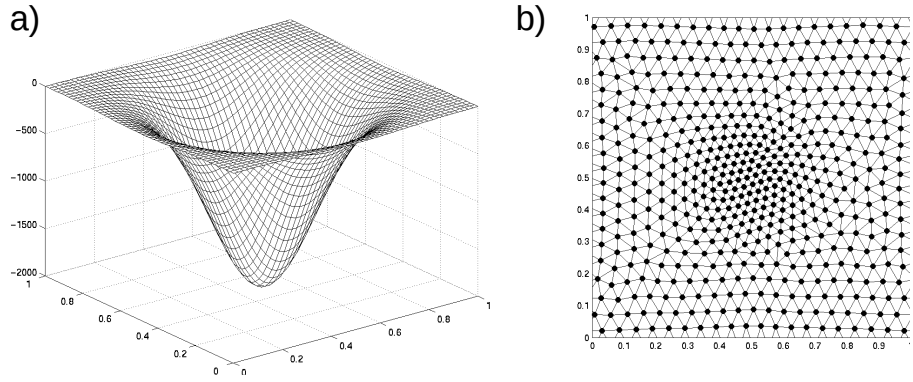

Figure 3.1: Mesh created by the Vortex meshing method.

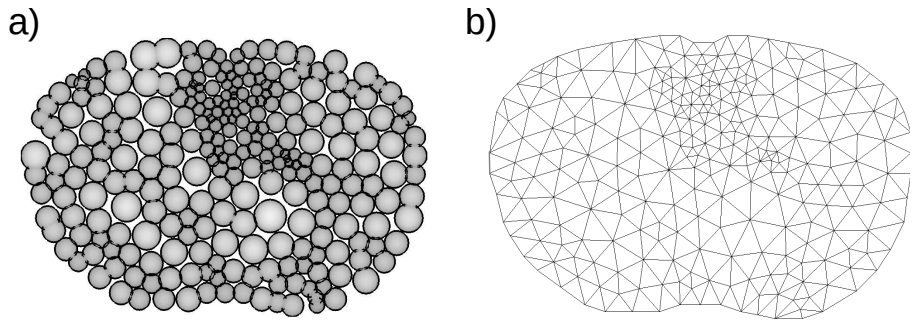

Figure 3.2: Mesh created by the Bubble meshing method.

(b) In *vortex meshing*, repulsive forces govern the equations of motion of the point-like vortices which have no spatial extension. An additional potential distribution enforces the density variation of nodes in the mesh.

The theoretical ground state (i.e. the lowest energy configuration) of both methods in the absence of density variations is, in two dimensions, a hexagonal lattice and, more generally, the closest sphere packing configuration (Aste and Weaire, 2000). For bubble meshing, this configuration corresponds to the lattice of atoms in solid state matter, whereas for vortex meshing it relates to the (two-dimensional) Abrikosov state (for a review see Blatter *et al.*, 1994) in Type-II Superconductors.

The mesh shown in figure 3.1 shows a Delaunay triangulation of a set of node positions generated by the vortex meshing technique using periodic boundary conditions. The node density in the mesh is determined by a 'pinning' potential as shown in figure 3.1(a). Vortices are attracted from the pinning potential (it reduces

Method	Density	Quality	Remeshing	Time
Advancing front	adaptive	good	N	fast
Bubble Meshing	adaptive	high	Y	fast-moderate
Vortex Dynamics	adaptive	very high	Y	moderate
Mesh conforming refinement	depends on previous mesh	depends on previous mesh	Y	very fast

Table 3.1: Properties of different finite element mesh creation techniques.

their energy) and thus vortices accumulate in the centre of the domain. Figure 3.2 shows a corresponding result from the bubble meshing technique.

Meshing algorithms usually employ the Delaunay triangulation method for which fast and hence efficient algorithms exist, for example the *qhull* package (Barber *et al.*, 1996). Table 3.1 gives an overview of some meshing methods and their performance benefits.

3.1.2 Element geometry

Although many different shapes of finite elements can be used to discretize a given domain, the most commonly used shapes are the trianglular or quadrilateral element in 2D and the tetrahedral or hexahedral element in 3D. We will be using the triangle and tetrahedron respectively as these are the simplest geometric constructs defining a plane by 3 points and a volume by 4 points, assuming points are not co-linear/co-planar.

The boundary of these elements consists of straight edges. There also exist - so-called isoparametric - elements with their surface defined by NURBS (Non-uniform rational bilinear spline) functions. These are rather difficult to handle numerically and computations involving these require large resources so that for fast and efficient computation, we will avoid their usage. In particular, there exists no analytical formula for integrating the form functions/solution along the boundaries compared to the simpler straight-edged elements (see Appendix A).

3.1.3 Element & mesh quality

Whilst for applications such as viscous fluid flow simulations elements with high aspect ratios may be desirable, general problems with lower variations in flux, such as

for example EIT, require elements with more regular shape. In 2D, the use of equilateral triangles and in 3D the use of regular tetrahedrons allows the discretization of a domain without preferring any particular direction. This property is known as *geometric isotropy* (Burnett, 1987) and ensures that one variable is not represented more accurately than the others.

A limited set of possible measures for the quality of elements, which are equally applicable to 2D and 3D, is given here:

$$q_{gm} = \frac{\text{true volume}}{\text{ideal volume}} + \frac{\text{true surface}}{\text{ideal surface}} + 1 \qquad 1 \leq q_{gm} \leq 3 \tag{3.1}$$

$$q_{rr} = \left(\frac{9\pi}{2\sqrt{3}} \frac{\text{true volume}}{\text{sphere volume}} \right)^{1/3} \qquad 0 \leq q_{rr} \leq 1 \tag{3.2}$$

$$q = D\frac{R_i}{R_o} \qquad 0 \leq q \leq 1. \tag{3.3}$$

q_{gm} and q_{rr} are presented and discussed in Robert *et al.* (1998) in the context of optimising tetrahedral space station arrangements. The higher the value, the better the quality of the element. The ideal volume and surface area are those obtained from a regular tetrahedron whose four angles, four faces and six edges are of the same shape and size, respectively. The true volume and true surface refer to the sizes obtained from the real (distorted) element whose quality is measured. In equation 3.2, the sphere volume is that of the circumscribing sphere which intersects the (real) tetrahedron at all vertices.

In general, it can be said that the mesh quality depends on the solution on the domain and elements with high aspect ratios might be suitable for solutions with highly unisotropic gradients. As we do not know the solution in advance in EIT, the general approach of using equilateral elements seems to be most promising. As the solution is assumed to be smooth, "smooth" transitions of element sizes seem to be a reasonable approximation. These are obtained by using these near-equilateral elements with high quality according to above quality measures.

In the following chapters, we will employ the quality measure q of equation 3.3 presented by Golias and Dutton (1997). R_i and R_o denote the radius of inscribed

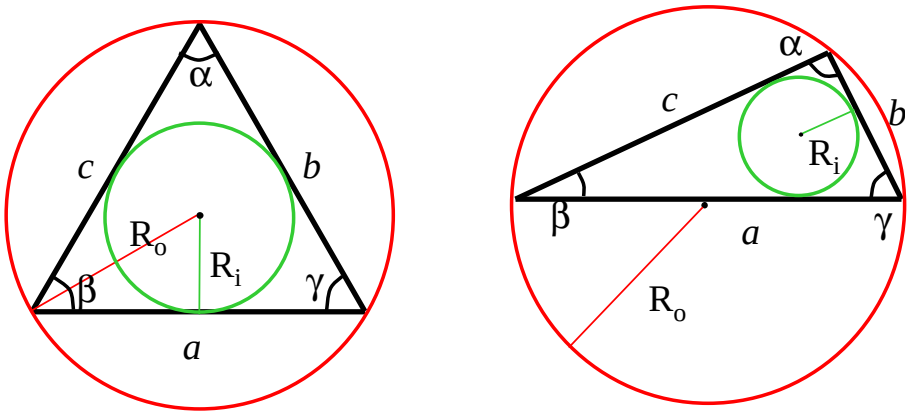

Figure 3.3: Example of calculation of element quality from inscribed and circumscribed circle.

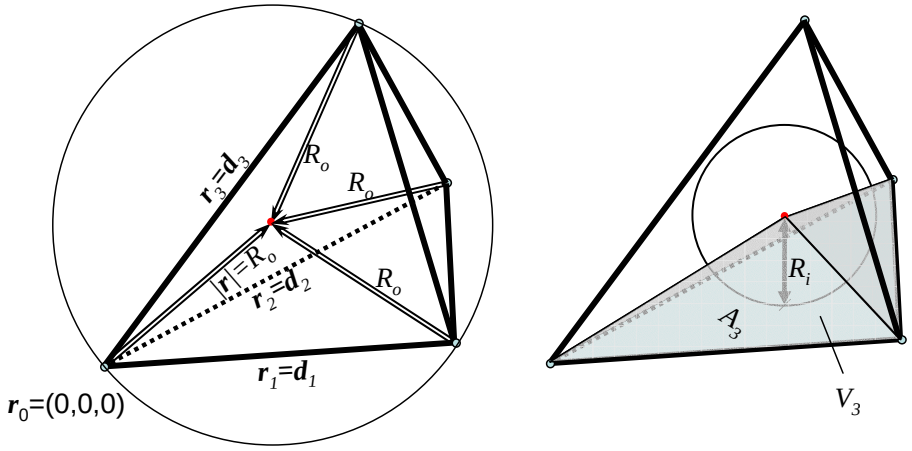

Figure 3.4: Derivation of tetrahedral element quality by computation of radii of inscribed and circumscribed spheres.

and circumscribed circle/sphere respectively and D is the dimension of the problem. Figure 3.5(b) shows a typical quality distribution of q on the 3D mesh in figure 3.5(a). From the bar graph distribution, we can visually determine how good the overall mesh quality is. As measure for the mesh quality, we will use the mean value of the q-distribution and its standard deviation.

As an example, we will derive the quality measure of a single tetrahedral element (figure 3.4):

To find the circumscribed sphere, we need the point that is equidistant from all four vertices, defined by the position vectors $\mathbf{r}_0, \ldots, \mathbf{r}_3$ with respect to the origin;

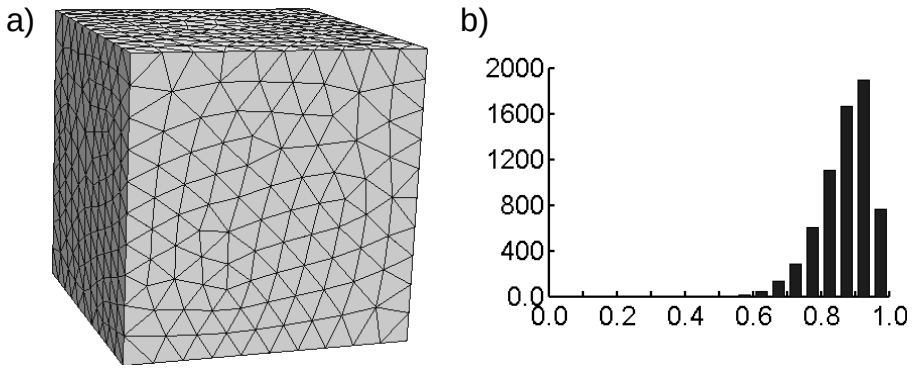

Figure 3.5: (a) High quality 3D finite element mesh consisting of 6535 tetrahedral elements, (b) quality plot of the elements contained in the cube ($<q> = 0.89$).

i.e. we want to find the centre of the sphere, $\mathbf{r}$, such that

$$\begin{aligned} (\mathbf{r} - \mathbf{r}_n) \cdot (\mathbf{r} - \mathbf{r}_n) &= R^2 \quad ; \quad n = 0 \ldots 3 \\ r^2 - 2\mathbf{r} \cdot \mathbf{r}_n + r_n^2 &= R^2. \end{aligned}$$

If we move r_0 into the origin, i.e. using the $\mathbf{d}_n$ in place of the $\mathbf{r}_n$, then $r^2 = R^2$ (sphere radius) and the equations reduce to

$$2\mathbf{r} \cdot \mathbf{d}_n = d_n^2 \quad ; \quad n = 1..3$$

This yields the matrix equation for the center of the sphere,

$$2 \begin{pmatrix} d_{1x} & d_{1y} & d_{1z} \\ d_{2x} & d_{2y} & d_{2z} \\ d_{3x} & d_{3y} & d_{3z} \end{pmatrix} \begin{pmatrix} r_x \\ r_y \\ r_z \end{pmatrix} = \begin{pmatrix} d_1^2 \\ d_2^2 \\ d_3^2 \end{pmatrix}, \tag{3.4}$$

from which we obtain for the radius R_o of the circumscribed sphere:

$$R_o^2 = r_x^2 + r_y^2 + r_z^2$$

We derive the radius R_i of the innerscribed sphere/circle by subdivision of the element with a new point placed in the centre and by connecting this centre point

to the vertices of the element. Then the volume V_j of the subdivision j is calculated from its surface area A_j and the radius R_i which represents the height of the tetraeder/triangle j in D dimensions:

$$V_j = \frac{A_j R_i}{D} \tag{3.5}$$

The total volume then corresponds to

$$V = \frac{R_i}{D} \sum_j A_j = \frac{R_i A}{D}, \tag{3.6}$$

which leads to

$$R_i = D\frac{V}{A}. \tag{3.7}$$

A_j represents the area of face j in 3D or the length of edge j in 2D respectively. In 3D, the total volume is obtained as

$$A = \sum_{faces} A_j = \frac{1}{2}\|d_1 \times d_2\| + \frac{1}{2}\|d_1 \times d_3\| + \frac{1}{2}\|d_2 \times d_3\| + \frac{1}{2}\|(d_2 - d_1) \times (d_3 - d_2)\|. \tag{3.8}$$

An alternative method for computing the quality indicator for 2D triangles can be derived with the help of Sieber and Huber (1990) as follows:

$$\begin{aligned} R_o &= \frac{s}{4\cos(\frac{\alpha}{2})\cos(\frac{\beta}{2})\cos(\frac{\gamma}{2})} \qquad \text{where} \quad s = \frac{a+b+c}{2} \\ R_i &= 4R_o \sin\left(\frac{\alpha}{2}\right)\sin\left(\frac{\beta}{2}\right)\sin\left(\frac{\gamma}{2}\right) \\ q_{\text{tri}} &= 2\frac{R_i}{R_o} = 8\sin\left(\frac{\alpha}{2}\right)\sin\left(\frac{\beta}{2}\right)\sin\left(\frac{\gamma}{2}\right), \end{aligned}$$

With $\sin(\frac{\alpha}{2}) = \sqrt{\frac{(s-b)(s-c)}{bc}}$ (Sieber and Huber, 1990) follows

$$q_{\text{tri}} = \sqrt{\frac{(s-b)(s-c)}{bc}}\sqrt{\frac{(s-a)(s-c)}{ac}}\sqrt{\frac{(s-a)(s-b)}{ab}} \tag{3.9}$$

$$= \frac{(s-a)(s-b)(s-c)}{abc}. \tag{3.10}$$

With these formula, we can easily compute a quality indicator of single elements and of a whole mesh, which we make use of in some of the examples in following chapters.

3.1.4 Element size & density

Mesh refinement. We will see in the following chapter that adaptive mesh refinement is a highly applicable technique for 2D Electrical Impedance Tomography. An initial coarse mesh can be refined to improve the accuracy of the solution as well as the resolution of material boundaries. The local refinement is then based on error or material gradient indicators, which guide the refinement process in regions of interest or where the solution varies rapidly. This saves a large amount of computation time for obtaining results of same accuracy compared to globally fine meshes.

Three major methods of mesh refinement are presented in literature. These include *h-refinement*, *p-refinement* and *r-refinement*; we will discuss further details of these methods in section 4.2.

Often, techniques for mesh creation or refinement, such as 'edge swapping' and 'element conforming subdivision' are much simpler to implement for two dimensions than for three dimensions. For 3D problems, other methods, such as those presented above have to be devised. We mainly concentrate on h-refinement of linear elements, which is both computationally efficient and adds a relatively small number of nodes and elements to the existing mesh.

3.1.5 Error Estimation

Since the true solution for the problem is unknown (otherwise we would not have to compute it numerically), the error of the approximation on the discretization is

unknown. However, once an approximated solution of the potentials at the nodes of our mesh is obtained, we can calculate a so-called *a posteriori* error estimate on an element and the mesh (Salazar-Palma *et al.*, 1998; Bathe, 1982). In Electrical Impedance Tomography, the solution of the forward problem gives us the potential at the nodes of our mesh with linear interpolation. The normal component of the current density within each element has to be continuous across inter-element boundaries. The approximate solution obtained from the FE discretization usually violates this (smoothness) condition. We can estimate the square norm of the error of the forward solution on element e, $\varepsilon^2(e)$, by summing the jumps of the squared residuals of the current density normal components ($\sigma\nabla\varphi$) across the surfaces between element e and its fth neighbour ($f = 1 \ldots N_{nb}$), given by the outward normal vector $\mathbf{s}_{ef}$.

$$\varepsilon^2(e) = g \sum_{f=1}^{N_{nb}} \left((\sigma_e \nabla\varphi_e - \sigma_f \nabla\varphi_f) \cdot \mathbf{s}_{ef} \right)^2 , \tag{3.11}$$

g is a geometrical factor, taking into account the element's shape. To obtain the total error on the mesh, we sum up the contributions of each element and take its norm

$$\varepsilon_{tot} = \sqrt{\sum_{elements} \varepsilon^2(e)}. \tag{3.12}$$

This error estimate is physically sound and robust (Salazar-Palma *et al.*, 1998) and can be carried out quite quickly. Again, for higher order elements, more terms have to be taken into account and integrals across the element's surface and in its interior have to be determined, which can slow down the computation significantly.

Applying this error estimate to an object with surface electrodes attached, we observe that the largest error is located in regions with highest current density, which is around the electrodes. This error in boundary regions around the electrodes affects the solution in inner regions of the domain significantly so that refinement is desirable as discussed previously.

Another possibility for mesh refinement is based not on the error but on the gradient of conductivity between neighbouring elements. This results in higher

resolution of material boundaries, which allows for better image resolution in ET (as we will see in the following chapter). The material gradient estimator used in the inverse problem, η is computed using the distance d_{ef} centres of mass of the element e and its neighbour f, and their respective conductivities, σ_e and σ_f:

$$\eta(e) = \sum_{f=1}^{N_{nb}} \frac{|\sigma_e - \sigma_f|}{d_{ef}}. \tag{3.13}$$

3.1.6 Mesh Templating & Deformation

In medical applications such as functional brain imaging, there arises the need for meshes which have certain built in features, for example a local high mesh density around the optic nerve or pre-defined materials in local regions. For this purpose, mesh templates can be defined which consist of a mesh corresponding to an 'average' model of the domain, for example the head. Methods are required to easily modify/deform this pre-defined template mesh to fit individual patients' geometries and/or internal material structures. Powerful tools exist for this type of reshaping (for example IDEAS), however, it would be useful to have Electrical Tomography software packages which incorporate such tools.

Our meshing methods allow for the reshaping of existing meshes by changing the bubble size in bubble meshing or the potential in the vortex dynamics based technique. Hence no new mesh needs to be computed and optimized topologies of mesh templates can be re-applied to many geometrically equivalent shapes.

3.1.7 Laplace mesh smoothing

To improve the shape and thus the quality of elements in a mesh, a smoothing operation can be carried out on an existing mesh obtained from a meshing package. Laplace smoothing is a common technique to perform this task by moving a vertex in the mesh in the centre of mass of its neighbored vertices, see figure 3.6 and figure 3.7 for a mesh (with edges represented by springs).

The difficulty with this is the definition of the term 'nearest neighbours'. However, if a Delaunay triangulation is carried out, then the vertices are connected with their nearest neighbours in the Delaunay sense (Thompson *et al.*, 1999) via the topological definitions (edges). Surprisingly, this then reduces the problem to

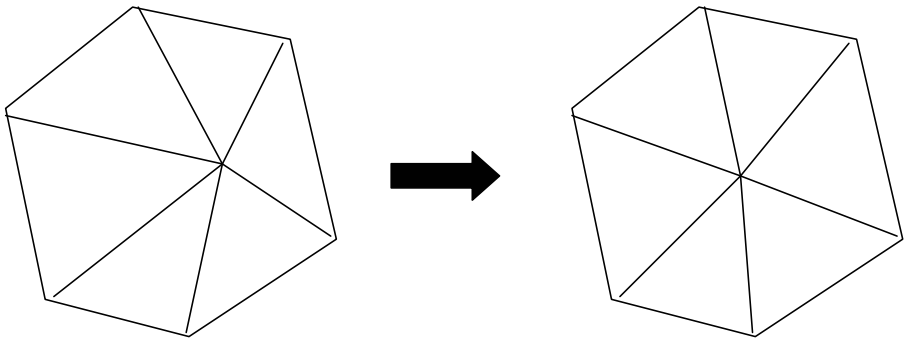

Figure 3.6: Laplace Smoothing technique: The vertex is moved into the centre of mass of its neighbours.

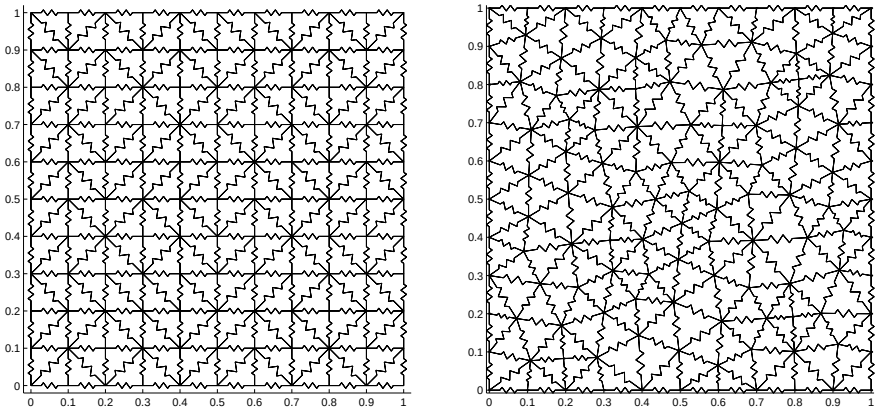

Figure 3.7: Smoothing of a mesh by the Laplace Smoothing technique: The mesh quality is visibly improved (edges between vertices are represented as springs).

the solution of a linear system of equations, and not – as is often assumed – a system of non-linear type as we will show in the following paragraph:

Assume a set of N_v given vertex positions, $\mathbf{P} \in \mathbb{R}^{N_v \times d}$, with dimension d, some of them ($\mathbf{P}_\mathrm{f} \subset \mathbf{P}$) with fixed positions (e.g. on the boundary) and all the others which can be moved freely ($\mathbf{P}_\mathrm{m} \in \mathbf{P} \backslash \mathbf{P}_\mathrm{f}$). From the Delaunay triangulation, we can easily obtain a very sparse vertex connection matrix, C, with $C_{ij} = 1$ when vertex i and j are connected by an edge and $C_{ij} = 0$ otherwise. The diagonal of C always is 0 as there is no edge between a vertex and itself. The number of vertices connected to a specific vertex k can then easily be found by summing up the entries in the connection matrix in row (or column) k: $n_k = \sum_i (C_{ik}) = \sum_j (C_{kj})$.

We obtain a linear system of equations which determines the new positions of the movable vertices, $P_{\mathrm{m,new}}$ (the others stay fixed):

$$\begin{bmatrix} C_F \\ C_M \end{bmatrix} \begin{bmatrix} \mathbf{P}_\mathrm{f} \\ \mathbf{P}_\mathrm{m} \end{bmatrix} = \mathrm{diag}(n) \begin{bmatrix} \mathbf{P}_\mathrm{f} \\ \mathbf{P}_\mathrm{m,new} \end{bmatrix} \tag{3.14}$$

To obtain solely the new positions of the movable vertices, we have to solve for $P_\mathrm{m,new}$:

$$\mathbf{P}_\mathrm{m,new} = diag(1/\mathbf{n})\ C_M \begin{bmatrix} \mathbf{P}_\mathrm{f} \\ \mathbf{P}_\mathrm{m} \end{bmatrix}. \tag{3.15}$$

The implementation in Matlab is straightforward and results in a very fast and efficient smoothing operation without the need for iterations.If we start with a high quality mesh, the resulting mesh is very likely to satisfy the Delaunay criterion. This, however, cannot be guaranteed and retriangulating according to the Delaunay criterion might be advisable to obtain a Delaunay-conform topology.

3.1.8 Node numbering

The numbering of the vertices in a finite element mesh can affect the solution speed of the numerical algorithm used to perform an inversion of a matrix. As we will see later, the matrices involved in the solution process are of size $N_V \times N_V$ with N_V being the number of vertices. Entries in this matrix only exist where two vertices i and j are connected via an edge and hence it is very sparse.

The Cholesky decomposition of a positive definite matrix and subsequent re-substitution can be performed faster and with less memory requirements if the vertices are numbered in such a way that the Cholesky factor of the matrix is also sparse. This is possible using, for example, the so-called *symmetric minimum degree algorithm*, "symmmd" (Press *et al.*, 1997; Golub and vanLoan, 1989). This and other methods for the use specifically in EIT have been investigated by Fulton and Lipczynski (1995).

Figure 3.8 shows the permutation in the entries of the system matrix of a simple system of size 267 ×267 and the number of nonzero entries in the matrix.

The time needed to Cholesky-decompose the matrices for a solution of the forward problem is 14.8 ms for the unaltered matrix and 3.2 ms for the permuted matrix plus 2.2 ms for the symmmd algorithm – this is a factor of approximately

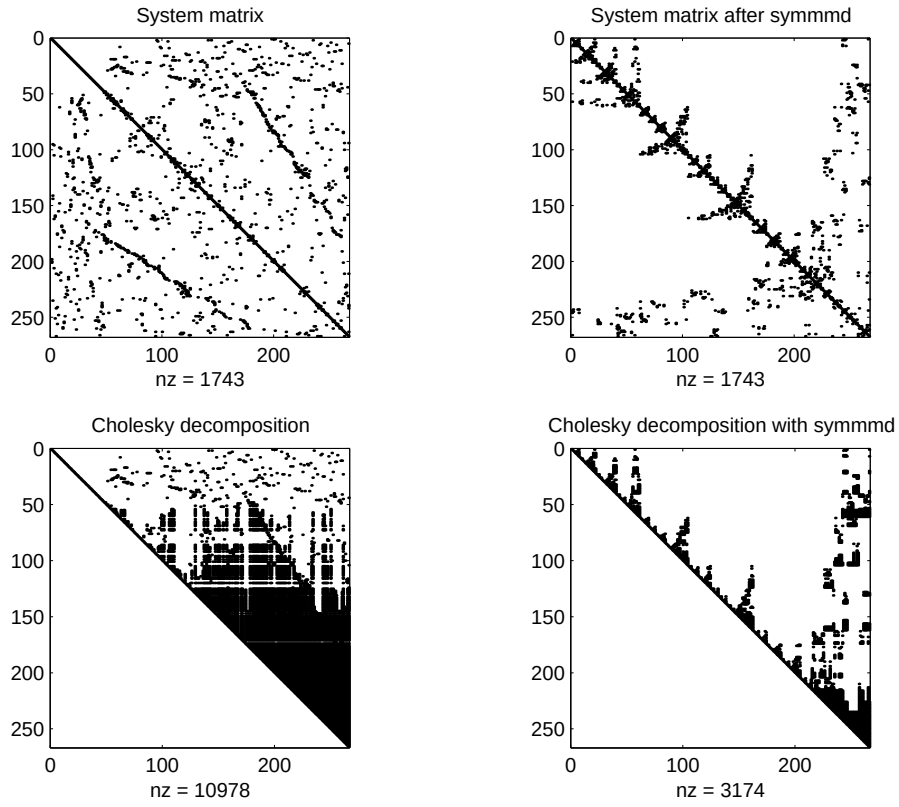

Figure 3.8: Results of permutation of the vertex numbers by the "Symmetric Minimum Degree" technique. Upper row: system matrix before (left) and after (right) minimum degree permutation. Bottom row: Cholesky decomposition of above matrices.

2.74 faster. The respective back-substitution times are 30.7 ms and 6.1 ms – this is another factor of approximately 5 faster for the permuted matrix. Altogether, we compare (14.8 ms+30.7 ms =) 45.5 ms to (3.2 ms+2.2 ms+6.1 ms =) 11.5 ms, this corresponds to a speed-up factor of 3.96 for a relatively small problem!

These results were obtained on a 700MHz Pentium PC in Matlab Version 5.3.

In the case of complex matrices, which occur when in addition to the conductivity also the permittivity is sought, Cholesky decomposition cannot be used as the system matrix will not be positive definite any more. The alternative solution for this case is to use the LU decomposition method, with the same aim to keep the L and U matrices as sparse as possible to maintain the highest possible efficiency.

3.2 Results

We show Electrical Impedance Tomography reconstructions of the same configuration on different types of 2D Finite Element meshes. All meshes are based on

# Nodes	# Elements	Quality Q	Error E	Time (ms)
17	16	0.63	0.40	10
27	36	0.92	0.24	10
43	68	0.96	0.21	14
56	91	0.95	0.19	20
77	121	0.93	0.17	30
136	233	0.95	0.14	50
267	472	0.94	0.12	100
511	947	0.96	0.09	230
823	1542	0.95	0.07	441
2447	4727	0.96	0.01	3560
6047	11890	0.96	(0.00)	$\sim$19 sec

Table 3.2: Different timings for meshes with linear interpolation functions on which the forward problem in EIT was computed, see text for definition of terms.

first order linear interpolation functions with constant conductivity values across the elements. The quality of the mesh can be given as a bargraph or - as we applied it - as a mean value of the distribution and its standard deviation. Table 3.2 gives a quantitative overview of the different meshes used and figure 3.9 indicates that the relation between number of nodes/elements and the time for solving the linear system is of exponential nature.

Q is calculated as the mean of $q_e = 2R_i(e)/R_o(e)$. The error E indicates the normalised difference between computed and measured voltages $\mathbf{U}$ and $\mathbf{V}$ at the electrodes, $E = ||\mathbf{U} - \mathbf{V}||/||\mathbf{V}||$. The time given was spent on computing not only the solution but also on memory allocation and assembly of the system matrix, computation of the matrices relevant for the complete electrode model (CEM), assembly of the CEM system matrix and finally the solution of the linearized matrix system. The time was taken on a PC with 512 MB main memory and a 900 MHz with MATLAB 5.3 for the calculations. To obtain an accurate estimate of the 'true' solution we computed the voltages at the electrodes $\mathbf{U}$ using the mesh with 11 890 elements (as shown in figure 3.10) and used these in the calculation of E.

We can see that the element density is the most critical component in terms of accuracy. In figure 3.11, we present the variation in the potential distribution for

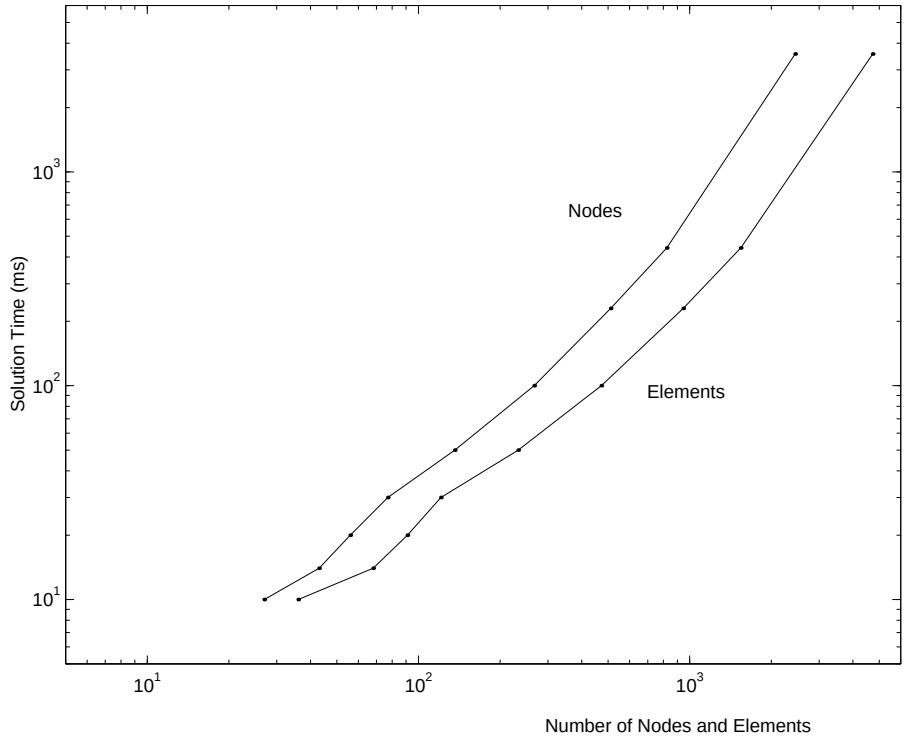

Figure 3.9: Time spent on solution of the forward problem with respect to the number of elements / nodes in the mesh. Numbers correspond to those given in table 3.2.

an identical current injection in all cases, coming in just before the three o'clock position through the electrode indicated by the bar around the boundary and coming out at the opposite electrode, positioned at just before nine o'clock.

By making the mesh denser (and application of Laplace mesh smoothing to improve the quality of mesh elements), we find that forward solution and resolution improve by a factor of approximately 2 for employing ten times as many elements/nodes resulting in apprximately a ten-fold increase in computation time.

Table 3.3 contains the refinement steps carried out on the initially very coarse and unsuitable mesh with 17 nodes and 16 elements. Figure 3.12 shows the improvement of accuracy in the forward solution by using adaptive, error-estimator based refinement. Comparing the time (71 ms) and error (0.110) to the values given above, we achieved a result equivalent to the use of a mesh of size 267 nodes or 472 elements respectively.

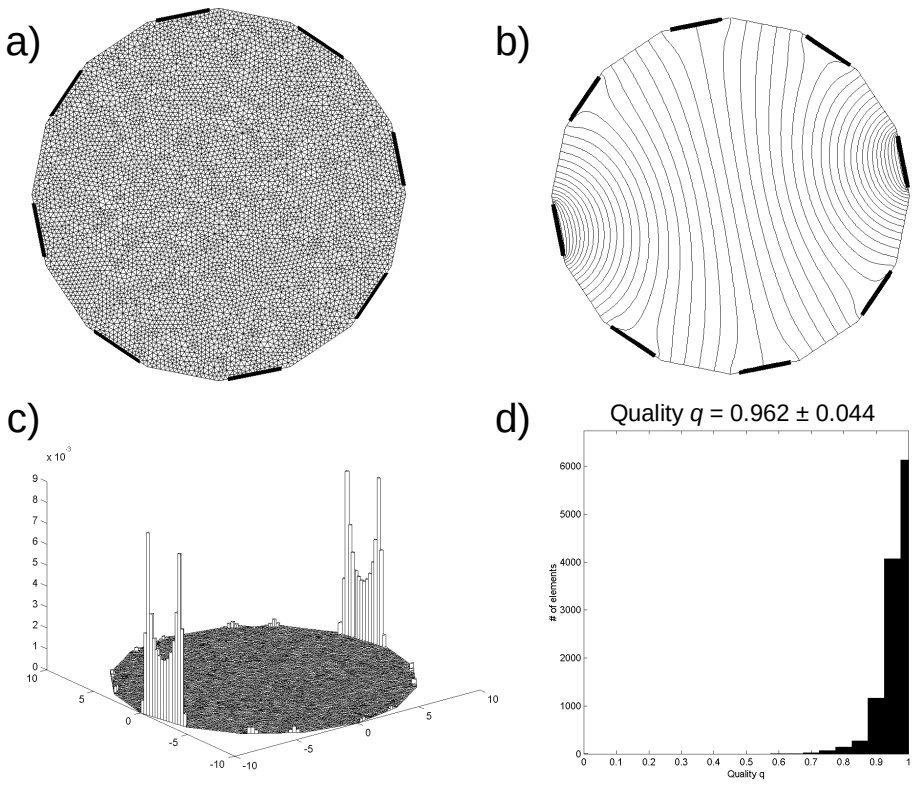

Figure 3.10: (a) The finite element mesh consisting of 6,047 nodes and 11,890 elements used for the most accurate computation of the potential shown in (b). The error estimator indicates that the error of the solution is large at the edges of the electrodes, especially of the two current injection electrodes (c). Graph (d) shows the very high geometrical quality of the elements in the mesh as defined in equation (3.3).

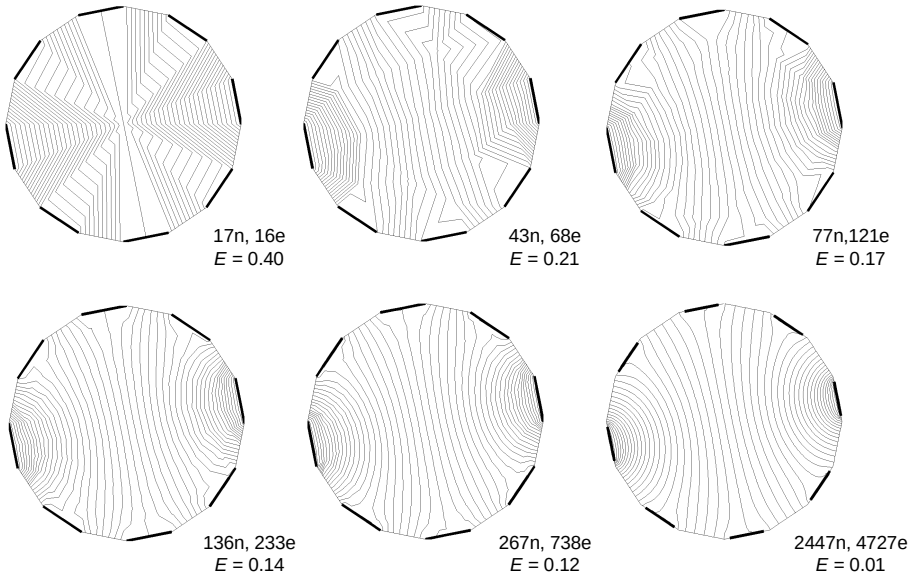

Figure 3.11: Potential distribution for differing finite element meshes. The numbers next to the meshes indicate the number of nodes and elements used. E denotes the error of the solution on the mesh.

	# Nodes	# Elements	Error E	Time (ms)
Starting state	17	16	0.400	11
Refinement 1	31	38	0.235	20
Refinement 2	47	64	0.191	20
Refinement 3	69	100	0.110	20
Result:	69	100	0.110	71
Global refinement	267	472	0.12	100

Table 3.3: Auto-adaptive refinement decreases the error on the solution using less nodes / elements than the global refinement and achieves a comparable error in even less time!

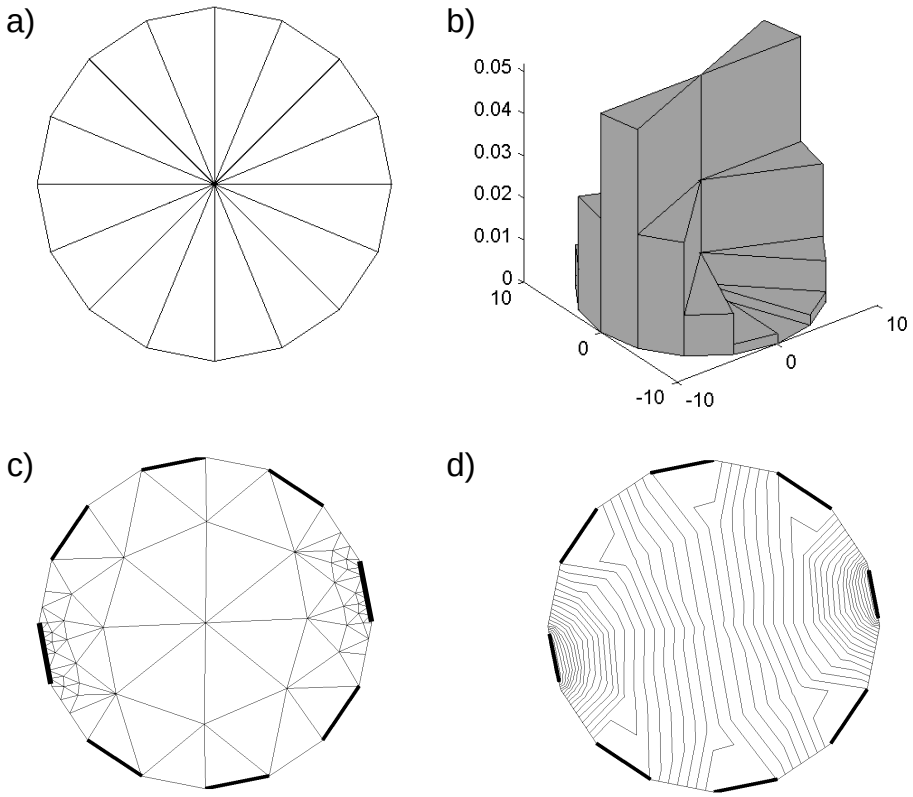

Figure 3.12: (a) shows an unsuitable mesh for reconstruction which we will refine according to the error estimator on the elements shown in (b). After three auto-adaptive refinement and smoothing steps, we obtain the mesh in (c) which results in the potential dicstribution in (d). This adaptive meshing is much faster and produces more accurate results than global fine meshes (see table 3.3)

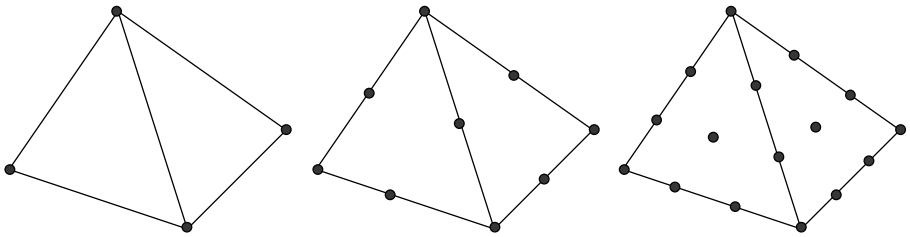

Figure 3.13: Node distribution on elements with first, 2^{nd} and 3^{rd} order interpolation

3.3 Approximation of potential

Once the FE discretization $\mathcal{D}$ of the domain Ω is obtained, the potential $\phi(\mathbf{r})$ within an element $\mathbf{r} \in \Omega^{(e)}$ can be approximated as

$$\phi(\mathbf{r}) \approx \varphi(\mathbf{r}) = \sum_{i=1}^{N_N} \alpha_i(\mathbf{r})\varphi_i, \tag{3.16}$$

where the $\alpha_i(\mathbf{r})$ are known as basis, interpolation or form functions and the φ_i represent the potential at node i within the element. N_N denotes the total number of nodes.

3.3.1 Choice of interpolation function

A commonly made choice for the interpolation function $\alpha_i(\mathbf{r})$ are Lagrange polynomials of grade p, and we define the first order interpolation in two dimensions as $\alpha_i^{(1)}(\mathbf{r}) := \alpha_i(\mathbf{r}) = c_1 + c_2 x + c_3 y$. The coefficients c_j are determined by the geometry of the element, and the number of coefficients necessary for a polynomial of order p increases as $(p+1)(p+2)/2$ for 2D and as $(p+1)(p+2)(p+3)/6$ for 3D.

In the case of linear interpolation, the nodes on the element correspond to the vertices which define the element. Higher order interpolation leads to additional nodes on the faces of the elements and above second order interpolation, there will be nodes within the elements. Figure 3.13 shows how the nodes will be distributed across the elements.

The approximation space associated with all elements having polynomial interpolation functions belongs to the space of continuous functions, C^0. Extending the formulation to approximation spaces that have continuous first derivatives across

element edges is surprisingly difficult. The simplest C^1 element in 2D is the 21 noded triangle with 5^{th}-order interpolation function.

Higher order polynomials as base functions provide better approximations, however, at the cost of increased computational complexity and resources. Generowicz *et al.* (2002) investigated the impact of higher order interpolation functions on the computational cost of solving a generalised eigenvalue problem for photonic bandgap modelling. The results of this comparison of first to sixth order polynomials show that second order basis functions perform best in terms of computation time compared to achievable accuracy.

Not only the the order of the basis functions but also their shape plays an important role in the accurate representation of the solution on the mesh. The shape functions tend to be standard polynomials or - depending on the symmetry of the domain - can be Bessel or Legendre functions or any other type of C^0 functions. It is desirable to use a problem-adapted base function which simplifies the numerical approximation and provides a high level of accuracy. The most suitable shape functions for arbitrary geometries are Lagrange interpolation polynomials. They provide interpolation up to any desired polynomial order. We note that with increasing order (so-called p-refinement), the number of interpolation nodes required for a given mesh increases and the subsequent higher computational cost leads to an increase in computation time.

We can see from the work of Vauhkonen *et al.* (1999) that for achieving a better accuracy of a factor 2 to 5, the number of interpolation nodes in the p-refinement case increases by a factor of 7, which leads to a slow-down of at least a factor 10 in the reconstruction.

We have decided to employ simple piecewise linear shape functions which are both fast to compute and easy to maintain in programming structures. The computing time saved in this way is then spent on refining the mesh locally rather than on global higher-order functions.

3.4 Determination of system matrix

To obtain the numerical solution to the general continuous equation

$$-\nabla\sigma(\mathbf{r})\nabla\phi(\mathbf{r}) + \beta(\mathbf{r})\phi(\mathbf{r}) = f(\mathbf{r}), \tag{3.17}$$

an approximation is required on the discretization $\mathcal{D}$. The most commonly used technique is the Rayleigh-Ritz-Galerkin variational method (Schwab, 1998) where the interpolation functions α_i are used as weighting functions for the residual R of the approximated solution:

$$R(\mathbf{r};\varphi) = -\nabla\sigma(\mathbf{r})\nabla\phi(\mathbf{r}) + \beta(\mathbf{r})\phi(\mathbf{r}) - f(\mathbf{r}). \tag{3.18}$$

The variational integral of the α_i-weighted residual then yields

$$\int \alpha_i \left\{-\nabla\sigma\nabla\phi + \beta\phi - f\right\} \,\mathrm{dV} = 0 \qquad i = 1, 2, \ldots, N_N. \tag{3.19}$$

Integration by parts and application of the Gaussian integration formula leads to

$$\int \left\{\sigma\nabla\alpha_i \cdot \nabla\phi + \alpha_i\beta\phi\right\} \,\mathrm{dV} = \int \alpha_i f \,\mathrm{dV} - \oint \alpha_i j_n \,\mathrm{dS}, \tag{3.20}$$

where the first term on the right hand side represents internal current sources and the second represents the boundary influx of the normal current density j_n through the surface of the object.

Approximating ϕ with the trial solution φ from equation (3.16), we obtain

$$\sum_{j=1}^{N_N} \left\{ \int \sigma\nabla\alpha_i \cdot \nabla\alpha_j \,\mathrm{dV} + \int \beta\alpha_i\alpha_j \,\mathrm{dV} \right\} \varphi_j = \int \alpha_i f \,\mathrm{dV} - \oint \alpha_i j_n \,\mathrm{dS}. \tag{3.21}$$

We define the *Dirichlet* or stiffness matrix (D), the *Metric* or mass matrix (M), the internal source or *load vector* ($\boldsymbol{\varrho}^{\text{int}}$) and the external source/load vector ($\boldsymbol{\varrho}^{\text{ext}}$) as

$$D_{ij} = \int \sigma \nabla \alpha_i \cdot \nabla \alpha_j \, \mathrm{dV} \tag{3.22}$$

$$M_{ij} = \int \beta \alpha_i \alpha_j \, \mathrm{dV} \tag{3.23}$$

$$\varrho_i^{\text{int}} = \int \alpha_i f \, \mathrm{dV} \tag{3.24}$$

$$\varrho_i^{\text{ext}} = \oint \alpha_i j_{-n} \, \mathrm{dS}. \tag{3.25}$$

Equation (3.21) can then be rewritten as a linear matrix equation:

$$K\boldsymbol{\varphi} = \boldsymbol{\varrho}, \tag{3.26}$$

where $K = D + M$ denotes the *system matrix* of size $N_N \times N_N$, relating the nodal potentials in $\boldsymbol{\varphi}$ to the electric field sources in $\boldsymbol{\varrho}$. It is very sparse as entries at positions K_{ij} exist only when nodes i and j are on the same edge of an element. The system matrix is often described as the *stiffness matrix* (in mechanical engineering) or as the *admittance matrix* (in electrical engineering).

In EIT it is indeed a discrete approximation to the transfer admittance operator $\mathcal{Y} = \mathcal{R}^{-1}$, resembling closely the structure of a resistor network. Therefore, we will refer to the system matrix as the admittance matrix henceforth and call its inverse – the discrete approximation of the transfer resistance operator $\mathcal{R}$ – the *resistance matrix*. Both are symmetric and positive definite if the conductivity complies with the physical restrictions of being positive and limited to an upper bound.

In Electrical Impedance Tomography, internal sources usually do not exist and hence $f = 0$ in equation (3.19). The vector of external sources contains the information of the Neuman BC. For the forward problem of EIT, these are represented by piecewise polynomial approximations of the current injected through boundary electrodes on the finite element mesh. The actual boundary conditions require a closer look as their formulation expands the system matrix by including the contact

impedance in the equations.

3.5 Application of boundary conditions

We have seen in chapter 2 that in addition to the formulation of the basic differential equations, boundary conditions need to be specified. The incorporation of the complete electrode model as given by equations 2.22–2.27 extends the system matrix to incorporate additional terms containing the contact impedance z. The surface integral on right hand side of equation (3.21) representing the injected current, is then replaced by the term obtained from equation (2.25):

$$\begin{aligned} \int_{S_\ell} \alpha_i \sigma \nabla \varphi_j \cdot n \, \mathrm{dS} &= \int_{S_\ell} \alpha_i \frac{V_\ell - \varphi_j}{z} \, \mathrm{dS} && (3.27) \\ &= \frac{V_\ell}{z} \int_{S_\ell} \alpha_i \, \mathrm{dS} - \frac{1}{z} \int_{S_\ell} \alpha_i \alpha_j \varphi_j \, \mathrm{dS}. && (3.28) \end{aligned}$$

The contact impedance can then be identified by $\beta = 1/z$ and hence we obtain from equation (3.21):

$$\sum_{j=1}^{N_N} \left\{ \int \sigma \nabla \alpha_i \cdot \nabla \alpha_j \, \mathrm{dV} + \frac{1}{z} \int \alpha_i \alpha_j \, \mathrm{dS} \right\} \varphi_j = \sum_{\ell=1}^{N_L} \frac{V_\ell}{z} \int_{S_\ell} \alpha_i \, \mathrm{dS}. \qquad (3.29)$$

This leads in the numerical representation of an extended system matrix as follows

$$S = \begin{pmatrix} K & C \\ C^T & G \end{pmatrix} \begin{pmatrix} \boldsymbol{\varphi} \\ \mathbf{V} \end{pmatrix} = \begin{pmatrix} \mathbf{0} \\ \mathbf{I} \end{pmatrix}, \qquad (3.30)$$

where

$$\begin{aligned} K_{ij} &= \int_\Omega \sigma \nabla \alpha_i \nabla \alpha_j \, \mathrm{dV} + \frac{1}{z} \sum_{\ell=1}^{N_L} \int_{S_\ell} \alpha_i \alpha_j \, \mathrm{dS} \qquad \text{for } i,j = 1,2,\ldots,N_N \\ C_{ij} &= -\frac{1}{z} \int_{S_\ell} \alpha_i \, \mathrm{dS} \qquad \text{for } i = 1,2,\ldots,N_N;\ j = 1,2,\ldots,N_L \qquad (3.31) \\ G_{ij} &= \frac{1}{z} \sum_k \int_{S_\ell} \alpha_k \, \mathrm{dS} \qquad \text{for } i,j = 1,2,\ldots,N_L. \end{aligned}$$

To obtain the measured voltages $\mathbf{V}$ from this matrix equation, only a part of the inverse of S of size $N_N \times N_L$ is required which relates the nodal voltage values to the electrode potentials. The solution of the above system can be achieved quickly by Cholesky decomposition and backsubstitution (Press *et al.*, 1997). Extending the lower right hand side vector by a unit matrix, the required inverse part of S can be obtained in the same Cholesky process and hence no additional inversion is required.

3.6 Convergence of the finite element method

The ultimate goal of the forward problem in EIT is to predict the potential distribution within the object of known conductivity and to obtain the resulting voltages at the measurement electrodes. The accuracy required from the voltages is predetermined by the measurement accuracy and has to be met by the model. For iterative reconstruction algorithms, the modelling must be both accurate and fast. The accuracy is limited by the characteristics of the elements, coarseness of the mesh and accuracy of the boundary model. As there is no *a priori* way of determining the best configuration of the discretization used in the numerical approximation, we will demonstrate the theoretically achievable limit and introduce an *a posteriori* estimate of error on the solution.

The convergence of the finite element approximation, φ, to the solution ϕ of a second order elliptic partial differential equation can be expressed as stated in Paulson (1992):

$$\frac{\|\phi - \varphi\|_s}{\|\phi\|_{p+1}} \leq C h^{p+1-s}, \tag{3.32}$$

where $\|\cdot\|_s$ is the Sobolev norm of degree s and C is a constant. The radius of an element, h, corresponds to the radius of the smallest circle circumscribing the element. In a mesh composed of many elements, h represents the maximum radius of any of its elements. Hence the global absolute convergence depends on the size of the largest element in the mesh, and as $h_{max} \to 0$, the solution converges to the true solution, $\varphi \to \phi$ (Burnett, 1987). Here, p denotes the degree of the interpolation polynomial used for the approximation and in the linear case ($p = 1$), we obtain for

a zero order Sobolev norm ($s = 0$) the convergence relation

$$\frac{\|\phi - \varphi\|_0}{\|\phi\|_{1+1}} \leq Ch^{1+1-0} = Ch^2 = \mathcal{O}(h^2). \tag{3.33}$$

For the finite element solution to have uniform error across the region, the radius h and hence the element size needs to be tuned locally to the variation of the potential field. However, this is impossible as long as the solution – which depends on the conductivity distribution – is not known. We show in the next section how to derive an estimate of the solution error after a solution is obtained (a so-called *a posteriori* error estimate).

3.7 Solution of the forward problem

Having the discretization, a solution can be obtained using an approximation function. The most straightforward approach is the assumption of a linear basis function for the potential φ within an element e,

$$\varphi_n^e(x, y) = c_1 + c_2 x + c_3 y = (1, x, y) \cdot (c_1, c_2, c_3)^T, \tag{3.34}$$

where the c_i are *a priori* unknown coefficients. These can be calculated by taking into account the vertex positions of a single triangle, (x_i, y_i), and their corresponding potential values φ_i:

$$\mathbf{c} = \begin{bmatrix} 1 & x_1 & y_1 \\ 1 & x_2 & y_2 \\ 1 & x_3 & y_3 \end{bmatrix}^{-1} \begin{pmatrix} \varphi_1 \\ \varphi_2 \\ \varphi_3 \end{pmatrix}. \tag{3.35}$$

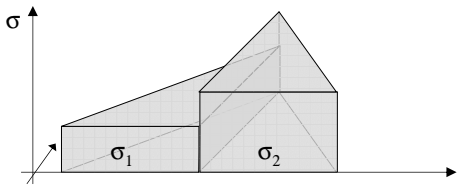

Figure 3.14: Zero-order interpolation function for conductivity σ on two elements

Thus, the element potential function can be expressed as

$$\begin{aligned} \varphi^e(x,y) &= (1,x,y)\cdot \mathbf{c}^T \\ &= (1,x,y)\cdot \begin{bmatrix} 1 & x_1 & y_1 \\ 1 & x_2 & y_2 \\ 1 & x_3 & y_3 \end{bmatrix}^{-1} \begin{pmatrix} \varphi_1 \\ \varphi_2 \\ \varphi_3 \end{pmatrix} \end{aligned} \tag{3.36}$$

$$\varphi^e(x,y) = \sum_{\nu=1}^{3} \alpha_\nu(x,y)\ \varphi_\nu. \tag{3.37}$$

The potential is formed by the nodal potentials φ_ν multiplied by the position dependent *interpolation* or *form functions* $\alpha_\nu(x,y)$, which are 'tent-like' for the linear case (i.e. they have value one at vertex ν, value zero at all other vertices and a constant slope between). An additional property of the form functions is that they add up to one, $\sum_\nu \alpha_\nu = 1$.

3.7.1 Interpolation function

As for the potential distribution in the forward problem, we need to numerically approximate the conductivity distribution for the inverse problem. Two-dimensional images usually consist of square pixels with each pixel containing a single color value. Again, we are using finite elements in the numerical reconstruction and thus, our pixels are represented by triangles. The interpolation function we choose is of uniform nature, i.e. represents a constant conductivity across a single element. Figure 3.14 shows the conductivity distribution of such an element.

3.8 Visualisation tools

The results of tomographic reconstruction are often difficult to visualise in a way that is useful for clinicians/human monitors. In particular, three-dimensional visualization is not very simple in the coding/programming sense. Commercial software such as, for example, MATLAB from The Mathworks enables full three-dimensional imaging across different Operating System platforms. MATLAB - as well as many other powerful visualisation packages (DataExplorer, GeomView, AVS, IDL, IrisExplorer to name but a few) - uses OpenGL implementations for visualisation. With OpenGL, the display of iso-surfaces, data interpolations and the application of a range of image processing algorithms can be carried out with considerable ease. Furthermore, the flexible graphical user interfaces often simplify functions such as zooming, rotating, panning, etc. OpenGL is a powerful, operating system independent graphics standard for which implementations such as GLUT (2001) or MESA (2001) are freely available. In addition, cheap graphics cards aimed at the PC games market provide highly optimized OpenGL performance, which was only possible on expensive graphics workstations a few years ago. The FE meshes used for reconstruction can also be used for visualisation. By applying clipping planes or isosurface display techniques, quantities such as potential, current density or material in the interior of a volume can efficiently be presented to the user.

3.9 Software implementation

The computational algorihms needed for a full reconstruction cycle in Electrical Impedance Tomography required the writing of a large number of routines and functions which – during the course of this project – were not available otherwise or in development.

We decided to use Matlab as development and run-time environment, as it offers very efficient matrix handling, built-in visualisation tools and optimised algorithms. Matlab is a mathematical scripting and execution environment for Linux and Windows operating systems which allows for fast prototyping.

The implementation of the algorithms for EIT reconstruction was performed in a number of steps.

Routines for loading the experiment configuration, mesh and data files had to be written.

A suite of mesh tools (termed 'SMESH') was developed to simplify the creation, loading and saving of FE meshes, the adaptation by refinement, computation of the Dirichlet system matrix, extraction of element centres, volumes and materials as well as assignment of boundary conditions and mesh smoothing. Table 3.4 gives an overview of the routines implemented for FE mesh handling.

The Newton-Raphson algorithm as well as the Conjugate gradient algorithm and the computation of the regularisation matrix were performed without using the existing Matlab toolboxes so that it was possible to profile the code and also because many of the pre-defined Matlab routines did not provide the flexibility required. The numerical routines were then optimised according to the timing profile obtained from the Matlab profiler.

A number of visualisation routines was also written which allowed the 2D and 3D visualisation of meshes, potentials, conductivity distributions and display of subset of these.

The Matlab software routines required to solve the actual forward and inverse problems in EIT on the finite element discretisation, have been assembled in a package titled *SEEIT*, which is an abbreviation for Southampton's Extended Electrical Impedance Tomography software.

Table 3.5 details the functions as part of this package and figure 3.15 shows a typical call graph, representing the interconnections between the SEEIT functions.

It should be noted that the recent large interest in such software for EIT reconstruction has led to the development of a collection of Matlab routines for 2D (Vauhkonen *et al.*, 2001) and subsequently 3D (Polydorides and Lionheart, 2002) Electrical Impedance and Diffuse Optical Reconstruction Software, also known as the EIDORS project, which has been released (http://www.eidors.org, 2002) under the GNU public license.

The software presented in this section sllows for the application of most of the optimisations as mentioned in this chapter. We are going to employ these routines of

Matlab function	Description
mesh_bubble.m	Simple bubble meshing routine. Returns mesh from polygon boundary definitions.
mesh_create.m	Creates meshes from polygon boundary definitions.
mesh_defineBC.m	Define & assign boundary conditions in graphical user interface.
mesh_density.m	Computes local element density.
mesh_dirichlet.m	Computes the Dirichlet/stiffness matrix for the FE mesh.
mesh_disp.m	Display different flavours of the mesh and the solutions on it. Allows for element/vertex/face highlighting and numbering to be displayed as well as element-based material distributions and vertex-based solutions, such as iso-lines, iso-surfaces, electrodes, etc.
mesh_disp_elems.m	Simple element graphic routines for element display.
mesh_disp_unv.m	More universal display modes.
mesh_edgecentre.m	Computes and returns vector of centre positions of edges.
mesh_edgelength.m	Computes and returns vector of edge lengths.
mesh_edges.m	Computes and returns the edges in a FE mesh in matrix format (vertex 1, vertex 2).
mesh_elemcentre.m	Computes and returns the centre of mass of all or of a range of elements in vector format.
mesh_elemdirichlet.m	Computes and returns a vector of matrices containing the Dirichlet/stiffness matrices for the elements in the FE mesh.
mesh_elemvolume.m	Computes and returns vector of element volumes (areas in 2D).
mesh_faces.m	Assembles and returns the face matrix containing the vertices and the neighbouring elements of a face in a row (v1, v2, v3, nL, nR).
mesh_facesize.m	Computes the face sizes of a range of or of all faces in the FE mesh.
mesh_load.m	Loads a range of FE mesh formats from data files.
mesh_loadAVS.m	Loads meshes in AVS format.
mesh_loadEASY.m	Loads meshes in EASYMESH format.
mesh_loadFEM.m	Loads meshes in standard FEM format.
mesh_loadGEOM.m	Loads meshes in GEOMPACK format.
mesh_loadMSH.m	Loads meshes in SMESH format (with extension .msh).

Table 3.4: Description of meshing functions written in Matlab as part of the SMESH package.

Table 3.4 continued.

Matlab function	Description
mesh_loadNETGEN.m	Loads meshes in NETGEN format.
mesh_loadQHULL.m	Loads meshes in QHULL format.
mesh_loadRAMPANT.m	Loads meshes in RAMPANT format.
mesh_loadTRIA.m	Loads meshes in TRIANGLE format.
mesh_loadcomplete.m	Loads a range of FE meshes and carries out integrity checks as well as constructs the missing entries in the mesh structure (faces, surface, etc.) before returning the Matlab mesh structure.
mesh_matgradient.m	Computes the material gradients across face boundaries between elements.
mesh_quality.m	Computes and returns a vector containing the quality factor of elements ($q = dim * r_i/r_o$).
mesh_refine.m	Performs h-refinement of FE meshes by either edge, face or centred point insertion.
mesh_save.m	Saves meshes in SMESH format (with extension .msh).
mesh_savePOS.m	Saves positions of vertices only.
mesh_saveSTURGEON.m	Saves mesh in STURGEON format.
mesh_smooth.m	Performs Laplace smoothing of mesh points and returns vector with new vertex positions.
mesh_surfacevertices.m	Extracts surface vertices from the mesh.
mesh_surffaces.m	Extracts the surface of the FE mesh.
obj_*.m	Files containing polygon definition routines for object surfaces.

the SEEIT and SMESH packages in the following chapters to compute the forward solution and solve the inverse problem with adaptive mesh refinement techniques.

Matlab function	Description
ApplyElectrodeDef.m	Applies electrode definitions (as boundary conditions) to the FE mesh and returns current pattern and voltage measurement matrices.
AssCurrPattMatrix.m	Assembles the current pattern and voltage measurement matrices from the parameters given in the project file.
ElecFindPatch.m	Finds elements and their faces underneath electrode patches.
Jacobian.m	Computes the Jacobian of the voltages with respect to the element conductivities.
LoadElectDef.m	Loads electrode definition parameters from data file (versions V1 and V2).
LoadMeasData.m	Loads real measurement data and computes noise from the variation of the measurements.
LoadProject.m	Loads project description file with parameters such as mesh files used, electrode and injection parameters, reconstruction parameters, ...
LoadSimMeasData.m	Loads simulated measurement data and adds Gaussian noise.
LogRegularisation.m	Computes and returns the regularisation matrix and/or vector in log-space.
RefineSGradient.m	Refines the mesh at conductivity gradients and adapts boundary conditions and Dirichlet matrix.
SaveSimMeasData.m	Saves simulated measurement data to file.
Solve_fwd.m	Solves the forward problem on a given FE mesh with given conductivities and boundary conditions.

Table 3.5: Description of functions used in the reconstruction of EIT images as part of the SEEIT software package.

Chapter 4

Adaptive Mesh Refinement for Forward Solution

In the previous chapter, we have reviewed the factors affecting the numerical approximation of the continuous electric potential. The finite element method allowed us to approximate the potential distribution by subdividing the object region into numerical entities, the elements. As the approximation is relatively coarse, the use of smaller elements for the discretization would improve the accuracy of the solution. However, using more elements requires higher computational resources. In this chapter, we will devise a method which balances computational requirements with achievable accuracy of the forward solution to obtain a high computational performance. We introduce adaptive mesh refinement and demonstrate how results computed using a self-adaptive refinement algorithm based on an *a posteriori* error estimate compare to uniform mesh refinement in terms of computational efficiency.

Electrical Impedance Tomography (EIT) can provide images with well-defined characteristics only when the full non-linear reconstruction process is constrained by a property of the image such as its local smoothness, applied in parallel with the requirement to fit the data to within clearly defined statistical criteria (Blott *et al.*, 1998b, 2000). The finite element forward solution is a significant part of the computational cost of such a reconstruction (Yorkey *et al.*, 1987; Johnson and McLeod, 1994). This cost grows quickly when the image is subdivided into smaller and smaller elements to obtain an image whose accuracy is governed by the quality

of the input data alone and not by the choice of discretization. To overcome the problems involved in handling high-density discretizations, sparse matrix techniques have been applied in the past (Pinheiro and Dickin, 1997) without taking into account that a huge amount of the cost could be avoided by using meshes adapted to the problem. We have developed an algorithm which automatically adapts to the reconstructed image by producing finer meshes in areas where there are sharp gradients in the EIT image. Typically, refinement is required at interfaces between regions with differing conductivities. Although adaptive meshing has not yet been applied to resistance or impedance modelling in a biomedical context, there exists some work on applications of AMR in modelling heart current sources (Johnson and McLeod, 1994) - a topic related to EIT. We apply the auto-adaptive refinement method to the forward modelling problem and demonstrate that the method quickly reduces the number of nodes and elements so that the calculation converges much more rapidly to the true solution. In particular, to obtain the same accuracy as uniform refinement, the adaptive refinement reduces the number of elements by a factor of more than three, which yields up to an order of magnitude speed-up.

4.1 A posteriori error estimation

Once a numerical approximation φ to the continuous potential ϕ is obtained, we can estimate its error introduced by the finite element mesh discretization $\mathcal{D}$. For this, we will consider the general form of the elliptic second order boundary value problem given as

$$-\nabla\sigma\nabla\phi + b\phi + f = 0 \qquad \text{in } \Omega, \tag{4.1}$$

where σ is a given and defined function of the location $\mathbf{r}$, $\sigma = \sigma(\mathbf{r})$ and ϕ represents the solution of the equation. The boundary conditions are defined as

$$\phi = 0 \qquad \text{on } \partial\Omega_D \tag{4.2}$$

$$\hat{n} \cdot \sigma\nabla\phi = j_n \qquad \text{on } \partial\Omega_N, \tag{4.3}$$

where $\partial\Omega = \partial\Omega_D \cup \partial\Omega_N$ denotes the boundary of Ω and $\hat{n}$ is the unit normal vector on the surface of Ω.

We assume that the solution belongs to the Hilbert space $\phi \in H^1(\Omega)$. The space of functions fulfilling the Dirichlet boundary condition is called $H_0^1(\Omega)$. Now multiplying (4.1) by an arbitrary weighting function $\nu \in H_0^1(\Omega)$, and integrating by parts

$$-\int_\Omega \nu \left[\nabla \cdot \sigma \nabla \phi\right] \mathrm{dV} + \int_\Omega \nu \left[b\phi\right] \mathrm{dV} + \int_\Omega \nu \left[f\right] \mathrm{dV} = 0, \tag{4.4}$$

using the identity

$$\nu(\nabla \cdot \sigma \nabla \phi) = \nabla \cdot (\sigma \nabla \phi \nu) - \sigma(\nabla \phi) \cdot (\nabla \nu) \tag{4.5}$$

yields

$$-\int_\Omega \nabla \cdot (\sigma \nabla \phi \nu)\,\mathrm{dV} + \int_\Omega \sigma(\nabla \phi) \cdot (\nabla \nu)\,\mathrm{dV} + \int_\Omega \nu(b\phi)\,\mathrm{dV} + \int_\Omega \nu(f)\,\mathrm{dV} = 0. \tag{4.6}$$

Applying the Gauss integration formula to the first term

$$\int_\Omega \nabla \cdot (\sigma \nabla \phi \nu)\,\mathrm{dV} = \int_{\partial\Omega} \sigma \nabla \phi \nu \cdot \hat{n}\,\mathrm{dS} = \int_{\partial\Omega} j_n \nu\,\mathrm{dS}, \tag{4.7}$$

and substituting, results in

$$\underbrace{-\int_{\partial\Omega} \nu j_n\,\mathrm{dS}}_{\text{surface sources}} + \underbrace{\int_\Omega \sigma(\nabla \phi) \cdot (\nabla \nu)\,\mathrm{dV}}_{\text{volume conductance}} + \underbrace{\int_\Omega \nu b \phi\,\mathrm{dV}}_{\text{surface conductance}} + \underbrace{\int_\Omega \nu f\,\mathrm{dV}}_{\text{internal sources}} = 0. \tag{4.8}$$

Using the numerical approximation of ϕ as given by equation (3.16), substituting ϕ in equation (4.8) with φ, and replacing the continuous weighting function ν by

the discretized weighting function α_j yields

$$\int_\Omega \sigma(\nabla\varphi^h)\cdot(\nabla\alpha_j)\,\mathrm{dV} + \int_\Omega \alpha_j b\varphi^h\,\mathrm{dV} = \int_{\partial\Omega}\alpha_j j_n\,\mathrm{dS} - \int_\Omega \alpha_j f\,\mathrm{dV}. \tag{4.9}$$

Integration by parts, re-substitution of α_j by ν and expression of the solution on an elemental basis (for all elements N_e) leads to

$$\sum_{e=1}^{N_e}\int_{\Omega^e}(-\nu\nabla\cdot\sigma\nabla\varphi^h)\,\mathrm{dV} + \sum_{e=1}^{N_e}\int_{\Omega^e}\nabla\cdot(\sigma\nabla\varphi^h\nu)\,\mathrm{dV} + \int_\Omega \nu b\varphi^h\,\mathrm{dV} = \int_{\partial\Omega}\nu j_n\,\mathrm{dS} - \int_\Omega \nu f\,\mathrm{dV}. \tag{4.10}$$

Application of Gauss' integration formula and formulating the second term as sum over the jumps of $j_n = \hat{n}\cdot\sigma\nabla\varphi^h$ at internal faces and such with Dirichlet BCs leads to

$$\sum_{e=1}^{N_e}\int_{\Omega^e}(-\nu\nabla\cdot\sigma\nabla\varphi^h)\,\mathrm{dV} + \sum_{\mathcal{F}_k\not\subset\partial\Omega_N}\int_{\Gamma_k}[j_n^{e_{\mathrm{left}}} - j_n^{e_{\mathrm{right}}}]\nu\,\mathrm{dS} + \int_\Omega \nu b\varphi^h\,\mathrm{dV} = \int_{\partial\Omega}\nu j_n\,\mathrm{dS} - \int_\Omega \nu f\,\mathrm{dV}. \tag{4.11}$$

If we define the jump in the normal current density vector across inter-element boundaries as $\varrho := -[j_n^{e_{\mathrm{left}}} - j_n^{e_{\mathrm{right}}}]$ and assume that the injected currents j_n in the right-hand term are accurate currents (which is correct in the case of exact boundary modelling), we can write

$$-\nabla\cdot\sigma\nabla\varphi^h - \varrho + b\varphi^h + f = 0. \tag{4.12}$$

Subtracting this discretized version from the continuous equation then yields the residual R

$$R = -\nabla\cdot\sigma\nabla\phi + b\phi + f - \left\{-\nabla\cdot\sigma\nabla\varphi^h + b\varphi^h + f - \varrho\right\} = 0 \tag{4.13}$$

and by denoting the error of the numerical solution as $\mathcal{E} := \phi - \varphi$ we obtain

$$R = -\nabla \cdot \sigma \nabla \mathcal{E} + b\mathcal{E} + \varrho = 0. \tag{4.14}$$

Multiplication with the error as an arbitrary weighting function and integrating over the whole area gives us the error of the approximation in the form of an energy (power) norm

$$\|\mathcal{E}\|_E^2 = \int_\Omega \left(-\mathcal{E}\nabla \cdot \sigma \nabla \mathcal{E} + b\mathcal{E}^2 + \varrho\mathcal{E}\right) \,\mathrm{dV}, \tag{4.15}$$

which in form of the residuals can be written as

$$\|\mathcal{E}\|_E^2 = \underbrace{\sum_{e=1}^{N_e} \int_{\Omega^e} (-\mathcal{E}\nabla \cdot \sigma \nabla \mathcal{E}) \,\mathrm{dV}}_{\text{intra-element residual}} + \underbrace{\int_\Omega b\mathcal{E}^2 \,\mathrm{dV}}_{\text{intra-domain residual}} + \underbrace{\sum_{\mathcal{F}_k \not\subset \partial\Omega_N} \int_{\Gamma_k} \varrho\mathcal{E} \,\mathrm{dS}}_{\text{inter-element residual}}. \tag{4.16}$$

An estimate of this error may be obtained in the form

$$\|\mathcal{E}\|_E^2 \quad \approx \quad \varepsilon_G^2 \;=\; \sum_{e=1}^{N_e} \varepsilon_e^2, \tag{4.17}$$

where ε_G denotes the global error estimate assembled from the local error estimates ε_e which are associated with the e-th element as given by

$$\varepsilon_e^2 \;=\; \alpha_e \int_{\Omega^e} r_s^2 \,\mathrm{dV} \;+\; \beta_e \sum_{\mathcal{F}_k^e \not\subset \partial\Omega_N} \int_{\Gamma_k^e} r_{fc}^2 \,\mathrm{dS}. \tag{4.18}$$

Here, r_s denotes the distributed residual over the e-th element and r_{fc} denotes the element's lumped residual across inter-element faces without Neumann BC, Γ_k^e. α_e and β_e are constants which have to be determined from the elemental geometry. According to Salazar-Palma *et al.* (1998), the following expression has been derived

for triangular elements

$$\varepsilon_e^2 \;=\; f_s \frac{h^2}{\sigma p} \int_{\Omega^e} r_s^2 \,\mathrm{dV} \;+\; f_{fc} \frac{h}{\sigma p} \sum_{\mathcal{F}_k^e \not\subset \partial\Omega_N} \int_{\Gamma_k^e} r_f^2 \,\mathrm{dS}, \tag{4.19}$$

where f_s and f_{fc} are numerically estimated weighting factors associated with the surface and singular residual errors respectively. h is the diameter of the element with conductivity σ and p is the order of the approximation used.

In summary, once the error of the solution on the discretization can be estimated, this error estimate can be used to reshape/refine the discretization so that the error becomes smaller.

The basic equation of electrical impedance tomography in the case of imaging conductivity (or analogously for impedance imaging) is a reduced version of equation 4.1:

$$\nabla \cdot \sigma \nabla \phi = 0 \tag{4.20}$$

subject to the boundary conditions:

$$\phi(\mathbf{r}_\ell) = V_\ell \qquad \text{on voltage electrodes } S_{\ell_v} \tag{4.21}$$

$$\int_{S_\ell} \sigma \frac{\partial \phi}{\partial \mathbf{n}} ds = I_\ell \qquad \text{on current electrodes } S_{\ell_c}, \tag{4.22}$$

where ϕ and V_ℓ represent electrostatic potentials resulting from the injected currents $\mathbf{I}$ in direction of the surface normal $\mathbf{n}$, and S_{ℓ_v} and S_{ℓ_c} are the boundaries with Dirichlet or von Neumann conditions, respectively.

To solve equation (4.20) numerically, the problem domain is subdivided into discrete finite elements. If insufficient elements are used, the choice of discretization will affect the accuracy of the potential distribution, and also the calculation of the Jacobian in the non-linear reconstruction of the conductivities. It is therefore common practice to refine the mesh globally to improve the accuracy of the solution across the whole domain. However, it is in fact only necessary to refine the mesh where the error is large: the paradox is that the exact error is only known if the

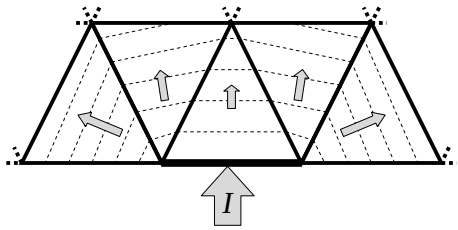

Figure 4.1: The error in potentials is caused by non-continuous normal components of the electric current across element boundaries. I is the injected current, the arrows indicate the current density in each element and the dotted lines are the iso-potentials.

exact solution is available!

We therefore use the *a posteriori* error estimate to determine whether refinement of the mesh is required. Starting with an initially rather coarse quality mesh (Shewchuk, 1996), we refine according to this estimator and adapt the mesh to give an accurate solution.

Figure 4.1 shows where the error on FE originates from - it is the normal component of the electric field which jumps between the elements, which is not possible in reality.

Analytical solutions for the forward problem only exist for very simple geometries, such as a cylinder of homogenous conductivity (see for example Appendix B). We found that there is good agreement between the *a posteriori* error estimate and the error between numerical and analytic solution for this simple case. However, the estimate should be treated as a more general approximation for more complex geometries and conductivity distributions.

4.2 Types of mesh refinement

The error estimate can be used in three ways to refine the mesh:

1. *h-refinement* consists of subdividing elements into two or more elements; h represents the element size (Burnett, 1987).
2. *p-refinement* increases the rate of convergence by using higher order interpolating basis functions on the elements (Zienkiewicz and Craig, 1986).
3. *r-refinement* relocates the existing nodes of a mesh in a more appropriate fashion without adding any new nodes (Shephard, 1985; Baines, 1998).

Efficient hybrids of these methods also exist, but can be complicated to implement. In this article, we focus on h-refinement of linear elements, which is both fast and adds relatively few additional elements and nodes to the mesh. p-refinement is an already commonly used improvement but produces larger matrices with increasing polynomial order. r-refinement requires modification of the mesh at each refinement stage but does usually not significantly improve the solution, however, it might be useful in time-dependent problems such as monitoring breathing, where the nodes of the mesh can follow predefined trajectories.

4.3 Auto-adaptive mesh algorithm

Figure 4.2 shows the steps in the adaptive meshing algorithm. We initialise the procedure with a coarse mesh and with the configuration of electrodes used. For reasons of simplicity we assume point-sized electrodes, however, the method works equally well for the complete electrode model (Somersalo *et al.*, 1992). For each step in the forward solution of the EIT reconstruction, we estimate the local error using equation (4.18) and compute the global error using equation (4.17). If the global error estimate is larger than a pre-defined threshold, the refinement procedure is started. Otherwise, the refinement is complete. The refinement algorithm then starts by marking 'primary' elements, which are those with a local error estimate above a certain percentage of the maximum occurring local error (usually 40-50 % for best efficiency).

As shown in figure 4.3, the primary elements are then subdivided into four smaller elements. This yields 'floating' nodes on the sides of adjacent secondary elements, which must be subsequently refined to maintain the required node connectivity within the mesh.

If we are using a fully nonlinear reconstruction algorithm (Blott *et al.*, 2000), then the mesh refinement steps form a natural part of the iterative solver.

4.4 Results

We have implemented the adaptive-meshing algorithm described in the previous section. Our results demonstrate the application of the method when solving the forward problem i.e. computing the potentials given the conductivities. Figure 4.4

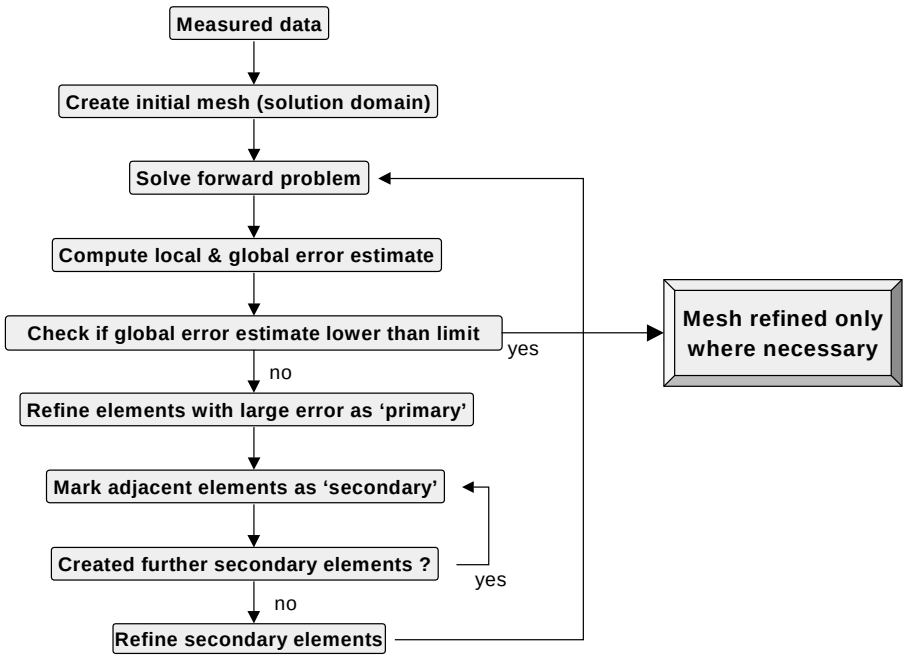

Figure 4.2: Steps in auto adaptive mesh algorithm for solution of one instance of the forward problem.

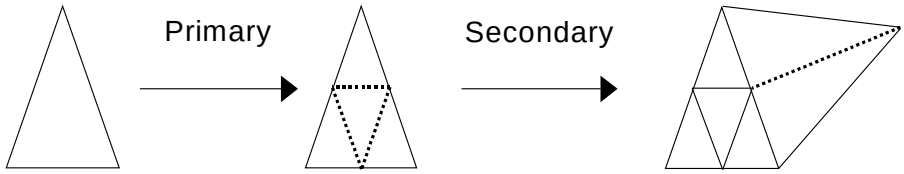

Figure 4.3: Refinement of triangular elements

shows a model of a transverse slice of the head with two electrodes, where we have used typical values for the conductivities of the tissue (0.25 S/m), bone (0.018 S/m) and cerebro-spinal fluid (1.79 S/m). This configuration could be used to monitor intra-ventricular haemorrhaging. As the mesh is refined, the equi-potential lines tend to the true solution, which we have verified using an independent FE solver (PDE-Flex). Figure 4.5 shows the method being applied where we refine the mesh at boundaries between materials with significantly differing conductivities. In a practical application of our technique, it would be desirable to combine both strategies to yield an accurate solution, which can give good resolution of material boundaries. If the image contains materials with differing conductivities, we can replace the error estimate, which determines when elements are refined, with one which refines elements based on the gradient of the reconstructed conductivity. This

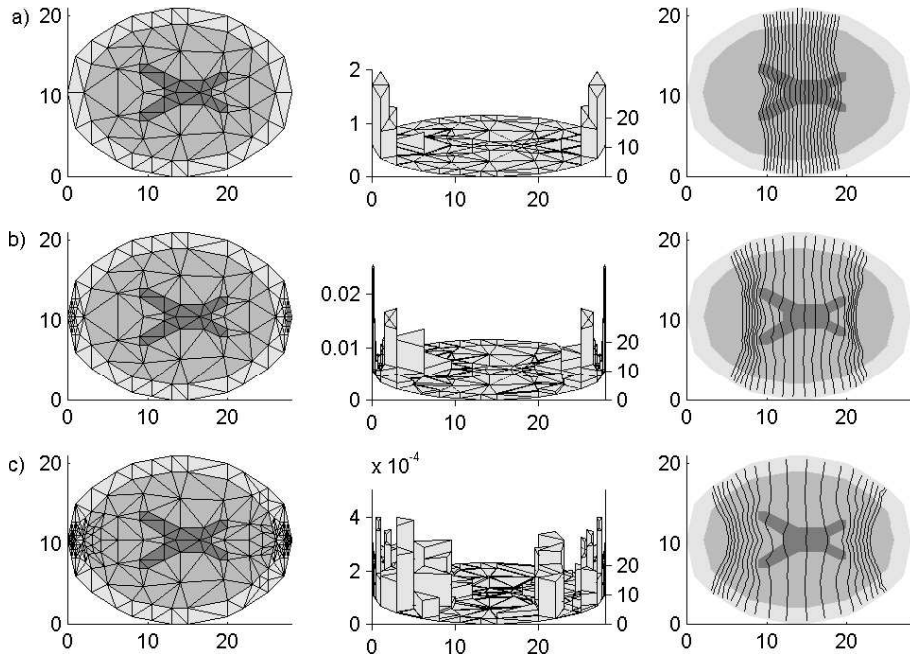

Figure 4.4: Example of auto-adaptive meshing for a head model showing bone, white matter and ventricles. (Left) Finite element mesh. (Centre) Local error estimates for each element in z-direction. (Right) Potential distribution in the region of interest for (a) the initial mesh, (b) after three refinement steps and (c) after seven refinement steps.

allows such boundaries to be more sharply resolved.

In figure 4.6 we show the performance benefits of our approach, by comparing the convergence of our method with a uniform refinement strategy. The adaptive algorithm requires only a small fraction of the number of elements/nodes in the uniformly refined mesh to achieve a given global error estimate. In particular, to attain a global error of 0.1 requires 300 elements and 0.01 seconds using the adaptive technique compared to 7000 elements and 100 seconds of compute time for the global refinement strategy. Since the solution of the forward problem scales with order between $N_N^{1.46}$ and N_N^2, where N_N is the number of nodes, reducing N_N saves both computation time and storage requirements for the system matrix.

Whilst there are many benefits of the adaptive refinement procedure, a number of numerical issues can arise. For example, the method for subdividing the elements has to be chosen in a way to avoid degenerate elements of high aspect ratios (small angles) and subsequent incorrect solutions (Salazar-Palma *et al.*, 1998). In addition, non-smooth transitions between regions of low and high mesh densities are likely to produce less accurate results (Burnett, 1987).

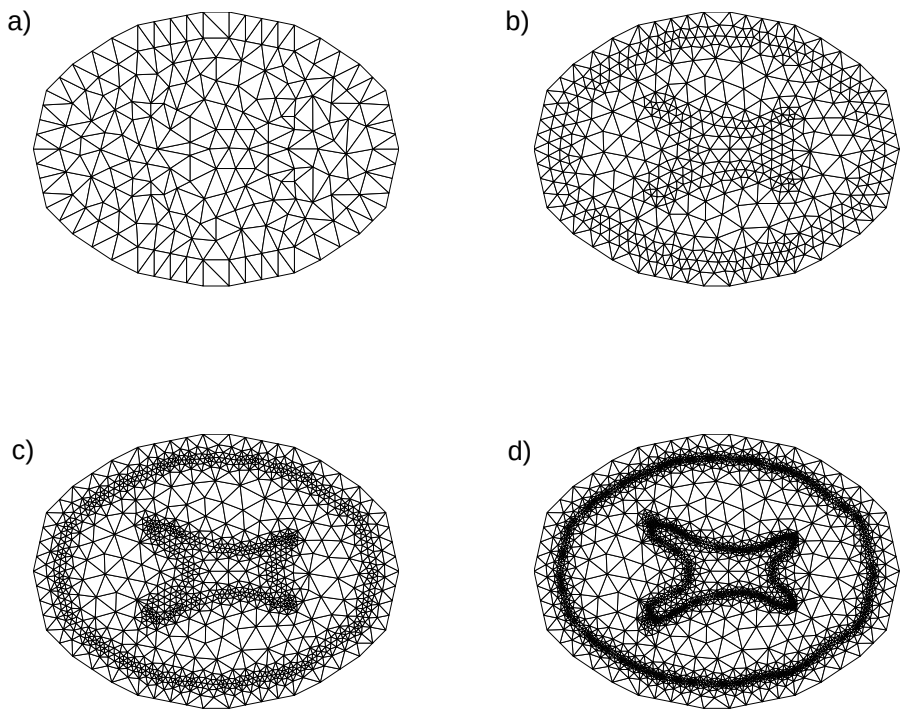

Figure 4.5: Material gradient-dependent mesh refinement provides higher resolution at material boundaries (for example for smoothing constraints). Known internal boundaries can act as prior information in the reconstruction process.

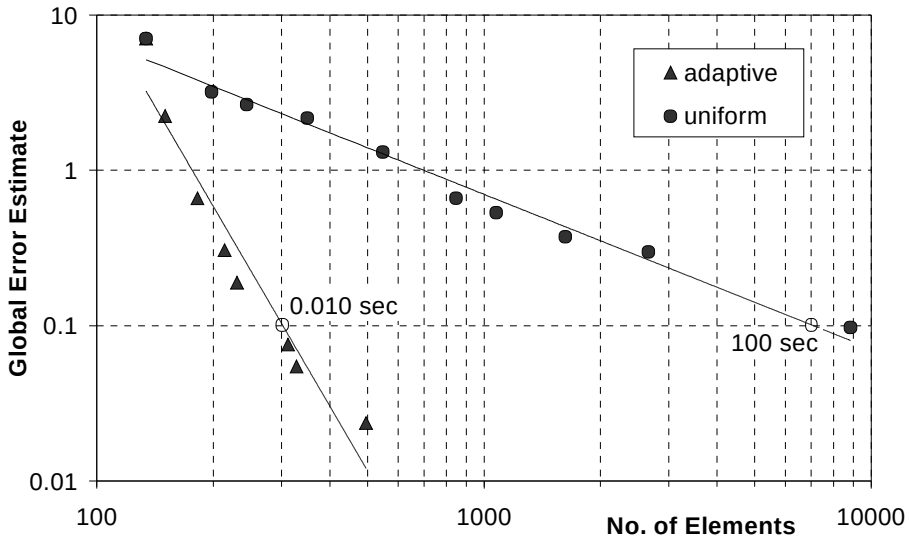

Figure 4.6: Comparison of error estimates for adaptive and uniform refinement for the head example.

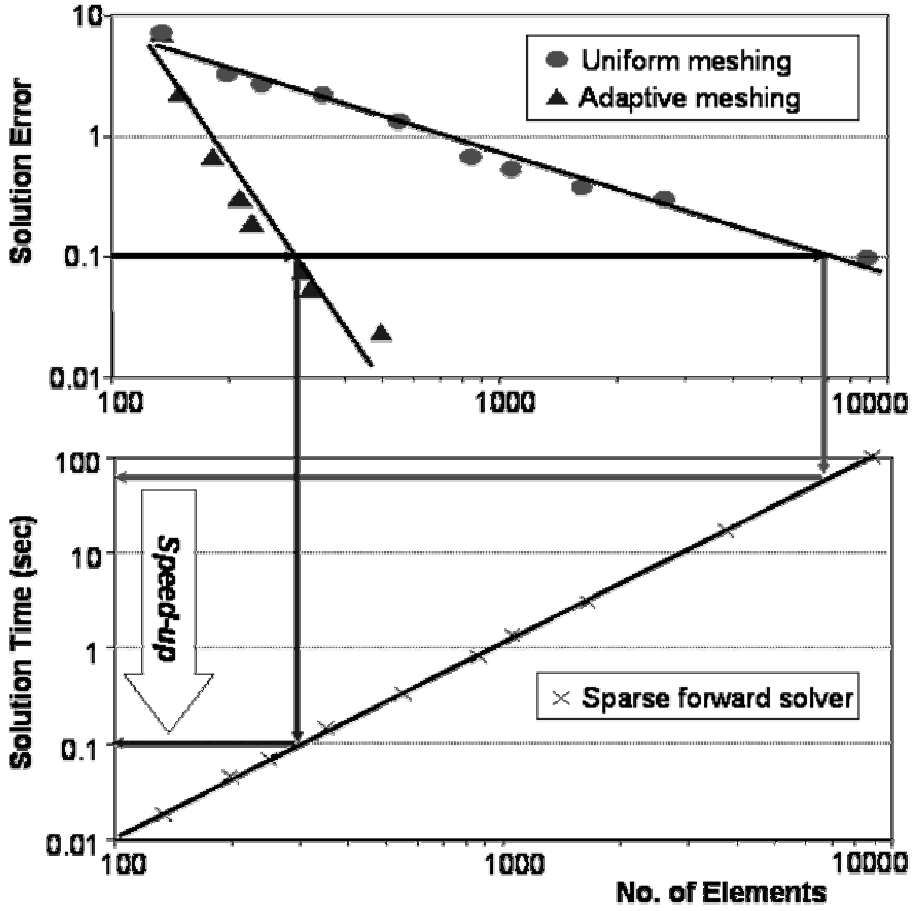

Figure 4.7: Speed-up of solution when adaptive meshing and a sparse matrix Cholesky solver is used.

Our results were obtained on a 500MHz PC with 128 MB main memory running Windows NT 4.0; the code is written in C++ and compiled using MS Visual C++ 6.0; it was later converted into Matlab.

Figure 4.7 shows the corresponding decrease in computational time spent on solving the forward solution with the sparse matrix Cholesky solver.

4.5 Effects of measurement noise on solution accuracy

Every real measurement carries measurement noise. To explore the effects of this noise on the forward solution, we simulate 100 measurements on an object with homogenous background conductivity. The simulations carry a normal-distributed random noise with a SNR of 60 dB which corresponds to a 0.1 % noise level.

We employ the complete electrode model and use a neighbouring current injection pattern for all of the 16 electrodes used. This leads to a total number of

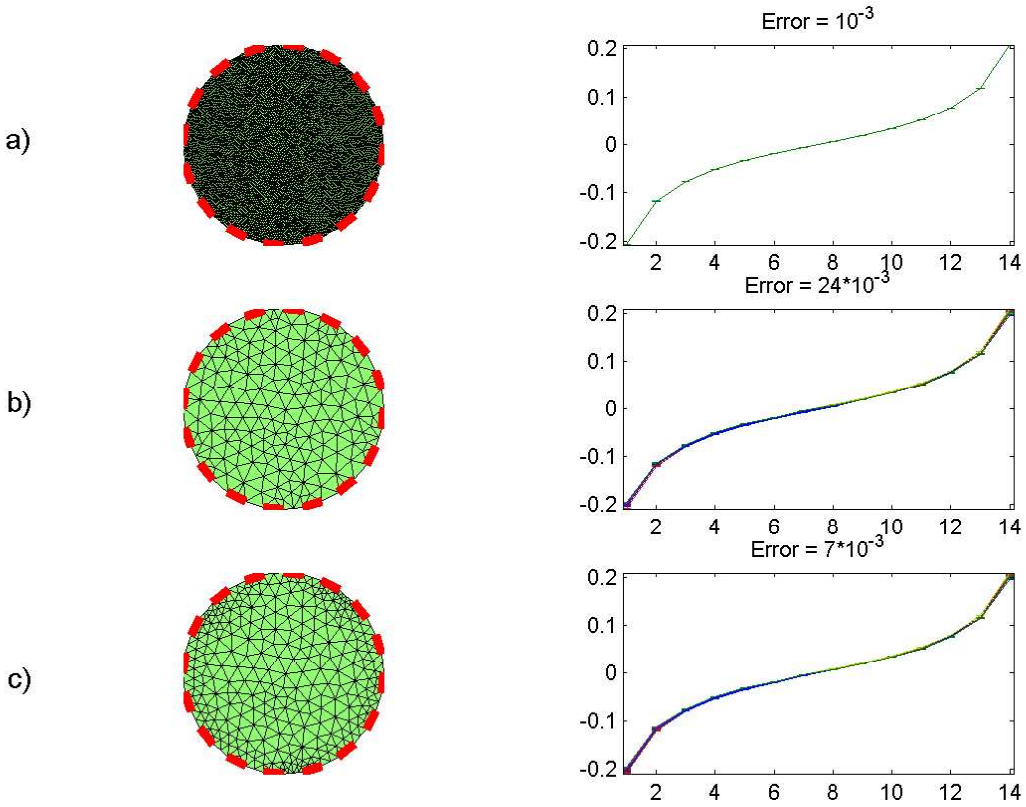

Figure 4.8: Error of forward solution. Left column: meshes and electrodes used, right column: electrode potentials and errors of a series of 100 measurements with simulated Gaussian noise at 0.1 %. (a) shows the mesh used for the simulation of the measurements with 11 890 elements, (b) represents the coarse mesh with 334 elements and (c) the mesh with 3 step mesh refinement (549 elements).

(16*13)/2 = 104 independent voltage measurements. The contact impedance is assumed to be 1/400 S/m.

The measurement simulations are performed on a 11 890 element finite element mesh and we use a base mesh of 334 elements for the solution of the forward problem. Figure 4.8 shows details of the meshes used for the simulation, forward solution on a coarse mesh and forward solution with mesh refinement. The mesh is refined based on the error estimator across the entire mesh, taking into account all current injection patterns.

The results show that the error on the simulated mesh taken over the set of 100 measurements is – as expected – $10^{-}3$, corresponding to the noise level of 0.1 %. Solving the forward problem for the whole set of experiments on the coarse mesh and comparing the electrode voltages against those obtained from the simulation, we obtain an error of approximately 2.4 %. When mesh refinement (3 steps at 40 %

of maximum error) is switched on, the electrode voltage error is reduced to 0.7 % for meshes then containing 549 elements.

We can conclude that the error of the electrode voltages overall is very small in both cases, without and with mesh refinement, however, the application of mesh refinement results in a factor 3 improved accuracy at the electrodes.

4.6 Conclusions

We have developed an efficient adaptive mesh refinement algorithm and applied it to improve the performance of EIT reconstruction algorithms by reducing both computational and storage requirements. We demonstrate its application to imaging of a section through the head and show that (i) the accuracy of the forward solution is improved using considerably fewer elements than a global refinement strategy, and (ii) the mesh resolution of interfaces between materials with differing conductivities is improved.

Our results indicate that it is possible to reduce the number of nodes required by at least a factor of three to obtain an accurate image reconstruction, over a uniform refinement strategy. This results in at least an order of magnitude improvement in the speed of the forward problem and increases the feasibility of performing fully non-linear reconstructions for complex large-scale biomedical problems in real-time using standard PC technology.

We could also show that the effects of measurement noise on the forward solution of the electrode voltages can be reduced by using adaptive mesh refinement with an example using the complete electrode model.

In the next chapter, we apply the refinement methods of this chapter to the solution of the inverse problem to investigate if our assumptions about the material gradient-dependent mesh refinement are correct.

Chapter 5

Adaptive solution of the inverse problem

In non-linear electrical impedance tomography the goodness of fit of the trial images is assessed by the well-established statistical χ^2-criterion applied to the measured and predicted data sets. Further selection from the range of images that fit the data is affected by imposing an explicit constraint on the form of the image, such as minimisation of the image gradients. In particular, the logarithm of the image gradients is chosen so that conductive and resistive deviations are treated in the same way. In this chapter we introduce the idea of adaptive mesh refinement to the 2D problem so that the local scale of the mesh is always matched to the scale of the image structures. This improves the reconstruction resolution so that the image constraint adopted dominates and is not perturbed by the mesh discretization. The avoidance of unnecessary mesh elements optimises the speed of reconstruction without degrading the resulting images. Starting with a mesh scale length of the order of the electrode separation it is shown that, for data obtained at presently achievable signal-to-noise ratios of 60 dB to 80 dB, one or two refinement stages are sufficient to generate high quality images.

Over the past three decades, much research has been carried out in the area of direct and inverse electric field problems (Geselowitz, 1971; Webster, 1990). Electrical Impedance Tomography (EIT) which measures the internal electric property distribution has become a very active research topic for medical applications. Some

advantages of EIT over other imaging methods such as MRI or X-Ray imaging are that it is very cost-effective, fast and portable but a key advantage is the close correlation of conductivity changes with physiological function.

The finite element mesh is the accepted method of image representation in contemporary EIT. The speed of reconstruction and the resolution are competing factors in the choice of finite elements; large elements reduce computational time at the expense of resolution. However, resolution can be regained where it is necessary by adaptively adjusting the size of the elements as the image is reconstructed.

In this chapter, we apply adaptive mesh refinement to non-linear EIT reconstruction and give examples of how this improves the image resolution while keeping the computational costs down. But first, we review the essential processes for generating well-characterized images in EIT; the χ^2-statistic for goodness of fit is applied in conjunction with an explicit smoothness constraint on the image.

5.1 The objective function - choice of log, image smoothness

The problem of reconstructing a scalar conductivity distribution σ within a body B consists of solving the non-linear equation

$$\nabla \cdot \sigma \nabla \phi = 0 \tag{5.1}$$

for σ. Here, ϕ denotes the potential at a point within Ω resulting from a current injection normal to the surface of Ω. We will denote the measured potentials at surface electrodes as $\mathbf{V} = \phi(\text{electrodes})$ and the electrode potentials based on the computed conductivity distribution σ as $\mathbf{U}$.

A conductivity distribution satisfying the equality of observed and predicted voltages is our target solution. However, all physical measurement processes have an inherent limitation in accuracy caused by the random noise generated in the signal source or measurement instrument. The irreducible random noise contribution $\delta\mathbf{V}$ to the signal $\mathbf{V}$ introduces statistical uncertainty in the imaging process. The

goodness of fit is then measured by the χ^2-statistic, defined as:

$$\chi^2 = \sum_{\ell}^{N_M} \left(\frac{U_\ell - V_\ell}{\delta V_\ell} \right)^2 \tag{5.2}$$

The criterion for an adequate fit is $\chi^2 \approx N_M$, where N_M is the number of independent measurements. Values of $\chi^2 \gg N_M$ would suggest significant statistical disagreement between $\mathbf{U}$ and $\mathbf{V}$ while $\chi^2 \ll N_M$ would introduce artefacts into σ solely to fit the noise in the data. Even when an adequate fit is achieved, a wide variety of solutions is possible. Because of the inherently limited spatial resolution of EIT, the values of $\mathbf{U}$ are unaffected by small spatial scale fluctuations in conductivity, even of large amplitude. Hence solutions containing these still fit the data according to χ^2 and a means to restrict the range of solutions needs to be found.

One possible method to accomplish this is to construct an explicit measure of image quality, such as smoothness. Blott *et al.* (1998b) chose a logarithmic function as the image constraint. It treats deviations in conductivity or resistivity in the same way and uses the local conductivity gradient as a definition of smoothness:

$$\Psi = \int_{\text{image}} |\nabla \log \sigma|^2 \, dxdy \tag{5.3}$$

The parameter λ is used as a weighting factor to balance between the contribution of χ^2 and the image smoothness function. λ is adjusted until χ^2 equals N_M or cannot be reduced further. In the latter case, the noise level has been misjudged or systematic errors are present. One avoidable systematic error is discretizing the image space using a mesh that is too coarse so that the values of $\mathbf{U}$ are not sufficiently accurate.

5.1.1 Newton-Raphson

The Taylor expansion of the non-linear forward problem leads to a Newton-Raphson type algorithm where updates of the conductivity lead to a local or global solution.

5.1.2 Derivation of Jacobian

In order to solve

$$J\Delta\sigma = (U - V), \tag{5.4}$$

where $\Delta\sigma$ is the change in conductivity, U is the vector containing the computed voltages at the electrodes for all current pattern applied and V contains the corresponding measured electrode voltages, we need to calculate the Jacobian J:

$$\begin{aligned}
J_{ij} &= \frac{\partial U_i}{\partial \sigma_j} \\
&= \frac{\partial}{\partial \sigma_j}(Y^{-1}I)_i \\
&= \frac{\partial (Y^{-1})_{ik}}{\partial \sigma_j} I_k \\
&= \frac{\partial (Y^{-1})_{ik}}{\partial \sigma_j} Y_{kl}(Y^{-1})_{lk} I_k \\
&= [\frac{\partial}{\partial \sigma_j}\{(Y^{-1})_{ik}Y_{kl}\} - (Y^{-1})_{ik}\frac{\partial}{\partial \sigma_j}Y_{kl}](Y^{-1})_{lk} I_k \\
J_{ij} &= -(Y^{-1})_{ik}\frac{\partial}{\partial \sigma_j}(Y_{kl})U_l.
\end{aligned} \tag{5.5}$$

J_{ij} represents the sensitivity of the voltage measured at index i (given by electrode number and current pattern index) with respect to the conductivity of element number j. J can be derived in different ways which can include the application of the identity $(A^{-1})^T = -A^{-1}A^TA^{-1}$. As we use a constant conductivity across the element, the derivative in the last row of equation 5.5 can be rewritten as

$$\frac{\partial}{\partial \sigma_j}(Y_{kl}) = \frac{\partial}{\partial \sigma_j}(\sum_m \sigma_m D_{kl}^{(m)}) = D_{kl}^{(j)}, \tag{5.6}$$

where $D_{kl}^{(j)}$ is the Dirichlet matrix of element j.

5.2 Auto-adaptive inverse solver

For the computational reconstruction the domain under investigation has to be discretized into small elements. We employ triangular finite elements with linear

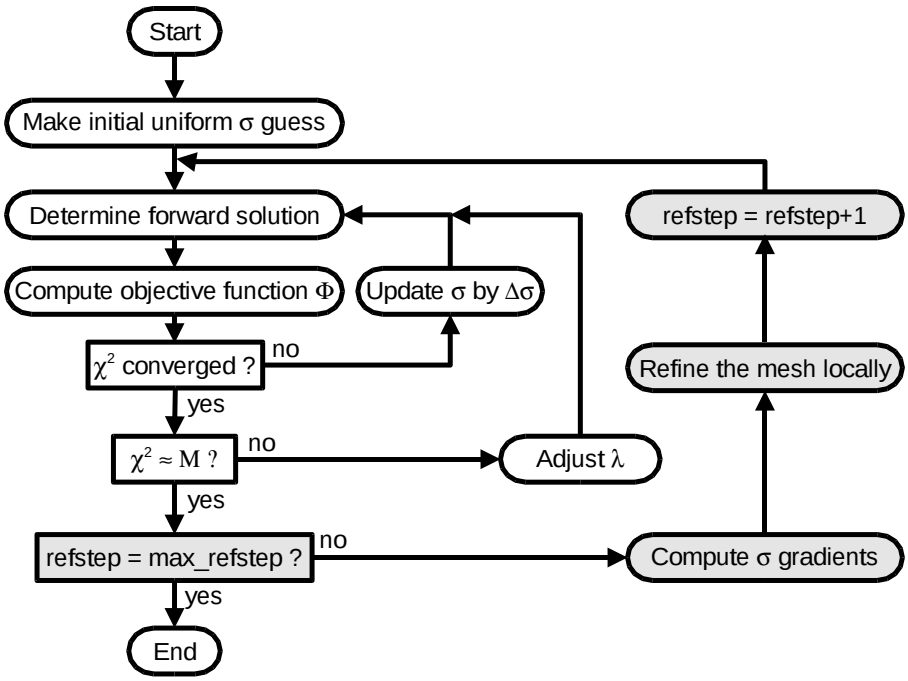

Figure 5.1: The modified iterative reconstruction algorithm incorporating material gradient estimation and auto-adaptive mesh refinement techniques. `max_refstep` defines the maximal number of refinement steps allowed.

base functions and constant conductivity. If the pre-selected mesh is too coarse, the image resolution will be very poor. However, if the discretization is very fine, the search space for solutions is large and leads to a very slow reconstruction which may not even converge. We overcome this problem by using adaptive meshing. In the case of the forward problem - computing the potential distribution given the conductivities and injected current - we have shown (Molinari *et al.*, 2001a) that the finite element mesh need only be fine in regions where high current density gradients are present. These regions were identified by an error estimator constructed from current density residuals across inter-element boundaries.

Applying the same mesh refinement technique to the inverse problem - reconstruction of conductivity knowing only electrode voltages - is now based on the conductivity gradient between the elements to obtain fine resolutions where tissue or organ boundaries are present.

Figure 5.1 shows the modification made to a standard iterative Newton-Raphson algorithm to include the mesh refinement procedure. We used the software package

Matlab to implement the non-linear iteration algorithm and finite element technique. An initial relatively coarse mesh is used to reconstruct an approximate conductivity distribution. When the $\chi^2 = N_M$ target is achieved or when subsequent iterations change the result by less than 5 %, the mesh is automatically refined in regions with high conductivity gradients. In order to apply equation (5.3) to a finite element representation of $\sigma(x, y)$ we need an approximation to Ψ. We use

$$\sum_{edges} |\log(\sigma_i) - \log(\sigma_j)|^2 l_{ij}, \tag{5.7}$$

where l_{ij} is the length of the edge separating elements i and j. For deciding on whether to refine the mesh, we use the quantity $|\log(\sigma_i) - \log(\sigma_j)|$.

As a first approach, we refine elements whose average conductivity differences with its adjacent elements is larger than 40 % of the maximal occurring difference in the mesh. This refinement criterion certainly needs adjustment as central elements exhibit a smoother transition than those closer to the boundary. In the test cases, this experimentally obtained choice always produced good results.

The selected elements are then refined by inserting vertices on the centres of all three edges. A local re-triangulation according to the Delaunay criterion (Delaunay, 1934) is carried out and subsequent Laplacian mesh smoothing (Freitag, 1997) ensures the use of near equilateral high-quality elements. This procedure is confined locally and hence very fast. It is auto-adaptive in the sense that it does not require user interaction once the parameter λ is chosen. Also, it is self-consistent in the sense that it does not require any prior information or knowledge about boundaries or approximate material distributions.

5.3 Simulation results

We have applied our algorithm (figure 5.1) to the reconstruction of data from several test structures. In this section we introduce a measure of image error, then present the reconstruction parameters and simulation results before investigating the effect of differing noise levels on the images.

5.3.1 Image comparison

To compare the reconstructed images with the simulated conductivity distributions we need a distance function as an indicator of reconstruction error. A direct method for comparing two images is to take the norm of the difference of conductivities at sample points across the image. Since we are comparing images reconstructed on triangular pixels, the simplest method to use would be to compare the material at the centre points of the finite elements. However, we are adapting and thus changing the underlying mesh including triangle sizes, shapes and positions so that this method is not applicable. In fact, some papers (for example Tang *et al.* 2001) compare images on differing meshes using this method which could result in erroneous conclusions about the reconstruction accuracy achieved.

A better way of comparing images - which is also applicable to elements with higher order internal variation in conductivity - is to resample the image on a regular (square) grid which allows for comparison across a range of images. We define the image distance D between two conductivity images, σ_1 and σ_2, by application of the L2 norm

$$D = \frac{1}{\mathrm{n_p}} \sqrt{\sum_{i=1}^{\mathrm{n_p}} \left(\sigma_1(i) - \sigma_2(i)\right)^2}. \tag{5.8}$$

Here, n_p denotes the number of total sampling points across the image. We choose to use a grid with $n_p = 10\ 000$. This corresponds to an image resolution of 1 % along each dimension.

The norm D corresponds directly to the error of a reconstructed image $\sigma_1 = \sigma_{\mathrm{recon}}$ if it is compared to the original simulated material distribution $\sigma_2 = \sigma_{\mathrm{sim}}$. We will employ this quantity to obtain the absolute average error $\mathcal{E}$ per pixel:

$$\mathcal{E} = D(\sigma_{\mathrm{recon}}, \sigma_{\mathrm{sim}}). \tag{5.9}$$

5.3.2 Reconstruction parameters

As an example we show the reconstruction of two T-shaped objects contained in a cylindrical area. The base conductivity of the cylinder is 1 S/m and the conductivities of the objects are 5 S/m and 0.2 S/m respectively for lower and upper T. We

investigate the resolution at the centre as well as throughout the image by taking cuts through the object as indicated in figure 5.2(a) which shows the original conductivity distribution. The scale of the axes is logarithmic so that the conductivity values of the two objects are $\log(5)$ and $\log(0.2) = -\log(5)$ respectively, with the background conductivity set to $\log(1) = 0$. This example tests for image resolution at the centre and also for the symmetry in treatment of conductivity and resistivity deviations.

We use the following measurement protocol: N_L electrodes driven with neighbouring current injection patterns result in $N_L(N_L - 3)/2$ independent potential measurements. We apply $N_L = 16$ equally spaced point-size electrodes around the boundary of the circular object and obtain 104 independent measurements. The simulation of the measurements was carried out on a high density unstructured finite element mesh consisting of 11 815 elements to obtain an accurate approximation to continuous matter; the computation of the measurements required 14.1 seconds. We assume the hardware measurement signal-to-noise ratio (SNR) to be in the range of 60 dB (=0.1% noise) to 80 dB (=0.01% noise), which can be achieved with today's measurement systems.

5.3.3 Results

Initial mesh elements are chosen with a scale to match the electrode spacing. Figure 5.2(b) shows the reconstruction on the initial coarse mesh with 304 elements after the $\chi^2 \leq N_M$ condition has been reached; this required 4 iteration steps. Applying one adaptive refinement step and iterating again results in the image in figure 5.2(c). We see clearly how the resolution even in the centre of the image has improved drastically. If we repeat this procedure again, further improvement is achieved, however, not as large as before if we compare the average pixel error $\mathcal{E}$.

Table 5.1 lists mesh sizes, error and reconstruction times at a noise level of 80 dB. The reconstructions were carried out in Matlab on a 900 MHz Processor with 1 GB RAM running the SuSE Linux 7.1 operating system.

The relatively large reconstruction time originates in the fact that the Newton-Raphson algorithm inverts a matrix of the size of the number of elements squared

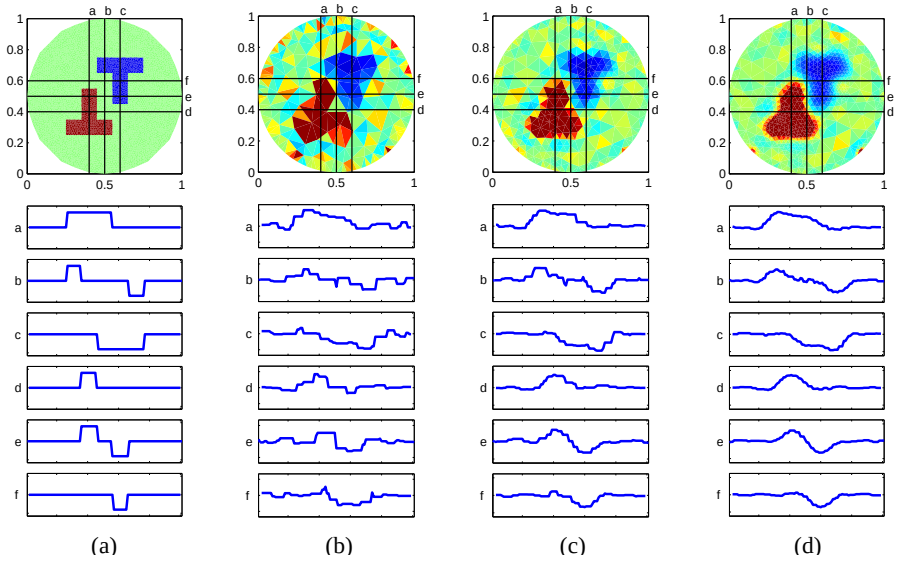

Figure 5.2: (a) Simulated conductivity distribution with $\sigma = 5$ S/m for lower T-shape and $\sigma = 0.2$ S/m for upper T-shape. (b) Reconstruction at a SNR of 80 dB without mesh refinement, (c) after one refinement step, (d) after two refinement steps. The axes show the logarithmic conductivity corresponding to the cuts indicated in the image. The image is scanned from left to right and bottom to top at the slices indicated by letters *a* to *f*.

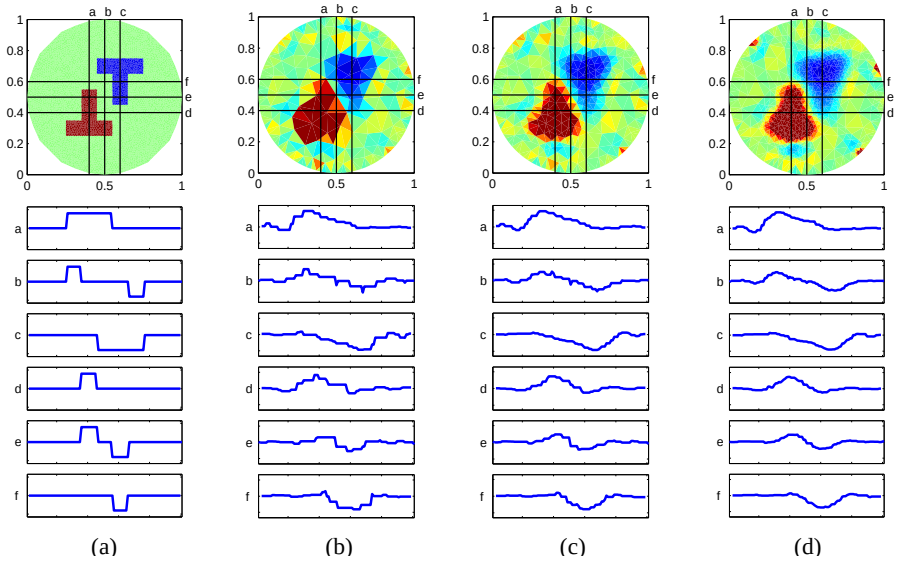

Figure 5.3: (a) Simulated conductivity distribution with $\sigma = 5$ S/m for lower T-shape and $\sigma = 0.2$ S/m for upper T-shape. (b) Reconstruction at a SNR of 60 dB without mesh refinement, (c) after one refinement step, (d) after two refinement steps. The axes show the logarithmic conductivity corresponding to the cuts indicated in the image.

Table 5.1: Reconstruction parameters before and after application of the adaptive reconstruction algorithm at a SNR of 80 dB

	Initial mesh	after 1^{st} refinement	after 2^{nd} refinement
Elements	304	533	1222
Nodes	201	316	663
Error E	0.008	0.005	0.004
Refinement (sec)	n.a.	1.10	2.22
Time/iteration (sec)	0.59	1.26	5.31
Iterations required	4	4	4($\pm$1)
Total time for reconstruction (sec)	2.36	8.50	31.96

and in the computation of the smoothness constraint for each iteration. The inversion of the matrix could be avoided by application of the so-called adjoint method (Arridge and Schweiger, 1998) which does not require the explicit computation of the Jacobian in the reconstruction process; or by using Hachtel's augmented matrix method, or by using the Woodbury formula.

5.3.4 Reconstruction at differing noise levels

We reconstructed the same test objects under the assumption of a higher noise level corresponding to a signal-to-noise ratio of 60 dB. The results are similar to those shown in table 5.1, however, the error does not decrease as fast with increasing number of mesh refinements.

A third refinement results in no further improvements which means that the error is no longer sensitive to the discretization. This leads to the conclusion that the error is determined wholly by the smoothness constraint which in turn depends on the signal-to-noise ratio of the measurement system.

Figure 5.4(d)-(f) shows the image resolution achievable at SNR levels of 60 dB, 80 dB and impossibly high 170 dB. The results suggest that further improvements are possible for higher signal-to-noise ratios until machine accuracy is reached.

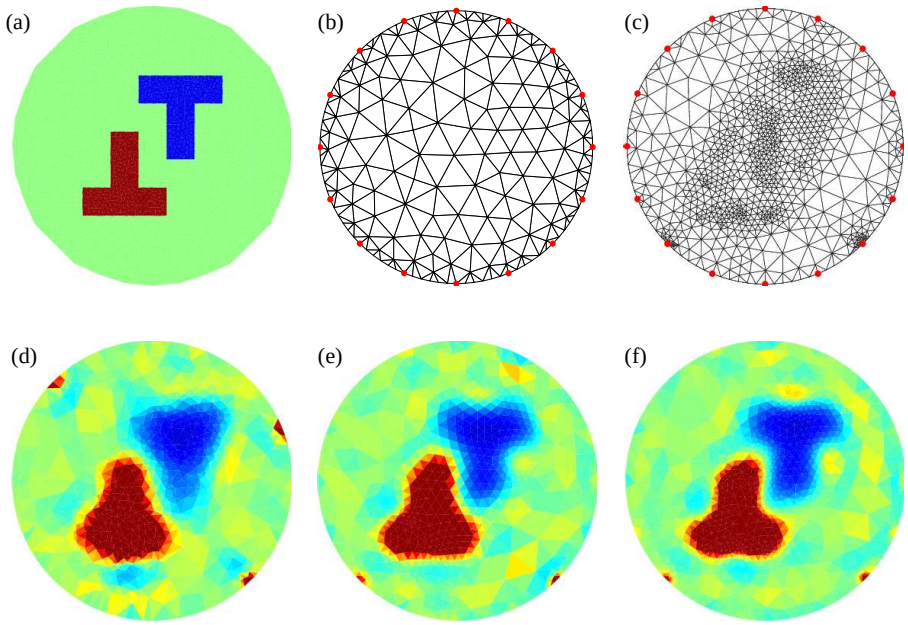

Figure 5.4: (a) Simulated conductivity distribution. (b) Initial mesh used for reconstruction. (c) Resulting mesh after 3 refinement steps during reconstruction. Reconstructions shown are at SNR's of (d) 60 dB, (e) 80 dB and (f) 170 dB.

5.4 Effects of measurement noise on inverse solution accuracy

We have shown in the previous chapter that the measurement noise affects the accuracy of the electrode potentials in the forward solution. A similar investigation can be carried out for the inverse problem: We would like to know how much this random Gaussian measurement noise affects the inverse solution accuracy. As the computational load is significantly higher, we simulate only 20 different measurements with noise (compared to 100 in the case of the forward solution).

The measurements are made on the 2D distribution as seen in the previous section. The simulations carry a normal-distributed random noise with a SNR of 40 dB which corresponds to a 1 % noise level.

We employ the complete electrode model and use a neighbouring current injection pattern for all of the 16 point-electrodes used. This leads to a total number of (16*13)/2 = 104 independent voltage measurements. The contact impedance is assumed to be 1/400 S/m.

We use the same conductivity distribution as in figure 5.3 but we calculate the error introduced by measurement noise using 20 reconstructions of random Gaussian noise.

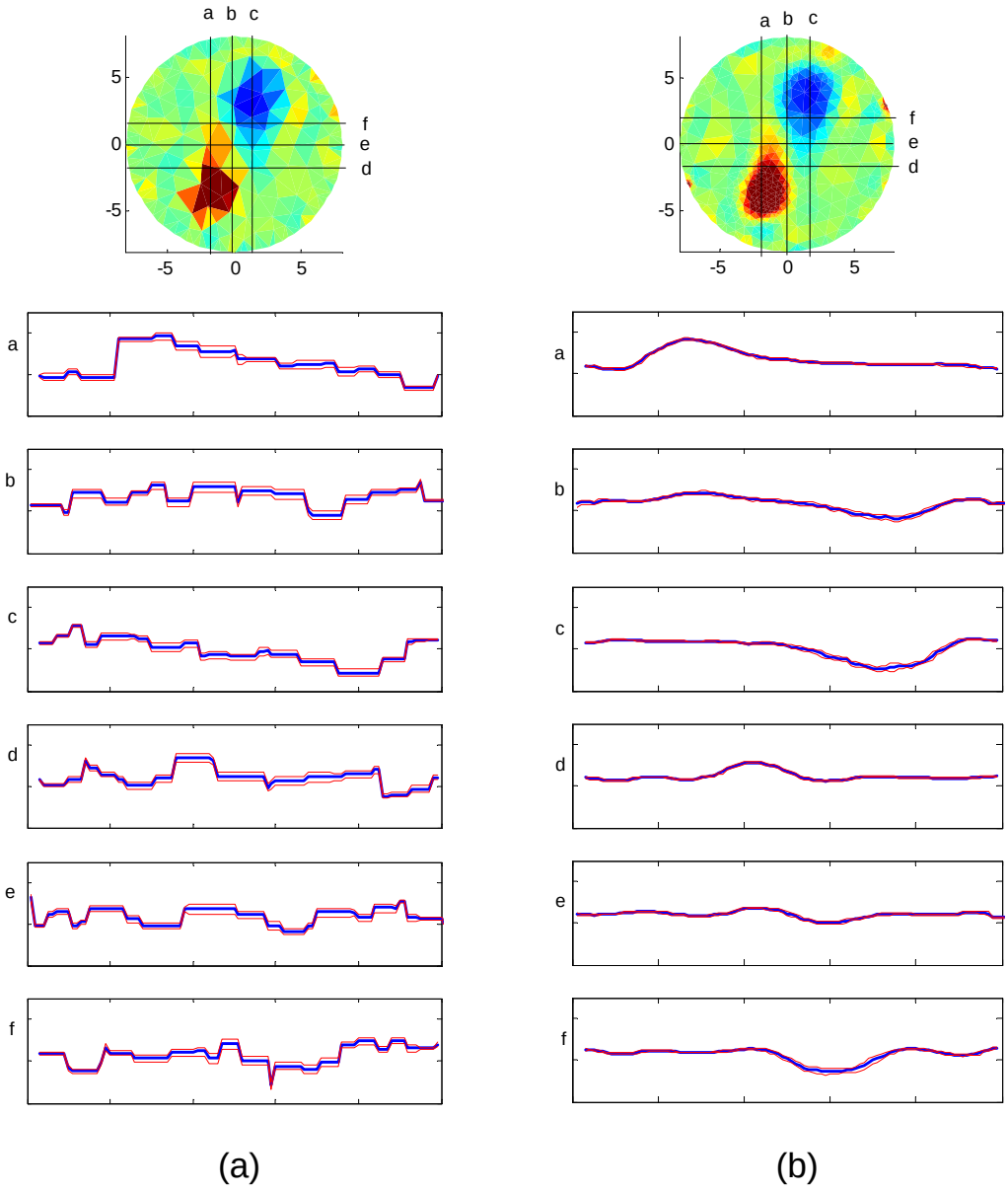

Figure 5.5: Error of inverse solution. (a) shows the mean (blue) with standard deviation (red) applied of 20 reconstructions with random Gaussian measurement noise at an SNR of 40 dB. (b) shows the same but with two stages of auto-adaptive meshrefinement carried out. Adaptive mesh refinement in the inverse problem results in a smaller effect of measurement noise on the reconstruction error and thus more robust imaging.

The results in figure 5.5 show the mean value of the 20 reconstructed conductivities on the slices a–f as a thick blue line; the standard deviation are indicated as error limits with the thinner red lines above and below the mean. We can see that the error in reconstruction due to measurement noise is reduced when mesh refinement is applied. This leads to the conclusion that the the finer the mesh around the object boundaries is, the more robust the reconstruction becomes. The better the mesh discretisation, the lesser does measurement noise affect the image.

5.5 Conclusions

In this chapter, we have focused on the issue of unavoidable random noise as the ultimate factor governing the optimum quality of image attainable in electrical impedance tomography. We have shown that the application of adaptive mesh refinement allows for the effective operation of an explicit image constraint. The choice of constraint to generate optimal images will depend to some extent on the nature of the interpretations sought by the user. Here we have chosen to select the smoothest images consistent with fitting the data. The results demonstrate clearly that the degree of detail which may be imaged depends on the level of random noise in the data. With presently available systems, the level of signal-to-noise achievable with a few seconds of data is in the range 60 dB to 80 dB. At these levels we have found that one or two refinement stages are sufficient to prevent the mesh discretization from affecting the image.

We have not considered the effect of systematic errors which may in principle be discoverable. The positions of the electrodes are measurable, but small movements during measurement may be unavoidable and their effect may need to be attenuated (Blott *et al.*, 1998a). Systematic effects may appear as distortions in the images where account may be taken of them, or they may appear as an inability to minimise χ^2 during the reconstruction process. In which case they may have to be included in the estimate of noise used to construct χ^2.

However, we have demonstrated that it is not necessary to uniformly refine the mesh to improve the solution quality, only to locally adapt where the reconstruction algorithm indicates large gradients in conductivity. This has a clear benefit in the computation time required whilst not sacrificing essential accuracy. The advantages

of tuning the element density adaptively at solution time are even greater in 3D EIT as we will see in the following chapter.

Refining the mesh adaptively has the advantage that the same image smoothness or regularisation term is better approximated in local regions of high conductivity gradients and hence the extend of the smoothing property becomes more localised and makes it feasible to resolve sharper boundaries more easily.

We have also shown that the better the discretisation is adapted to boundaries within the volume, the more robust the algorithm becomes with respect to measurement noise effects.

If in addition to the conductivity also the electrical permittivity is reconstructed, either an additional mesh with refinement only around high gradients of the permittivity can be used or the same mesh as for the conductivity with both material-gradient refinements applied. The investigation of the effects of these two differing methods on the performance of reconstructions needs to be investigated as part of future work.

Chapter 6

From 2D to 3D EIT

Non-linear electrical impedance tomography reconstruction algorithms usually employ the Newton-Raphson iteration scheme to image the conductivity distribution inside the body. For complex 3D problems, the application of this method is not feasible any more due to the large matrices involved and their large storage requirements. In this chapter we demonstrate the suitability of an alternative conjugate gradient reconstruction algorithm for 3D tomographic imaging incorporating adaptive mesh refinement and requiring less storage space than Newton-Raphson. We compare the reconstruction efficiency of both algorithms for a simple 3D head model. The results show that an increase in speed of about 30 % is achievable with the conjugate gradient-based method without loss of accuracy.

The generation of electrical conductivity tomograms from external measurements is approaching the limits of development using 2D models (Holder and Brown, 1993; Blott *et al.*, 1998b; Vauhkonen *et al.*, 2001). The principals of the reconstruction method are the incorporation of a statistical test of acceptance for how well the reconstructed image accounts for the data bearing in mind the noise in the measurements, and the creation of a measure of the image characteristics. The latter "smoothness" measure is essential to ensure that only the features in the image that can be relied upon are retained. The inverse problem is then solved with a non-linear Newton-Raphson (NR) algorithm. The calculation of the tomograms is implemented with the aid of a finite element mesh in which, to keep computing

time down, the element size is adapted to match the scale of the image variations (Molinari *et al.*, 2002b).

In three dimensional medical electrical impedance tomography the complexity of body shapes and components requires a large number of mesh elements which raises new computer capacity problems on single processor systems. Either the mesh discretization becomes too coarse to obtain images unaffected by the element size, or it causes the computer to run out of memory with the commonly used algorithms. There exist two ways of addressing this capacity problem: (1) to parallelise and thus distribute the problem onto several processors (Paulson, 1992; Woo *et al.*, 1993; Blott *et al.*, 2000) and (2) to investigate alternatives to Newton-Raphson for the optimization problem – we will focus on a non-linear conjugate gradient (CG) approach.

After reviewing, in the next section, the requirements for efficacious reconstruction algorithms on electrical impedance tomography, we take the second approach and give details about our implementation of a Newton-Raphson based algorithm as well as a new conjugate-gradient algorithm to solve the 3D inverse problem. In the section thereafter, we compare the efficacy of these two algorithms applied to the reconstruction of a simple head model before we finally draw our conclusions.

6.1 Issues involved (slicing etc.)

Table 6.1 summarizes the major requirements for algorithms applicable to medical electrical impedance tomography. The model of an object created in the pre-processing stage affects the flexibility of the algorithm which impacts on the whole reconstruction process. Accuracy and speed are mainly affected by numerical code implementations. After a satisfactory solution is obtained, its visual representation in a medically useful format should not be overlooked. Visualization characteristics in the post-processing stage often depend on the initial model and the reconstruction algorithm used.

Some of the requirements listed in table 6.1 have been addressed in the context of 3D electrical impedance tomography in previous works, others still remain to be investigated. Amongst these are:

- Accurate boundary shape representation as investigated for 2D problems by Jain *et al.* (1997).
- Modelling of general object shapes, such as the head (Gibson *et al.*, 2000)
- High reconstruction times caused by large dense matrices
- Resolution inaccuracies caused by deficient element quality (Vauhkonen *et al.*, 1999)
- Accounting for the influence of off-plane structures in 3D reconstructions (Metherall *et al.*, 1996).

6.2 From Newton-Raphson to Conjugate Gradient

Our reconstruction of a conductivity distribution σ within a volume conductor Ω by means of electrical impedance tomography is based on the minimization of a functional Φ, which employs the statistical χ^2-criterion for goodness of fit. It works on the difference between computed $\mathbf{U}$ and measured $\mathbf{V}$ electrode voltages, $U_i - V_i$, for all measurements $i = 1 \ldots N_M$ and accounts for the measurement error δV_i. A well-defined reconstruction is ensured by the image smoothness term $|\nabla \log \sigma|^2$:

Table 6.1: Requirements for an efficient EIT reconstruction algorithm for medical applications (extended from Molinari *et al.* 2001c)

Flexibility	Accurate modelling of complex 2D and 3D geometries Easy application of differing electrode types Possibility of node relocation for dynamic imaging
Accuracy	Usage of high-quality domain discretization Robustness with respect to noise Minimal influence of algorithmic constraints on solution accuracy Suitable algorithm for the problem's non-linear nature
Speed	Application of sparse matrix storage schemes and solver techniques Algorithm with problem-adaptive mesh density Parallelization of code
Visualisation	Extraction of medically significant features from image Display of slices, surfaces, volumes

$$\Phi = \sum_{i=1}^{N_M} \left(\frac{U_i - V_i}{\delta V_i} \right)^2 + \lambda \int_\Omega |\nabla \log \sigma|^2 \, d^3x \tag{6.1}$$

$$= \chi^2 + \lambda \Psi. \tag{6.2}$$

This system is equivalent for two- and three-dimensional problems. A more detailed discussion of this functional and the determination of the parameter λ can be found in Blott *et al.* (1998b). There exist a number of techniques to estimate λ from solutions obtained. These include the L-curve method, the generalised cross-validation method and Morozov's discrepancy principle, however, the details of these are outside the scope of this work.

Since there exist no analytic solutions to the generalized problem, we employ the well-studied finite element method (Burnett, 1987) to discretize Ω for a numerical solution. We use tetrahedral elements with piecewise linear base functions for the potentials and a constant conductivity parameter. This choice reduces the size of the matrices involved and therefore ensures an efficient reconstruction compared with higher order interpolation. The main advantages of the finite element discretization compared to other numerical methods are its flexibility in terms of geometry and application of different types of boundary conditions imposed by the electrodes used. These outweigh by far the disadvantage of the rather complex coding of finite element programs.

To minimize equation (6.1) with respect to the discretized conductivity distribution σ, we initially employ the non-linear Newton-Raphson iteration scheme for which Yorkey *et al.* (1987) showed fastest convergence out of a number of 2D ET reconstruction algorithms.

This iterative algorithm updates an initial homogenous conductivity guess by $\Delta\sigma$ during each iteration according to the following formula:

$$\left(J^T J + \lambda R\right) \Delta\sigma = J^T \left(\frac{\mathbf{V} - \mathbf{U}}{\delta \mathbf{V}} \right) + \lambda \mathbf{r}. \tag{6.3}$$

The solution of this system involves the construction and Cholesky decomposition of the large dense sensitivity matrix $J^T J + \lambda R$ of size N_E^2, where N_E is the number of finite elements. J denotes the Jacobian weighted by the measurement uncertainties $\delta \mathbf{V}$. R and r are a sparse matrix and a vector respectively, both introduced by the image smoothness term in equation (6.1). While R is constant for a mesh and has to be computed only once, J and r require updating during each iteration step.

The repeated computation and subsequent Cholesky decomposition of the dense sensitivity matrix makes the Newton-Raphson approach unsuitable for large complex 3D problems as N_E can easily exceed 5000, which corresponds to a matrix size of $25 \cdot 10^6$ or a memory requirement of 200 MByte to store the matrix alone.

An alternative approach is the application of a non-linear conjugate gradient (CG) algorithm. This type of algorithm is well-studied (Hake, 1992) and recognized as one of the most suitable numerical algorithms for complex ill-conditioned large-scale applications (Golub and O'Leary, 1989; Arridge and Schweiger, 1998). The CG method searches for a minimum of the functional Φ by taking conjugate search directions for every iteration step and requires the computation of the gradient of Φ only, instead of the full second derivative. Different choices for finding the minimum along a search direction exist. The application of an inexact line search algorithm does avoid the necessity of computing the Jacobian for every iteration step. We implemented the CG algorithm with the Polak-Ribière parameter updating technique (see, for example, Shewchuk 1994).

Figure 6.1 and figure 6.2 show the two algorithms with the auto-adaptive mesh refinement wrapper. Both algorithms terminate when the statistical criterion $\chi^2 \approx N_M$ is satisfied, where N_M is the number of independent measurements made, and the targeted number of refinements is reached.

6.3 Adaptive mesh refinement in 3D

The speed and accuracy of the imaging process – the reconstruction of conductivities given only surface potential measurements – depends not only on the algorithm used but also strongly on the underlying finite element discretization. We have shown that adaptive mesh refinement techniques can have a major impact on the efficient

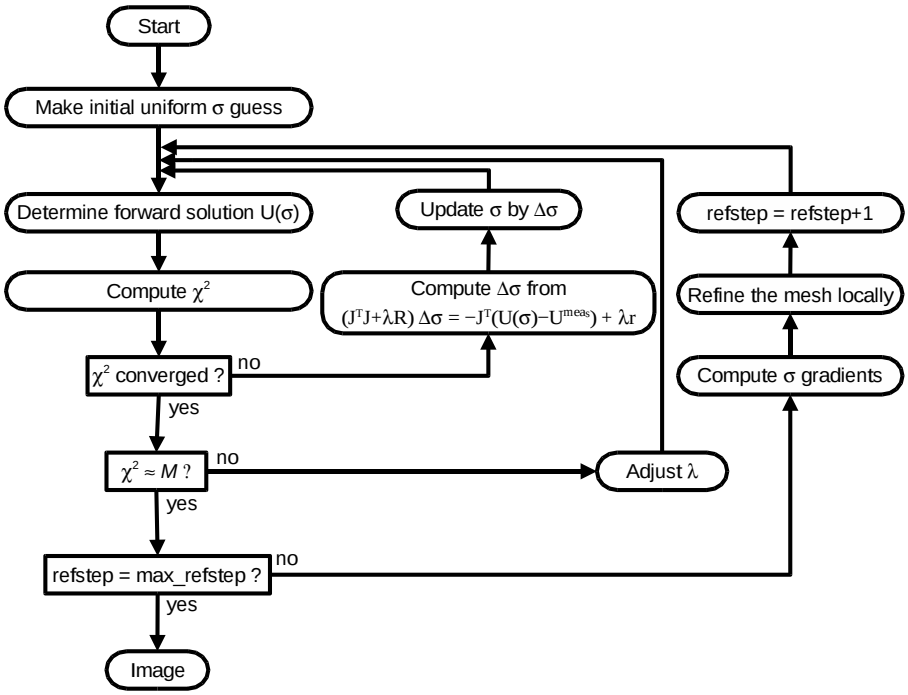

Figure 6.1: Outline of Newton-Raphson imaging algorithm with adaptive mesh refinement in the reconstruction process.

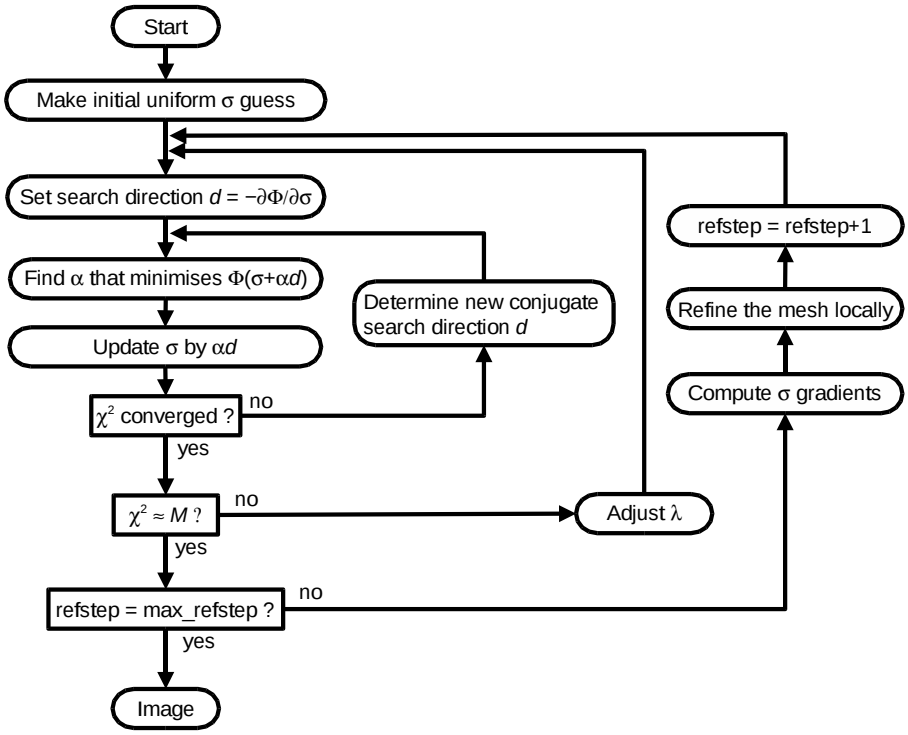

Figure 6.2: Outline of the non-linear conjugate gradient algorithm. Not shown are parameters such as termination criteria, Polak Ribiére updating and restarting criteria.

solution of the forward problem (Molinari *et al.*, 2001a) as well as on achieving the image resolution intrinsic in the data (Molinari *et al.*, 2002b).

We have modified the NR and CG algorithms to include mesh refinement techniques. *h-refinement* – the subdivision of elements in the initial rather coarse mesh – is fast and offers a number of additional advantages, such as maintaining the underlying element geometry and focusing on selected areas (Burnett, 1987), as well as being applicable to both the forward solution and the inverse problem. An error estimator in the former case and a conductivity gradient indicator in the latter case determine the elements to be refined. In three dimensions, the number of possible subdivisions of these selected elements is larger than in 2D thus allowing for more flexible control over local element density in the mesh as indicated in figure 6.3.

Refinement for the inverse problem is carried out when the χ^2-criterion is met after a number of iterations. Thus, the adaptive refinement code *wraps* around the actual algorithm. The flow diagram assumes that the initial mesh is not so coarse that $\chi^2 \approx N_M$ cannot be reached. Tests at 80 dB signal-to-noise level have shown that after three refinement stages, no significant improvement is achieved by further refining the mesh.

To maintain the node connectivity within the mesh after adding a number of nodes, a local Delaunay re-triangulation (Golias and Dutton, 1997) of the nodes within and adjacent to the refined elements is required. This can be carried out quickly and efficiently with, for example, the Qhull algorithm (Barber *et al.*, 1996).

Element-centred point insertion maintains the element boundaries and adds only 3 further elements within the existing one. This leads to the addition of relatively few elements at the expense of distorted element geometries. It is advisable to maintain element geometries which are as close as possible to equilateral tetrahedra. This so-called *high-quality mesh* avoids geometrical anisotropies causing numerical errors, especially in the region around the electrodes. The addition of 6 nodes on the edges of a selected element leads to the addition of 7 elements of similar quality to the base element and should hence be preferred to the former two methods.

Mesh-conforming refinement is essential as the potential values of the forward solution computed at the nodes are used in the computation of the sensitivity

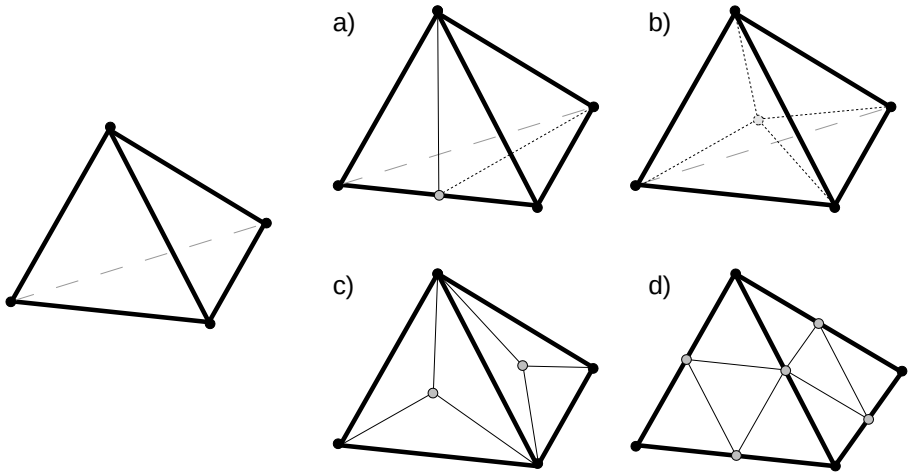

Figure 6.3: *h*-refinement by point insertion for 3D tetrahedra: (a) longest-edge bisection; (b) element-centred, (c) face-centred and (d) edge-centred point insertion.

matrix, J, in the Newton-Raphson procedure. This means that some of the nodes used in the computation of the forward solution must correspond to the nodes at which potential values are evaluated for the inverse solution. This is either done by using a base mesh and refining it according to its task (accurate forward solution or high conductivity boundary resolution) or combining these two meshes into one which incorporates both features. The latter option has the disadvantage of producing a large number of elements in places not specifically required for the inverse problem and hence causes longer computation times than necessary. Its advantages are the easier algorithmic implementation and the potential of quality improvement by relocating nodes in the centres of their adjacent neighbours – the *Laplace-Smoothing* discussed in chapter 3.1.7.

6.4 Simulation results

We show results from reconstructions obtained with the algorithms described above on synthetic data. We use a simple dummy head model made up from a combination of solid-constructive-geometry objects, such as cylinders and spheres, and meshed with Netgen (Schöberl, 2001). We simulated three conductivity parameters within the head mesh consisting of 40 216 elements: the head itself filled with grey matter of 0.15 S/m (Foster and Schwan, 1989) and a mouth region of an estimated 0.01 S/m as well as a blood clot of 0.67 S/m (Geddes and Baker, 1967) in a central region

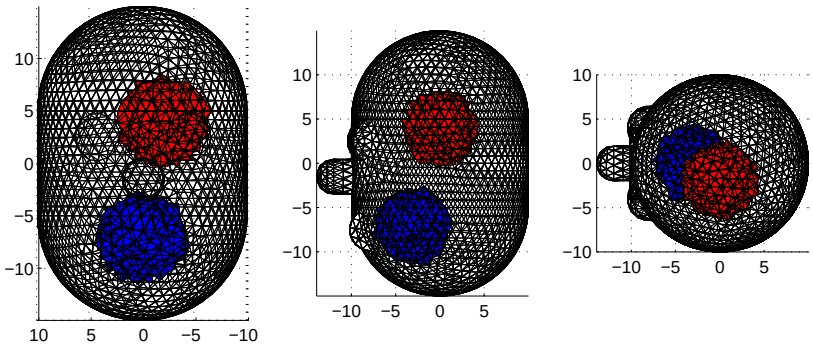

Figure 6.4: Front, left and top view of head dummy simulation with background conductivity (grey matter, 0.15 S/m), mouth cave region (air, 0.01 S/m) and object behind left eye (blood 0.67 S/m).

behind the left eye of the patient. Figure 6.4 shows the simulated materials in front, side and top view and Figure 6.5 shows slices at the indicated heights.

To avoid shape mismatch between the electrodes applied to the surface in the forward case and those in the inverse case, we decided to employ point electrodes. The algorithm, however, is equally applicable to the complete electrode model as introduced by Somersalo *et al.* (1992). 24 electrodes in total have been applied – 6 on top, 6 at the back and 6 on each side of the head – to ensure an appropriate coverage of the surface. Current injection is performed through both opposed and adjacent electrode pairs so that a total of 24 current patterns was used. This corresponds to a total of $(24 \times 21)/2 = 252$ independent potential measurements. We assumed a signal-to-noise ratio of about 80 dB in the measurements, which is about the best achievable with current technology.

The initial mesh for the reconstruction consists of 5027 elements which corresponds to a spatial resolution of about 5.8%. This model does not take into account the possible shunting effect by the skin and insulation by the skull barrier. These might affect the reconstruction from real measurements significantly. However, we are mainly concerned here with the performance aspects of the algorithm rather than the fidelity of the simulation.

Imaging results:

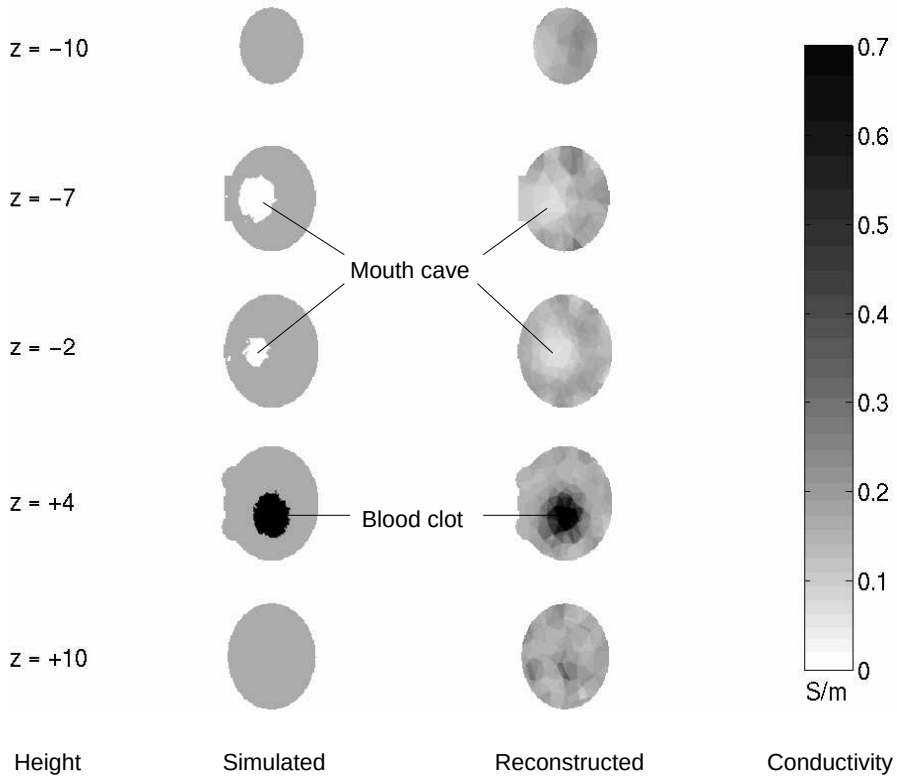

Figure 6.5: Slices through the head at the indicated heights showing the conjugate gradient based reconstructed conductivity distribution. The centre-left column represents the original values and the centre-right column displays the reconstructed values. Mouth cave and blood clot are clearly detectable. The range of reconstructed conductivites lies within the simulated values as indicated by the colour distribution. The Newton-Raphson result is visually indistinguishable.

Figure 6.5 shows the result of the CG algorithm which is visually indistinguishable from the NR algorithm. The quantitative analysis of the pixel error $\mathcal{E}$ in table 6.2 reveals that both algorithms perform also equally well in terms of absolute conductivity reconstruction. $\mathcal{E}$ is the averaged Frobenius norm of the difference between simulated and reconstructed conductivities sampled on a $100\times100\times100$ point grid.

Although CG requires much less memory than Newton-Raphson, many more iterations have to be carried out to reach the statistical χ^2 stopping criterion. The large number of iterations required increases the solution time and partly balances out the speed advantages. Nevertheless, our new CG based approach achieved a 28% decrease in computing time. The calculation was performed using Matlab Release 12 on a 900 MHz processor PC with 1024 MB of memory and running the

Table 6.2: Comparison of Newton-Raphson (NR) and conjugate gradient (CG) algorithms

	Newton-Raphson	Conjugate gradient
Storage requirement (MByte)	220	7.8
Number of iterations	9	172
Solution time (min)	16.9	12.2
Average pixel error $\mathcal{E}$(S/m)	0.0136	0.0143

SuSE Linux 7.1 operating system.

6.5 Discussion & Conclusions

The iterative Newton-Raphson method is the method of choice for small scale electrical impedance tomography problems. It exhibits robustness and high accuracy in the absolute imaging of synthetic data. When it comes to 3D imaging with arbitrarily shaped complex geometries, such as the head, this method becomes more and more unsuitable due to the large matrices involved. Storage and computing time rises as a factor of the number of elements involved and hence an alternative algorithm has to be found.

We have investigated the possible use of a non-linear conjugate gradient based algorithm. The results presented show that it is superior to Newton-Raphson in terms of speed and storage requirements as only the first derivative of the objective function needs to be computed. This leads to an increase in speed of about 28 % for our example which consists of about 5000 elements only. As conjugate gradient time complexity scales with $\mathcal{O}(N_E^{4/3})$ (Shewchuk, 1994), where N_E= number of elements, compared to Newton-Raphson which scales with $\mathcal{O}(N_E^3)$, significantly larger differences in reconstruction speed can be expected if even more elements are used. The fact that the conjugate gradient algorithm is easier to parallelize onto several processors (Takeda *et al.*, 2000) makes it a suitable candidate for 3D electrical impedance tomography reconstructions. It is in particular more suitable for complex large-scale problems when the number of elements increases above 10 000 and the matrices involved would require too much memory in the Newton-Raphson method.

To obtain fast reconstructions, not only the algorithm employed, but also technqiues such as adaptive mesh refinement play a crucial role. We have presented a number of possible refinement strategies for 3D tetrahedral finite elements which help to increase mesh density where required for forward and inverse problem solution. Further work is required to find the best way of obtaining the most suitable high-quality finite element mesh for image reconstruction and to investigate the usefulness of special numerical tools such as the Woodbury formula. These and the parallelization in 3D of the new conjugate gradient based code will be the next problems to address in non-linear three-dimensional electrical impedance tomography.

Chapter 7

Conclusions

7.1 Summary of main findings

The aim of this PhD project has been to investigate the inverse problem in electrical impedance reconstruction and to develop appropriate algorithms for fast and accurate imaging purposes in two and three dimensions.

Chapter 1 presents the possible applications of Electrical Impedance Tomography. We identified the requirements for modern EIT as high speed/real-time reconstructions of high resolution images and concentrated on the reconstruction of absolute and static images.

In chapter 2, we reviewed the physical basis and mathematical models for EIT and discussed the general properties of inverse problems. We discretized and approximated the derived continuous equations using finite element analysis as numerical tool in chapter 3 as well as addressed the issues of boundary condition, convergence and error estimation on the finite element mesh. We were able to show that the error at the edges of electrodes is largest and thus requires a finer mesh to model the solution more accurately across the domain.

Throughout the course of this work, a software package for finite element mesh computations (SMESH) has been developed in Matlab and the routines have been optimised in terms of computational speed. An additional suite of Matlab functions (SEEIT) has been developed to deal with the reconstructions of impedance images.

In chapter 4 we introduced adaptive mesh refinement techniques to the field of EIT modelling. Based on an *a posteriori* error estimation on the forward solution,

we were able to show that this technique increases performance of both simulation and solution of the inverse problem by approximately an order of magnitude. This allows for faster image acquisition than using a globally fine mesh while preserving the resolution required for an accurate solution. The adaptive meshing affects the voltage prediction in the forward solution as well as the sensitivity accuracy as the sensitivity matrix is modelled using the same interpolation functions.

Adaptive mesh refinement has also been implemented into a Newton-Raphson based reconstruction algorithm in chapter 5. In this case, the refinement has been based on the gradient of conductivities in the computed image. This particularly novel approach shows that the application of adaptive mesh refinement allows for the effective operation of an explicit smoothness constraint on the image. We have reconstructed images at different measurement noise levels and showed that the degree of detail in the image can be made independent of the finite discretization and is only limited by the noise in the measurements. An additional benefit is the faster reconstruction by focussing the available computational resources on key regions for the forward solution and inverse reconstruction.

We have demonstrated that local adaption of the finite element mesh to changes in conductivity has a clear benefit in the computation time required whilst not sacrificing essential accuracy. In addition does mesh refinement give a better approximation to local variations in the smoothing constraint which leads to better localised image resolution.

Furthermore, numerical simulations of the reconstruction error caused by random Gaussian noise in the voltage measurements showed that refined meshes result in a more stable behaviour of the reconstruction algorithm and a much reduced effect of the noise on the final image.

If in addition to the conductivity also the electrical permittivity is reconstructed, either an additional mesh with refinement only around high gradients of the permittivity can be used or the same mesh as for the conductivity with both material-gradient refinements applied. The investigation of the effects of these two differing methods on the performance of reconstructions needs to be investigated as part of future work.

Although the introduced mesh refinement concentrates computing power to regions where required by the algorithm, the imaging algorithm based on the Newton-Raphson scheme is computationally still very expensive. Chapter 6 introduces an alternative non-linear conjugate gradient based algorithm for the reconstruction of the image. We could show that the advantages of tuning the element density adaptively at solution time are even greater in 3D EIT compared to 2D. The results show that non-linear 3D imaging is now possible on machines with less power but with a conservation of the high pixel resolution in the image.

7.2 Suggested future work

This work has specifically focused on the reconstruction algorithm and its implementation with adaptive finite element meshing. There are still a number of issues which need to be addressed in the future to enable EIT to become a fast routine application in the medical and/or industrial sector.

The computation of the Jacobian – which is required for both methods (NR & CG) – is still the computationally most expensive part in computed impedance tomography. An alternative to investigate would be the method of adjoint sources as described in Arridge and Schweiger (1998) or to use Hachtel's augmented matrix method.

Our developed software routines and algorithms will allow further research into issues not yet solved in Electrical Impedance Tomography, such as the effect of electrode size, location and discrete representation on the final image, as well as convergence behaviour of a number of different algorithms.

The combination of the different optimisation techniques (mesh refinement, fast numerical algorithms, adaptive current patterns, electrode positions, etc.) could lead to even more improved solutions and efficiency of the combined process.

Software will be required which is suitable for distributed computing on PC clusters and on the Grid. In particular for image farming purposes (as described in Appendix C).

A full impedance reconstruction method using adaptive mesh refinement needs to be derived – in particular for applications in which both, the reconstruction of conductivity and electrical permittivity are of equal importance.

In addition to the mesh refinement methods, it would be interesting to investigate de-refinement methods and also consider intelligent meshes which adapt themselves to prior information of the object and thus to the expected image.

An as yet unsolved problem in EIT is the computational geometric modelling of electrodes in finite element meshes, in particular surface electrodes for medical 3D imaging. This field could prove important for future work in EIT as the electrodes contribute some of the largest errors towards the reconstructions. Extending this field of computational geometry to the remeshing of not only electrodes but also fixed or moving internal boundary structures offers potential for a large range of further research.

Appendix A

Triangle Integration Formulas

In finite element analysis, we often encounter integrals of the basis or shape functions over the area or along an edge of a regular triangular element, for example,

$$I_1 = \iint_{\Omega^e} \varphi_i(x,y)\varphi_j(x,y)\ dx\ dy, \tag{A.1}$$

or

$$I_2 = \int_{v_1}^{v_2} \varphi_i(x,y)\ ds. \tag{A.2}$$

These integrals may be evaluated with the following triangle integration formulae:

$$\iint_{\Omega^e} \zeta_1^l \zeta_2^m \zeta_3^n\ dx\ dy = \frac{l!m!n!}{(l+m+n+2)!} 2\Delta \tag{A.3}$$

$$\int_i^j \zeta_i^l \zeta_j^m\ ds = \frac{l!m!}{(l+m+1)!} L_{ij} \tag{A.4}$$

where

Ω^e	integration area of triangular element
$\zeta_1, \zeta_2, \zeta_3$	the three area coordinates raised to powers l,m,n
Δ	area of the triangle
L_{ij}	length of edge between vertices i and j.

Note that $0! = 1$. In the case of a C^0-linear triangle, a special solution is

$$\iint_{\Omega^e} \zeta_i \zeta_j \, dx \, dy = \begin{cases} \frac{\Delta}{6} & : \quad i = j \\ \frac{\Delta}{12} & : \quad i \neq j \end{cases} . \tag{A.5}$$

A.1 Area, triangular, simplex or barycentric coordinates

Area coordinates (also known as triangular, simplex or barycentric coordinates) are a set of three coordinates naturally realted to triangular geometry (fig. 13.16 in Burnett, p.572). Each coordinate varies linearly from the value 0 on one of the sides to the value 1 at the opposite vertex. Geometrically, ζ_i is a fractional area, $\zeta_i = \Delta_i/\Delta$ and also the fractional distance from the side opposite node i, as indicated by the coordinate lines for ζ_1 shown in the figure. It is immediately apparent from the geometry that the area coordinates are not independent, but in fact satisfy the relation

$$\zeta_1 + \zeta_2 + \zeta_3 = 1 \tag{A.6}$$

The shape functions are identical with the area coordinates for a C^0-linear triangle.

Appendix B

Possible analytic solution of simple geometry

For simple geometries with uniform conductivity distribution, we can derive an analytic solution for the potential throughout the object. As an example, we will use a cylinder of radius R and height H, filled with homogenous material of isotropic constant conductivity σ. Current I will be injected through two point electrodes at positions $p_1(R, \alpha_1)$ and $p_2(R, \alpha_2)$ as given in figure B.1. Using cylinder coordinates with the origin as the axis of the cylinder, the potential ϕ_A at position $p(r, \alpha)$ can

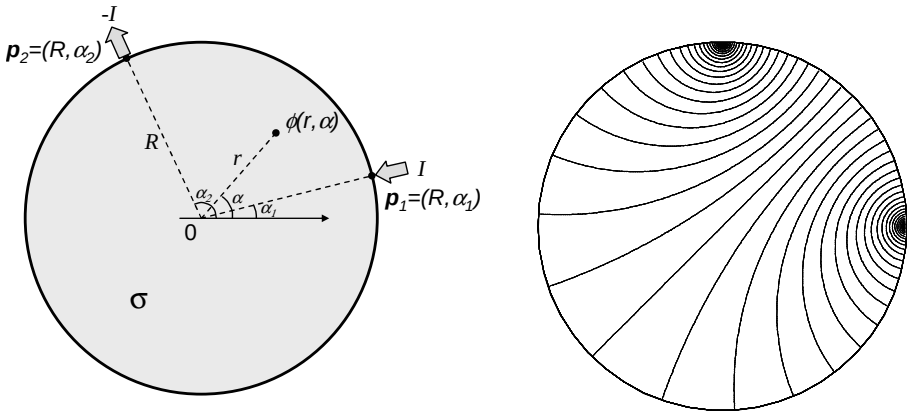

Figure B.1: Set-up for analytical solution on simple cylinder with line electrodes on the boundary and homogenous conductivity σ

be found by using the Green function for a point source in two dimensions,

$$G(\mathbf{r}, \mathbf{r}') = \ln \frac{1}{|\mathbf{r} - \mathbf{r}'|}, \tag{B.1}$$

and the corresponding formulation of the resulting potential

$$\nabla^2 G(\mathbf{r}, \mathbf{r}') = -\delta(\mathbf{r} - \mathbf{r}'). \tag{B.2}$$

In electrical impedance tomography, the forward solution can be calculated analytically only for very simple conductivity sets such as, for example, a circular uniform conductivity distribution with point electrodes on the surface.

In this case, we can deduce the solution by solving Laplace's equation

$$\nabla^2 \phi = 0 \tag{B.3}$$

subject to boundary conditions specifying the current injection.

When a current I is injected between two points on the boundary of a circular medium at angular positions α_1 (source) and α_2 (sink). If a medium of conductivity σ, radius R and thickness t is assumed, the equation which gives the potential difference ϕ_{PO} between point $P(r, \alpha_p)$ within the medium and point O in the centre of the circle, is given by

$$V_{PO} = \frac{I}{2\pi\sigma t} \ln \left(\frac{d2}{d1} \right)^2 \tag{B.4}$$

$$= \frac{I}{2\pi\sigma t} \ln \left(\frac{1 + (\frac{r}{R})^2 - 2(\frac{r}{R}) \cos(\alpha_2 - \alpha_p)}{1 + (\frac{r}{R})^2 - 2(\frac{r}{R}) \cos(\alpha_1 - \alpha_p)} \right). \tag{B.5}$$

On the boundary with $r = R$, we obtain:

$$V_{PO} = \frac{I}{2\pi\sigma t} \ln \left(\frac{1 - cos(\alpha_2 - \alpha_p)}{1 - cos(\alpha_1 - \alpha_p)} \right). \tag{B.6}$$

This formula can be derived from basic principles:
To solve the Laplace Equation

$$\nabla^2 \phi = 0 \tag{B.7}$$

with boundary conditions

$$\mathbf{n} \cdot \sigma \nabla \phi(R, \alpha_1) = j \tag{B.8}$$

$$\mathbf{n} \cdot \sigma \nabla \phi(R, \alpha_2) = -j, \tag{B.9}$$

we employ the method based on Green functions. In this method, the governing equation for the potential of a unit point source, represented by the delta function, can be written as given in Bronstein and Semendjajew (1991):

$$\nabla^2 G(\mathbf{x}, \mathbf{x}') = -2\pi\delta(\mathbf{x} - \mathbf{x}') \tag{B.10}$$

The delta function can, for example, be represented by a Gaussian bell shaped distribution,

$$\delta(x) = \frac{1}{\sqrt{2\pi}\sigma} \int_{-\infty}^{+\infty} e^{-\frac{1}{2\sigma^2}x}\, dx, \tag{B.11}$$

with the standard deviation σ equal to the root of the variance V_x,

$$\sigma = \sqrt{V_x} \tag{B.12}$$

$$V_x = E(X^2) - (E(X))^2 = E\left((x - E(X))^2\right) = \textstyle\sum_k (x - E(X))^2 p_k \tag{B.13}$$

and the expectation or mean value (= center of distribution) of a measurement x_k with probability p_k:

$$E(X) = \sum_k x_k p_k. \tag{B.14}$$

The Green function for this 2D problem is

$$G(\mathbf{x}, \mathbf{x}') = -2 \ln |\mathbf{x} - \mathbf{x}'|, \tag{B.15}$$

where $\mathbf{x}$ represents the point of potential measurement, $\mathbf{x}$' denotes the location of the electric field source.

The boundary term $\frac{\partial \phi}{\partial n}$ can be derived from the injected current, I, of density $\mathbf{j}$, and the height of the cylinder, H:

$$\begin{aligned} I &= \int\limits_{\text{electrode}} \mathbf{j} \cdot d\mathbf{A} = j_n H R \qquad \text{(B.16)} \\ &= \sigma \frac{\partial \phi}{\partial n}\Big|_{p_i} H R. \qquad \text{(B.17)} \end{aligned}$$

Hence we obtain for $\frac{\partial \phi}{\partial n}$

$$\frac{\partial \phi}{\partial n}(\mathbf{p}_i) = \frac{I_i}{\sigma H R}\, \delta(\alpha_i - \alpha'). \tag{B.18}$$

Writing the potential ϕ as effect of the von Neumann point source boundary conditions yields

$$\begin{aligned} \phi(\mathbf{x}) &= \oint_S \frac{\partial \phi}{\partial n} \frac{1}{2\pi} 2 \ln |\mathbf{x} - \mathbf{x}'|\, ds' \\ &= \oint_S \frac{I}{\sigma H R} \left(\delta(\alpha_1 - \alpha') - \delta(\alpha_2 - \alpha')\right) \frac{1}{2\pi} 2 \ln \sqrt{r^2 + R^2 - 2rR\cos(\alpha' - \alpha_0)}\, R d\alpha' \\ &= \frac{I}{2\pi\sigma H} \oint_S \left(\delta(\alpha_1 - \alpha') - \delta(\alpha_2 - \alpha')\right) 2 \ln \sqrt{r^2 + R^2 - 2rR\cos(\alpha' - \alpha_0)}\, d\alpha' \\ &= \frac{I}{2\pi\sigma H} 2 \ln \left(\frac{\sqrt{r^2 + R^2 - 2rR\cos(\alpha_1 - \alpha_0)}}{\sqrt{r^2 + R^2 - 2rR\cos(\alpha_2 - \alpha_0)}} \right) \\ &= \frac{I}{2\pi\sigma H} \ln \left(\frac{r^2 + R^2 - 2rR\cos(\alpha_1 - \alpha_0)}{r^2 + R^2 - 2rR\cos(\alpha_2 - \alpha_0)} \right). \qquad \text{(B.19)} \end{aligned}$$

This is the analytical solution for the potential within a rotationally symmetric cylinder. Figure B.1(b) shows the isopotential lines for a current injection through

electrodes at positions 12 o'clock and 3 o'clock.

Appendix C

Image Farming in non-linear 3D EIT

The convergence of non-linear reconstruction algorithms for Electrical Impedance Tomography (EIT) depends on many factors, such as the noise of the measurement system, the numerical discretization of the object and the starting value of the iterative approximation. We have shown previously that the result can be made independent of the underlying numerical discretization of the object when adaptive mesh refinement methods are used in combination with a logarithmic image smoothness constraint.

The non-linear nature of EIT reconstruction and the unavoidable measurement noise, however, cause several differing solutions in the image space to satisfy the conditions for a 'best-fit' conductivity distribution. A verification of the correctness of an obtained image can only be carried out if the true distribution is known. This, however, is not possible when in-vivo measurements are made and hence we need to establish a measure of similarity between the reconstructed result and a simulated object to characterize the algorithmic behaviour for real experiments.

By distributing and reconstructing a large number of different initial conductivity guesses on a commodity cluster of PCs, we can determine the quality of the final images and correlate the results with the true images within a short time-span. This gives an indication of the quality of image and provides a measure of convergence properties and robustness of the tested algorithms.

In this chapter, we present results from these investigations into the characteristics and efficient reconstruction of the final image and comment on the clinical

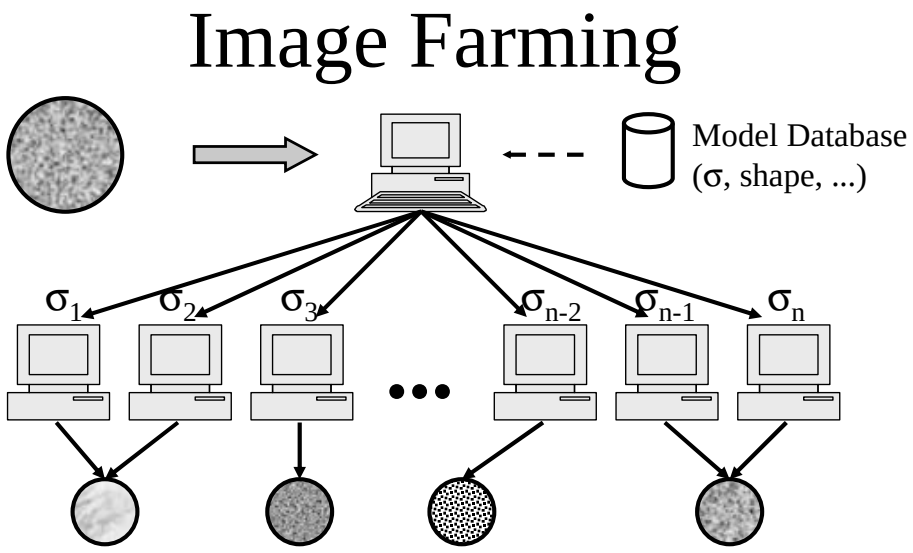

Figure C.1: Image Farming in non-linear 3D EIT

importance of choice of starting value.

C.1 Introduction

In the previous chapters, we have developed all the tools needed for a fully non-linear 3D reconstruction of electrical conductivity images using image smoothness constraint, adaptive mesh refinement techniques and conjugate gradient algorithm. The remaining question is how the choice of starting value of the reconstruction algorithm affects the resulting image. In this chapter, we will derive a method to investigate the different choices of starting value and their corresponding resulting images to be able to draw a map for indicators for the reliability and robustness of a specific reconstruction algorithm.

The non-linear nature of the problem as well as the low sensitivity of electrode voltages to changes of conductivity within central elements, and the measurement noise lead to a large solution space for the conductivy image which contains several local minimia. We will enable the investigation of the convergence behaviour of the algorithm by comparing the resulting images which may be local or the global minimia with the initial starting position of the algorithm.

If the true image is not known, for example as during in-vivo imaging, this method can be used to reconstruct images from a number of different starting choices to obtain a view whether all of the reconstructions are similar. This allows

for obtaining a measure of confidence in the reconstruction, which is important if medical findings are to be based on these images.

C.2 Simulation on distributed resources

Current and future technology allows to assemble together independent PC's to form a computational cluster on which a number of these simulations can be run in parallel. The advantage of such technology in the medical area is that instead of only a single image, a range of possible images showing different interpretations of the measurements can be obtained simultaneously and the decision of a physician regarding possible treatment and/or surgery can be made with all possible information at hand (and not only based on a potentially wrong single image).

In the view of current and future Grid technology (Foster, 2002) it will be possible to use distributed machines and computational clusters of PC's at remote sites for this task. In particular, the Condor system developed at the University of Wisconsin (The Condor Project, 2002) allows for the use of distributed computational resources in an easy-to-use way and offers huge potential for the investigation of large parameter sets.

C.3 Methods

Tools

To make comparisons of resulting images with their simulated 'real' counterparts, we need an 'exact' object model on which we will carry out the simulations of real measurements, a statistical model which adds the measurement noise onto these measurements and a measure of goodness of reconstruction or the correlation of the results with initial starting point in σ-space.

C.4 Measurement of image correlation

Correlation of conductivity images & measure of fidelity

To compare two conductivity distributions, the method of choice would be to compare the (triangular) pixels directly. However, since we are changing the discretization and each element can contain a different conductivity, this method would

have its shortcomings (difficult implementation, distortion of the density of comparison points).

Instead, we use the method as described in the previous chapter, where a regular grid of points is used for determining the conductivity distribution in 2D images and 3D volumes.

The conductivity defined on the triangular elements is mapped by a fast algorithm (Qhull's tsearch) to the regular grid points. The points in the regular grid then sample/identify a unique and homogenous representation of the conductivity distribution and the comparison of differing images/volumes is straightforward. For this comparison, we employ the correlation measure as follows:

Assume that $\mathbf{r}_i = [x_i, y_i, z_i]$, $(i \in [1...N])$ represents the positions of the N regular grid points in three-dimensional space. The corresponding conductivity measurements are then stored in a vector σ of size $(N \times 1)$.

There will be three such vectors for each simulation we are performing: $\sigma_\mathbf{0}$ representing the conductivities of the original image at the positions $\mathbf{r}$; $\sigma_\mathbf{s}$ for the starting value of the computation; and $\sigma_\mathbf{f}$ containing the conductivities of the final result once the computation has finished.

As all three vectors are sampled at the same positions within the volume, we can easily compute their correlation to obtain a measure of closeness of the images as follows (Bronstein and Semendjajew, 1991, p.692).

For two vectors x_i and y_i $(i = 1..N)$ with respective mean values of $\bar{x}$ and $\bar{y}$, and variances $s_x^2 = \frac{1}{N-1}\sum_{i=1}^{N}(x_i - \bar{x})^2$ and $s_y^2 = \frac{1}{N-1}\sum_{i=1}^{N}(y_i - \bar{y})^2$, the covariance is defined as

$$m_{xy} = \frac{1}{N-1}\sum_{i=1}^{N}(x_i - \bar{x})(y_i - \bar{y}). \tag{C.1}$$

The correlation coefficient between these two vectors is

$$C_{xy} = \frac{m_{xy}}{s_x s_y} = \frac{\sum_{i=1}^{N}(x_i - \bar{x})(y_i - \bar{y})}{\sqrt{\sum_{i=1}^{N}(x_i - \bar{x})^2 \sum_{i=1}^{N}(y_i - \bar{y})^2}}. \tag{C.2}$$

In addition to the correlation, which only gives an indication of relative changes, we employ the following measure to obtain an absolute measure of the convergence

behaviour of the algorithm.

The measure of fidelity

As a measure of fidelity, we follow the method proposed by Yorkey *et al.* (1987). We define the measure of fidelity, $\mathcal{F}$, as the squared inner product of the difference between the true resistivity profile (σ_0) and the estimate (σ), normalised by the squared inner product between the true resistivity and its average value ($\bar{\sigma}_0$), i.e.

$$\mathcal{F}(\sigma) = \frac{(\sigma_0 - \sigma)^T(\sigma_0 - \sigma)}{(\sigma_0 - \bar{\sigma}_0)^T(\sigma_0 - \bar{\sigma}_0)}. \tag{C.3}$$

The normalisation allows to express $\mathcal{F}$ in the range $0 \leq \mathcal{F} \leq 1$. This corresponds to a value of $\mathcal{F} = 1$ if we choose the average distribution as starting value, and a value of $\mathcal{F} = 0$ when the reconstruction is perfect. Vadasz and Sebestyen (1996) emphasize that this choice of average conductivity of the object as initial guess is also pratical with real measurements, since it is usually known or can easily be extracted from the measurements.

The measure would be unsuitable for homogenous distributions as the denominator would be equal to zero, however, we will only investigate conductivity distributions which contain conductivity variations.

We have devised a method for the testing of the convergence properties and hence robustness of reconstruction algorithms. This method allows the exploration of the image space by farming out a large number of starting guesses for the initial conductivity distribution. However, further work is required to extend and apply these ideas to real test cases and to be able to determine the robustness of a range of reconstruction algorithms used in the EIT community.

Appendix D

Terminology of electric + magnetic parameters

$R = \frac{U}{I}$	resistance	Widerstand
$G = \frac{1}{R}$	conductance	(Wirk)Leitwert
$\varrho = \frac{RA}{l}$	resistivity	Spezifischer Widerstand
$\sigma = \frac{1}{\varrho}$	conductivity	Leitfähigkeit
$\epsilon = \epsilon_r \epsilon_0$	electric permittivity	Permittivität
$\mu = \mu_r \mu_0$	magnetic permeability	Permeabilität
$\bar{Z} = \frac{\bar{U}}{\bar{I}} = R + iX$	impedance	Scheinwiderstand / Impedanz
$\bar{Y} = \frac{1}{\bar{Z}} = G + iB$	admittance	Scheinleitwert / Admittanz
X	reactance	Blindwiderstand / Reaktanz
B	susceptance	Blindleitwert / Suszeptanz

Bibliography

Ackermann E. *Biophysical Sciences*, chapter 2. Prentice Hall Inc, 1962.

Adler A, Guardo R, and Berthiaume Y. Impedance imaging of lung ventilation: do we need to account for chest expansion? *IEEE Trans Biomed Eng*, **45**:412–21, 1996.

Arridge S and Schweiger M. A gradient-based optimisation scheme for optical tomography. *Optics Express*, **2**(6):213–26, 1998.

Artola J and Dell J. Broyden quasi-newton method applied to electrical impedance tomography. *Electronic Letters*, **30**(1):27–8, 6 January 1994.

Aste T and Weaire D. *The pursuit of perfect packing*. IOP Publishing, Bristol, UK, 2000.

Avill R, Mangnall Y, Bird N, Brown B, Barber D, Seagar A, Johnson A, and Read N. Applied potential tomography: A new noninvasive technique for measuring gastric emptying. *Gastroenterology*, **26**:1019–26, 1989.

Baines M. Grid adaptation via node movement. *Applied Numerical Mathematics*, **26**:77–96, 1998.

Barber C, Dobkin D, and Huhdanpaa H. The quickhull algorithm for convex hulls. 1996. `http://www.geom.umn.edu/software/qhull/`.

Barber D and Brown B. Applied potential tomography. *J Phys E Sci Instrum*, **17**:723–33, 1984.

Batacharya B and Tandon SN. Potential distribution in the thorax in relation to electrical field plethysmography. *Med Biol Eng Comput*, **26**:303–9, 1988.

Bathe K. *Finite Element Procedures in Engineering Analysis*. Prentice Hall Inc, USA, 1982.

Bayford R, Hanquan Y, Boone KG, and Holder DS. Experimental validation of a novel reconstruction algorithm based on backprojection of lagrange multipliers. *Physiol Meas*, **16**(Suppl. 3A):A237–47, 1995.

Blatter G, Feigel'man M, Geshkenbein V, Larkin A, and Vinokur V. Vortices in high-temperature superconductors. *Rev Mod Phys*, **66**:1125–388, 1994.

Blott B, Cox S, Daniell G, Caton M, and Nicole D. High fidelity imaging and high performance computing in nonlinear EIT. *Physiol Meas*, **21**:7–14, 2000.

Blott B, Daniell G, and Meeson S. Electrical impedance tomography with compensation for electrode positioning variations. *Phys Med Biol*, **43**:1731–9, 1998a.

Blott B, Daniell G, and Meeson S. Nonlinear reconstruction constrained by image properties in EIT. *Phys Med Biol*, **43**:1215–24, 1998b.

Boone K and Holder D. Current approaches to analogue instrumentation design in electrical impedance tomography. *Physiol Meas*, **17**:229–47, 1996.

Borcea L. Nonlinear multigrid for imaging electrical conductivity and permittivity at low frequency. *Inverse Problems*, **17**(2):329–59, 2001.

Borouchaki H and George PL. Aspects of 2-D Delaunay mesh generation. *Int J Num Methods in Engineering*, **40**:1957–75, 1997.

Borsic A. *Regularisation methods for imaging from electrical measurements*. Ph.D. thesis, School of Engineering, Oxford Brookes University, 2002.

Breckon W and Pidcock M. Some mathematical aspects of electrical impedance tomography. In M Viergever and A Todd-Pokropek, editors, *Mathematics and Computer Science in Medical Imaging*, NATO ASI Series, pages 3531–62. Springer Verlag, 1987a.

Breckon W and Pidcock M. Data errors and reconstruction algorithms in electrical impedance tomography. *Clin Phys Physiol Meas*, **9**(Suppl. A):105–9, 1988.

Breckon WR and Pidcock MK. Mathematical aspects of impedance imaging. *J Clin Physiol Meas*, **8**:77–84, 1987b.

Bronstein I and Semendjajew K. *Taschenbuch der Mathematik*. B.G. Teubner Verlagsgesellschaft Stuttgart Leipzig; Verlag Nauka Moskau, 25 edition, 1991.

Brown B. Overview of clinical applications. In *Proc. of EC COMAC-BME Workshop on EIT*, pages 29–35. 1990.

Brown B, Barber D, and Seagar A. Applied potential tomography: Possible clinical applications. *Clin Physiol Meas*, **6**:109–21, 1985.

Brown B and Seagar A. The Sheffield data collection system. *Clin Phys and Physiol Meas*, **8**:91–7, 1987.

Budinger T. Medical imaging techniques. August 2001. URL `http://cfi.lbl.gov/~budinger/medimaging.html`.

Burnett D. *Finite element analysis, from concepts to applications*. Addison-Wesley, 1987.

Calderon AP. On an inverse boundary value problem. In W Meyer and M Raupp, editors, *Seminar on Numerical Analysis and its Applications to Continuum Physics*, pages 65–73. Brasilian Math. Society, Rio de Janeiro, 1980.

Cheney M, Isaacson D, and Newell J. Electrical impedance tomography. *SIAM Review*, **41**(1):85–101, 1999.

Cheng KS, Isaacson D, Newell J, and Gisser D. Electrode models for electric current computed tomography. *IEEE Trans Biomed Eng*, **36**:918–24, 1989.

Cingoski V, Murakawa R, Kaneda K, and Yamashita H. Automatic mesh generation in finite element analysis using dynamic bubble system. *J Appl Phys*, **81**(8):4085–7, 1997.

Clarke C. Probabilistic methods in a biomagnetic inverse problem. *Inverse Problems*, **5**:1–14, 1989.

Clarke C and Janday B. The solution of the biomagnetic inverse problem by maximum statistical entropy. *Inverse Problems*, **5**:483–500, 1989.

Cohen-Bacrie C, Goussard Y, and Guardo R. Regularized reconstruction in electrical impedance tomography using a variance uniformization constraint. *IEEE Trans Med Imaging*, **16**(5):562–71, 1997.

Committee on the Mathematics and Physics of Emerging Dynamic. Mathematics and physics of emerging biomedical imaging. Online Book at `http://www.nap.edu/catalog/5066.html`, 1996.

Constable SC, Parker RL, and Constable CG. Occam's inversion: a practical algorithm for generating smooth models from electromagnetic sounding data. *Geophysics*, **52**:289–300, 1987.

Coskun N and Szymanski J. The induced polarization method for archaeology: Two-dimensional modelling using the finite difference method. In A Vogel, editor, *Geophysical Exploration of Archaeological Sites*, volume 7 of *Theory and Pratice of Applied Geophysics*, pages 89–101. Vieweg Publishing, Braunschweig/Wiesbaden, 1993.

Courant R. Variational methods for solution of problems of equilibrium and vibration. *Bull Amer Math Soc*, **49**:1–23, 1943.

CSEP. Direct and inverse bioelectric field problems. Electronic book, Computational Science Education Project (CSEP), USA, 1996. `http://csep1.phy.ornl.gov/CSEP/CSEP.html`.

Dawn S, Gotway M, and Webb W. Multidetector-row spiral computed tomography in the diagnosis of thoracic diseases. *Respiratory Care Online*, **46**(9), September 2001. URL `http://www.rcjournal.com/contents/09.01/09.01.0912.html`.

Delaunay B. Sur la sphère. *Vide Izvestia Akademia Nauk SSSR VII Seria Otdelenie Matematicheskii i Estestvennyka Nauk*, **7**:793–800, 1934.

Dickin F and Wang M. Electrical resistance tomography for process applications. *Meas Sci Technol*, **7**:247–69, 1996.

Dobson D. Convergence of a reconstruction method for the inverse conductivity problem. *SIAM J Appl Math*, **52**(4):442–58, 1992.

Dobson D and Santosa F. An image enhancement technique for electrical impedance tomography. *Inverse Problems*, **10**:317–34, 1994a.

Dobson D and Santosa F. Resolution and stability analysis of an inverse problem in electrical impedance tomography: dependence on the input current patterns. *SIAM J Appl Math*, **54**(6):1542–60, 1994b.

Dobson DC. Recovery of blocky images in electrical impedance tomography. In HW Engl, AK Louis, and W Rundell, editors, *Inverse Problems in Medical Imaging and Nondestructive Testing*, pages 43–64. Springer-Verlag Wien, 1997.

Doerstling B. *A 3D reconstruction algorithm for the linearized inverse boundary value problem for Maxwell's equations.*. Ph.D. thesis, Rensselaer Polytechnic Institute, 1995.

Duffin R. Distributed and lumped networks. *J of Mathematics and Mechanics*, **8**(5):793–826, 1959.

Eyüboglu B, Birgül O, and Ider Y. Magnetic resonance - electrical impedance tomography (mr-eit): A new technique for high resolution conductivity imaging. In D Holder, editor, *Biomedical Applications of EIT - Scientific Abstracts*, 2^{nd} EPSRC Engineering Network Meeting, pages 82–5. University College London, 5-7 April 2000.

Fangohr H, de Groot P, and Cox S. Critical transverse forces in weakly pinned driven vortex systems. *Physical Review B*, **63**:1–5, 2001.

Fangohr H, Price A, Cox S, de Groot P, Daniell G, and Thomas K. Efficient methods for handling long-range forces in particle-particle simulations. *J Comp Phys*, **162**:372–84, 2000.

Foster I. The Grid: A new infrastructure for 21st century science. *Physics Today*, **55**(2):42–47, 2002.

Foster K and Schwan H. Dielectric properties of tissues and biological materials: a critical review. *Crit Reviews in Biomed Engng*, **17**(1):25–104, 1989.

Freitag L. On combining Laplacian and optimization-based mesh smoothing techniques. *Trends in Unstructured Mesh Generation*, **AMD-220**:37–43, July 1997.

Fulton W and Lipczynski R. Optimising the time to solution in electrical impedance tomography. *IEE Proc Sci Meas Technol*, **142**(6):433–41, 1995.

Gaeke E. Tightening the belt for a cheaper body scan.... *New Scientist*, **134**(1819):18, 1992.

Galatsanos S and Katsaggelos A. Methods for choosing the regularization parameter and estimating the noise variance in image restoration and their relation. *IEEE Trans Image Processing*, **1**:322–336, 1992.

Geddes L and Baker L. The specific resistance of biological material – a compendium of data for the biomedical engineer and physiologist. *Med Biol Engng*, **5**:271–93, 1967.

Generowicz J, Beckett D, Hiett B, Molinari M, Thomas K, and Cox S. Optimized use of finite elements in photonic crystal modelling. *submitted for publication*, 2002.

Geselowitz D. An application of electrocardiographic lead theory to impedance plethysmography. *IEEE Trans Biomed Eng*, **18**:38–41, 1971.

Geuzaine C and Remacle J. Gmsh - 3D meshing software. 2000. URL `http://www.bloodwolf.org/~jf/Gmsh_Eng.html`.

Gibson A, Tidswell T, Bayford R, and Holder D. Spherical and realistic head models in electrical impedance tomography. In D Holder, editor, *Biomedical Applications of EIT - Scientific Abstracts*, 2^{nd} EPSRC Engineering Network Meeting, pages 150–4. University College London, 5-7 April 2000.

Gisser D, Isaacson D, and Newell J. Electric current computed tomography and eigenvalues. *SIAM J Appl Math*, **50**(6):1623–34, 1990.

Gjelsvik A, Aam S, and Holten L. Hachtel's augmented matrix method - a rapid method improving numerical stability in power system statuc state estimation. *IEEE Trans Power Apparatus and Systems*, **PAS-104**:2987–92, 1985.

GLUT. Opengl utility toolkit. 2001. `http://www.opengl.org/developers/documentation/glut.html`.

Golias N and Dutton R. Delaunay triangulation and 3D adaptive mesh generation. *Finite Elements in Analysis and Design*, **25**:331–41, 1997.

Golub G and O'Leary D. Some history of the conjugate gradient and Lanczos algorithms. *SIAM Journal on Optimization*, **2**(1):21–42, 1989.

Golub G and vanLoan C. *Matrix Computations*. Johns Hopkins University Press, Baltimore, 1989.

Groetsch C. *Inverse Problems in the Mathematical Sciences*. Vieweg-Verlag, Germany, 1993.

Hadamard J. *Lectures on Cauchy's Problem in Linear Partial Differential Equations*. Yale University Press, 1923.

Haile J. *Molecular Dynamics Simulation, Elementary Methods*. John Wiley & Sons, 1997.

Hake J. Parallel algorithms for matrix operations and their performance on multiprocessor systems. In L Kronsjö and D Shumsherruddin, editors, *Advances in Parallel Algorithms*, pages 396–437. Blackwell Scientific Publications, London, 1992.

Heimbach M. *J G Webster: Electrical Impedance Tomography*, chapter 9:Data Collection Errors, pages 87–96. IOP Publishing, 1990.

Henderson RP and Webster JG. An impedance camera for spatially specific measurements of the thorax. *IEEE Treans Biomed Eng*, **25**:250–4, 1978.

Holder D and Brown B. Biomedical application of EIT: a critical review. In D Holder, editor, *Clinical and Physiological Applications of EIT*. UCL Press, London, UK, 1993.

http://www.eidors.org. EIT and Diffuse Optical Tomography Reconstruction Software (EIDORS) homepage. 2002.

Hua P, Woo E, Tompkins W, and Webster J. Finite element modeling of electrode-skin contact impedance in electrical impedance tomography. *IEEE Trans Biomed Eng*, **40**(4):335–43, 1993.

Hua P, Woo E, Webster J, and Tompkins W. Iterative reconstruction methods using regularization and optimal current patterns in electrical impedance tomography. *IEEE Trans Med Imaging*, **10**:621–28, 1991.

Hua P, Woo E, Webster J, and Tompkins W. Improved methods to determine optimal currents in electrical impedance tomography. *IEEE Trans Med Imaging*, **11**:488–95, 1992.

Isaacson D. Distinguishability of conductivities by electric current computed tomography. *IEEE Trans Med Imaging*, **5**(2):91–5, 1986.

Jackson J. *Classical Electrodynamics*. John Wiley & Sons, 3rd edition, 1998.

Jain H, Isaacson D, Edic P, and Newell J. Electrical impedance tomography of complex conductivity distributions with noncircular boundary. *IEEE Trans Biomed Eng*, **44**(11):1051–1060, 1997.

Joe B. Geompack - 2D/3D meshing software. 1996. `http://www.cs.sunysb.edu/~algorith/implement/geompack/implement.shtml`.

Johnson C and McLeod R. Nonuniform spatial mesh adaption using a posteriori error estimates: applications to forward and inverse problems. *Appl Num Math*, **14**:311–26, 1994.

Karamete B, T.Tokdemir, and Ger M. Unstructured grid generation and a simple triangulation algorithm for arbitrary 2-d geometries using object oriented programming. *Int J Num Methods in Engineering*, **40**:251–68, 1997.

Kim D, Baker L, Pearce J, and Kim W. Origins of the impedance change in impedance cardiography by a three-dimensional finite element model. *IEEE Trans Biomed Eng*, **35**:993–1000, 1988.

Kim Y. *A three-dimensional modifiable computer body model and its applications*. Ph.D. thesis, Dept. of Electrical & Computer Engineering, Univ. Wisconsin, Madison, USA, 1982.

Knudsen K. A new direct method for reconstructing isotropic conductivities in the plane. *Physiol Meas*, **24**:391–401, 2003.

Kohn R and Vogelius M. Determining the conductivity by boundary measurement ii - interior results. *Comm Pure Appl Math*, **38**:644–67, 1985.

Kohn R and Vogelius M. Relaxation of a variational method for impedance computed tomography. *Commun Pure Appl Math*, **40**:745–77, 1987.

Kohn RV and McKenney A. Numerical implementation of a variational method for electrical impedance tomography. *Inverse Problems*, **6**:389–414, 1990.

Kothiyal K, Shankar B, Fogelson L, and Thakor N. Three-dimensional computer model of electric fields in internal defibrillation. *Proc IEEE*, **76**:720–30, 1988.

Kwon O, Woo EJ, Yoon JR, and Seo JK. Magnetic resonance electrical impedance tomography (mreit): simulation study of j-substitution algorithm. *IEEE Trans on Biomedical Engineering Feb 2002*, **49**(2):160–7, 2002.

Kyriacou GA, Koukourlis CS, and Sahalos JN. A reconstruction algorithm for electrical impedance tomography with optimal configuration of the driven electrodes. *IEEE Trans Med Imaging*, **12**(3):430–8, 1993.

Kytömaa H and Weselake K. Current distribution and finite element mesh selection for electrical impedance tomography. *Computational Mechanics*, **15**:161–72, 1994.

Lamm P. Inverse problems and ill-posedness. In *Inverse Problems in Engineering: Theory and Practice*, pages 1–10. The American Society of Mechanical Engineers, 1993.

Lehr J. A vector derivation useful in impedance plethysmographic field calculations. *IEEE Trans Biomed Eng*, **BME-19**:156–7, 1972.

Lionheart WRB, Kaipio J, and McLeod C. Generalized optimal current patterns and electrical safety in EIT. *Physiol Meas*, **22**(1):85–90, 2001.

Liu W, Hua P, and Webster J. Three-dimensional reconstruction in electrical impedance tomography. *Clin Phys Physiol Meas*, **9**(Suppl A):131–5, 1988.

Meeson S. *An investigation of optimal performance criteria in electrical impedance tomography*. Phd thesis, University of Southampton, August 1997.

Meeson S, Blott B, and Killingback A. EIT data noise evaluation in the clinical environment. *Physiol Meas*, **17**:A33–A38, 1996.

MESA. The mesa 3-d graphics library. 2001. `http://www.mesa3d.org/`.

Meshing Research Corner. `http://www.andrew.cmu.edu/user/sowen/mesh.html`. 2001.

Metherall P, Barber D, Smallwood R, and Brown B. Three-dimensional electrical impedance tomography. *Nature*, **380**:509–12, 1996.

Miller C and Henriquez C. Finite element analysis of bioelectric phenomena. *Crit Rev in Biomed Eng*, **18**:207–33, 1990.

Molinari M, Cox S, Blott B, and Daniell G. Adaptive mesh refinement techniques for electrical impedance tomography. *Physiol Meas*, **22**(1):91–6, 2001a.

Molinari M, Cox S, Blott B, and Daniell G. Efficient non-linear 3D electrical tomography and finite element optimizations for functional source imaging. *Biomedizinische Technik Biomedical Engineering*, **46**(Ergänzungsband 2):130–1, 6-9 September 2001b. Conference Proceedings of NFSI2001, Innsbruck, Austria, ISSN 0939-4990.

Molinari M, Cox S, Blott B, and Daniell G. Efficient non-linear 3D electrical tomography reconstruction. In R Mann, D Mewes, and P Ronson, editors, *Proceedings of the 2nd World Congress on Industrial Process Tomography (WCIPT)*, pages 424–32. VCIPT, 29-31 August 2001c. ISBN 0 85316 224 7.

Molinari M, Cox S, Blott B, and Daniell G. Optimal finite element modeling and efficient reconstruction in non-linear 3D electrical resistance tomography. In D Holder, editor, *3rd EPSRC Engineering Network Meeting on Biomedical*

Applications of EIT - Scientific Abstracts. University College London, 4-6 April 2001d.

Molinari M, Cox S, Blott B, and Daniell G. Comparison of algorithms for non-linear inverse 3D electrical tomography reconstruction. *Physiol Meas*, **23**(1):95–104, 2002a.

Molinari M, Cox S, Blott B, and Daniell G. Optimal imaging with adaptive mesh refinement in electrical tomography. *Physiol Meas*, **23**(1):121–8, 2002b.

Molinari M, Fangohr H, Generowicz J, and Cox S. Finite element optimizations for efficient non-linear electrical tomography reconstruction. In R Mann, D Mewes, and P Ronson, editors, *Proceedings of the 2nd World Congress on Industrial Process Tomography (WCIPT)*, pages 406–17. VCIPT, 29-31 August 2001e. ISBN 0 85316 224 7.

Morruci JP, Granie M, Lei M, Chabert M, and Marsili PM. 3d reconstruction in electrical impedance imaging using a direct sensitivity matrix approach. *Physiol Meas*, **16**(3A):A123–8, 1995.

Mueller JL, Isaacson D, and Newell JC. A reconstruction algorithm for electrical impedance tomography data collected on rectangular electrode arrays. *IEEE Trna Biomed Eng*, **46**(11):1379–86, 1999.

Murai T and Kagawa Y. Electrical impedance computed tomography based on a finite element model. *IEEE Trans Biomed Eng*, **BME-32**:177–84, 1985.

Nachman A. Global uniqueness for a two-dimensional inverse boundary value problem. *Ann Math*, **143**:71–96, 1996.

Natarajan R and Seshadri V. Electric-field distribution in the human body using finite-element method. *Med Biol Eng*, **14**:489–93, 1976.

Newell J, Isaacson D, Saulnier D, Cheney M, and Gisser D. Acute pulmonary edema assessed by electrical impedance tomography. In *Proc 15th IEEE/EMBS Conf.*, pages 92–93. 1993.

Niceno B. Easymesh - 2D meshing software. 2001. `http://www-diama.univ.trieste.it/~nirftc/research/easymesh/`.

Nunez P. *Electric fields of the brain: the neurophysics of EEG*. Oxford University Press, New York, 1981.

Otto GP and Chew WC. Time-harmonic impedance tomography using the T-Matrix method. *IEEE Trans Med Imaging*, **13**(3):508–516, 1994.

Paulson K. *Parallel Algorithms for Three Dimensional Electrical Impedance Tomography*. Ph.D. thesis, School of Computing and Mathematical Sciences, Oxford Brookes, 1992.

Paulson K, Breckon W, and Pidcock M. Electrode modelling in electrical impedance tomography. *SIAM J Appl Math*, **52**(4):1012–22, 1997.

Paulson K, Lionheart W, and Murdock M. POMPUS: An optimized EIT reconstruction algorithm. *Inverse Problems*, **11**:425–37, 1995.

Paulson K, Lionheart W, and Pidcock M. Optimal experiments in electrical impedance tomography. *IEEE Trans Med Imaging*, **12**(4):681–6, December 1993.

Paulson K, Lionheart W, and Pidcock M. Fast, non-linear inversion for electrical impedance tomography. *Image and Vision Computing*, **12**(6):367–73, 1994.

Pinheiro P and Dickin F. Sparse matrix techniques for use in electrical impedance tomography. *Int J Numerical Methods in Engineering*, **40**:439–51, 1997.

Pinheiro P, Loh W, and Dickin F. Smoothness-constrained inversion for two-dimensional electrical resistance tomography. *Meas Sci Technol*, **8**:293–302, 1997.

Polydorides N and Lionheart W. A matlab toolkit for three-dimensional electrical impedance tomography: a contribution to the Electrical Impedance and Diffuse Optical Reconstruction Software project. *Meas Sci Technol*, **13**:1871–83, 2002.

Press WH, Teukolsky SA, Vetterling WT, and Flannery BP. *Numerical Recipes in C*. Cambridge University Press, 2nd edition, 1997.

Robert P, Roux A, Harvey C, Dunlop M, Daly P, and Glassmeier K. Tetrahedron geometric factors. In G Paschmann and P Daly, editors, *Analysis Methods for Multi-Spacecraft Data*, pages 323–49. ISSI/ESA Publications, 1998.

Ruan W, Guardo R, and Adler A. Experimental evaluation of two iterative reconstruction methods for induced current electrical impedance tomography. *IEEE Trans Med Imaging*, **15**(2):180–7, 1996.

Rudin L, Osher S, and Fatemi E. Nonlinear total variation based noise removal algorithms. *Physica D*, **60**:259–68, 1992.

Salazar-Palma M, Sarkar T, Garcia-Castillo L, Roy T, and Djordjevic A. *Iterative and Self-Adaptive Finite Elements in Electromagnetic Modelling*. Artech House Inc., Norwood, 1998.

Schellbach K. Probleme der Variationsrechnung. *J Reine Angew Math*, **41**:293–363, 1851.

Schinnerl M, Schöberl J, and Kaltenbacher M. Nested multigrid methods for the fast numerical computation of 3D magnetic fields. *IEEE Trans Magnetics*, **36**(4):1557–60, 2000.

Schmidt J, Johnson C, Eason J, and McLeod R. Applications of automatic mesh generation and adaptive methods in computational medicine. In J Flaherty and I Babuska, editors, *Modeling, Mesh Generation, and Adaptive Methods for Partial Differential Equations*. Springer-Verlag, 1994.

Schöberl J. Netgen - 3D meshing software. 2001. `http://www.sfb013.uni-linz.ac.at/~joachim/netgen/`.

Schütze C. DC-geoelectrical deep sounding in combination with modern inversion technologies: a tool to investigate geological structures. Webpage, February 1998. `http://ghp712.geo.uni-leipzig.de/~geocr/ktb/`.

Schwab A. *Begriffswelt der Feldtheorie: praxisnahe, anschauliche Einfuehrung*. Springer, Berlin, 5th edition, 1998.

Seagar AD, Barber DC, and Brown BH. Theoretical limits to sensitivity and resolution in impedance imaging. *Clin Phys Physiol Meas*, **8**(Suppl. A):13–31, 1987.

Shephard M. Automatic and adaptive mesh generation. *IEEE Trans Magnetics*, **MAG-21**:2484–89, 1985.

Shewchuk J. An introduction to the conjugate gradient method without the agonizing pain. Technical report, Carnegie Mellon University, Pittsburgh, USA, 1994.

Shewchuk J. Triangle: Engineering a 2D quality mesh generator and delaunay triangulator. *First Workshop on Applied Computational Geometry*, **ACM**:124–33, 1996.

Sieber H and Huber L. *Mathematische Formeln*. Ernst Klett Verlage, Stuttgart, 1990.

Siemens. Forschung und innovation highlights. Brochure 1, 1999.

Siltanen S, Mueller JL, and Isaacson D. An implementation of the reconstruction algorithm of A Nachman for the 2D inverse conductivity problem. *Inverse Problems*, **16**:681–99, 2000.

Silvester P and Ferrari R. *Finite Elements for Electrical Engineers*. Cambridge University Press, UK, 3rd edition, 1996.

Skilling J and Bryan RK. Maximum entropy image reconstruction: general algorithm. *Mon Notices R Astron Soc*, **211**:111–24, 1984.

Somersalo E, Cheney M, and Isaacson D. Existence and uniqueness for electrode models for electric current computed tomography. *SIAM J Appl Math*, **52**:1023–40, 1992.

Somersalo E, Cheney M, Isaacson D, and Isaacson E. Layer stripping: a direct numerical method for impedance imaging. *Inverse Problems*, **7**:899–926, 1991.

Sylvester J and Uhlman G. A global uniqueness theorem for an inverse boundary value problem. *Annals of Math*, **125**:153–69, 1987.

Szymanski J and Tsourlos P. The resistive tomography technique for archaeology: an introduction and review. *Achaeologia Polona*, **31**:5–32, 1993.

Takeda A, Cox S, and Payne A. Parallel numerical modelling of ice flow in antarctica. In H Arabnia, editor, *Proceedings of International Conference on Parallel and Distributed Processing Techniques and Applications*, pages 335–41. CSREA Press, June 2000.

Tang M, Wang W, and Wheeler J. Incorporating more compatible prior information into the image in electrical impedance tomography. In D Holder, editor, 3^{rd} *EPSRC Engineering Network Meeting on Biomedical Applications of EIT – Scientific Abstracts*, pages 37–40. University College London, UK, 4-6 April 2001.

The Condor Project. 2002. `http://www.cs.wisc.edu/condor`.

Thompson J, Soni B, and Weatherill N, editors. *Handbook of Grid Generation*. CRC Press LLC, USA, 1999.

Toyoda K. EIT for muskmelon quality assurance. The EIT mailing list, 2000. 06/02/2000.

Vadasz D and Sebestyen I. Comparison of the Newton-Raphson and the spectral expansion impedance tomography reconstruction algorithms. *IEEE Trans Magnetics*, **32**(3):1286–9, 1996.

Vassilevski P and Wade J. A comparison of multilevel methods for total variation regularization. *Electronic Transactions on Numerical Analysis*, **6**:255–70, 1997.

Vauhkonen M. *Electrical Impedance Tomography and prior information*. Ph.D. thesis, Natural and Environmental Sciences, Kuopio University, Finland, 1997.

Vauhkonen M, Kaipio JP, Somersalo E, and Karjalainen PA. Electrical impedance tomography with basic constraints. *Inverse Problems*, **13**:523–30, 1997.

Vauhkonen M, Lionheart W, Heikkinen L, Vauhkonen P, and Kaipio J. A MATLAB package for the EIDORS project to reconstruct two-dimensional EIT images. *Physiol Meas*, **22**:107–11, 2001.

Vauhkonen P, Vauhkonen M, Savolainen T, and Kaipio J. Three-dimensional electrical impedance tomography based on the complete electrode model. *IEEE Trans Biomed Eng*, **46**(9):1150–60, 1999.

WCIPT. Proceedings of the 2nd World Congress on Industrial Process Tomography, R. Mann and D. Mewes and P. Ronson, editors. 29-31 August 2001. ISBN 0 85316 224 7.

Webb S, editor. *The Physics of Medical Imaging*. Medical Science Series. IOP Publishing Ltd, Bristol, UK, 1993 reprint edition, 1988.

Webster J. *Electrical Impedance Tomography*. The Adam Hilger Series on Biomedical Engineering. IOP Publishing Ltd, Bristol, UK, 1990.

Wexler A. Electrical impedance imaging in two and three dimensions. *Clin Phys Physiol Meas*, **9**(4):29–33, 1988.

Williamson F. An historical note on the finite element method. *Int J Numer Methods Eng*, **15**(6):930–4, June 1980.

Woo E, Hua P, Tompkins W, and Webster J. A finite element model with node renumbering for adaptative impedance imaging. In *Proc 10th IEEE-EMBS Conf.*, pages 277–78. New Orleans, LA, 1988.

Woo E, Hua P, Webster J, and Tompkins W. Measuring lung resistivity using electrical impedance tomography. *IEEE Trans Biomed Eng*, **39**(7):756–60, 1992.

Woo EJ, Hua P, Webster JG, and Tompkins WJ. A robust image reconstruction algorithm and its parallel implementation in electrical impedance tomography. *IEEE Trans Med Imaging*, **12**(2):137–46, 1993.

Woo EJ, Hua P, Webster JG, and Tompkins WJ. Finite-element method in electrical impedance tomography. *Med Biol Eng Comput*, **32**:530–6, 1994.

Yamakawa S and Shimada K. High quality anisotropic tetrahedral mesh generation via ellipsoidal bubble packing. In *Proc 9th International Meshing Roundtable*, pages 263–73. Sandia National Laboratories, New Orleans, Louisiana, USA, 2-5 October 2000.

Yorkey T, Webster J, and Tompkins W. Comparing reconstruction algorithms for electrical impedance tomography. *IEEE Trans Biomed Eng*, **34**(11):843–52, 1987.

Yorkey TJ. Electrical impedance tomography with piecewise polynomial conductivities. *J Comp Phys*, **91**:344–60, 1990.

Zadehkoochak M. *Image reconstruction and spectral expansion analysis in electrical impedance tomography*. Ph.d. thesis, University of Southampton, 1992.

Zadehkoochak M, Blott B, Hames T, and George R. Spectral expansion analysis in electrical impedance tomography. *J Phys D Appl Phys*, **24**:1911–6, 1991.

Zienkiewicz O and Craig A. Adaptive refinement, error estimates, multigrid solution, and hierarchic finite element method concept. In *Accuracy Estimates and Adaptive Refinements in Finite Element Computations*, pages 25–59. John Wiley & Sons, London, 1986.